







ELG×LRG distribution through dark matter halo dynamics

GINEVRA FAVOLE ^{1,2} FRANCISCO-SHU KITaura ^{1,2} BORYANA HADZHIYSKA ³ DANIEL EISENSTEIN ⁴
LEHMAN H. GARRISON ⁵ AND SOWNAK BOSE ⁶¹*Departamento de Astrofísica, Universidad de La Laguna, E-38206, La Laguna, Tenerife, Spain*²*Instituto de Astrofísica de Canarias, c/ Vía Láctea s/n, E-38205, La Laguna, Tenerife, Spain*³*Institute of Astronomy, University of Cambridge, Madingley Road, Cambridge CB3 0HA, UK*⁴*Center for Astrophysics, Harvard & Smithsonian, 60 Garden Street, Cambridge, MA 02138, USA*⁵*Scientific Computing Core, Flatiron Institute, 162 Fifth Avenue, New York, NY 10010, USA*⁶*Institute for Computational Cosmology, Department of Physics, Durham University, South Road, Durham, DH1 3LE, UK*

ABSTRACT

We investigate the clustering and halo occupation distribution (HOD) of DESI Y1 emission-line (ELGs) and luminous red (LRGs) galaxies at $0.8 < z < 1.1$, including their cross-correlation (ELG×LRG), using the ABACUSSUMMIT suite and a new Halo Occupation Model (HOME) for galaxy multi-tracers. This integrates intra-halo dynamics, halo exclusion, and quenching, bridging insights from hydrodynamical, HOD, abundance-matching, and semi-analytic studies. Leveraging full phase-space information from the UCHUU N -body simulation, and sampling satellites from dark-matter particle positions via physically motivated prescriptions, HOME reproduces the anisotropic clustering down to $s = 200 h^{-1}\text{kpc}$ with unprecedented accuracy. Model parameters are inferred solely from two-point statistics using a two-level Bayesian framework, yielding high-fidelity ELG, LRG and cross-reference catalogs. We find that satellite ELGs behave as incoherent flows within their parent halos, dominating the clustering below $4 h^{-1}\text{Mpc}$. The HOD from the best-fit HOME has the following properties: (i) 90.50% (85.91%) of ELGs (LRGs) are central galaxies without satellites, residing in halos of $M_{\text{vir}} \sim 6.6 \times 10^{11} (1.2 \times 10^{13}) h^{-1}M_{\odot}$; (ii) the ELG×LRG cross-correlation is governed by central-central pairs and shaped by halo exclusion on $2 - 5 h^{-1}\text{Mpc}$ scales; (iii) 9.50% (14.09%) of ELGs (LRGs) are satellites, of which 1.09% (3.52%) inhabit halos with a central galaxy of the same species in a maximally conformal configuration, 7.02% (0.005%) orbit complementary hosts in a minimally conformal state, and 0.58% (10.57%) are orphans. HOME high sensitivity precisely captures the dynamics of satellites in different host environments, opening a promising avenue for understanding systematics, the dynamical nature of dark matter, potentially distinguishing gravity models.

Keywords: Galaxies (573) — Cosmology (343)

1. INTRODUCTION

A complete and physically motivated galaxy-halo connection scheme is crucial for building high-fidelity reference catalogs for mock calibration to achieve accurate covariance estimates for cosmological analyses. However, establishing a universal prescription is challenging due to the diversity of galaxy populations targeted by new-generation surveys, as the Dark Energy Spectroscopic Instrument (DESI; Levi et al. 2013; DESI Collaboration et al. 2016, 2022) or the *Euclid* space mission

(Laureijs et al. 2011). These surveys observe a variety of galaxy types, each with different compositions, star formation histories, and physical properties. All these sources are complementary biased tracers of the same underlying dark matter field.

To capitalise on ongoing and upcoming observations, it is essential to generalise the standard galaxy-halo connection techniques, i.e. the sub-halo abundance matching (SHAM; Conroy et al. 2006; Behroozi et al. 2010; Trujillo-Gomez et al. 2011) and the halo occupation distribution (HOD; Berlind & Weinberg 2002; Zehavi et al. 2005; Zheng et al. 2005, 2007) models, to different surveys and galaxy tracers. This involves incorporating the effects of target selection, different bias schemes, intra-

halo dynamics, halo exclusion and quenching in our clustering models.

Significant progress has been made in recent years with HOD (e.g., Favole et al. 2016a; Guo et al. 2016; Gonzalez-Perez et al. 2018; Avila et al. 2020; Alam et al. 2020; Hadzhiyska et al. 2021b,a; Yuan et al. 2022; Rocher et al. 2023; Yuan et al. 2025) and SHAM (e.g., Favole et al. 2016b, 2017; Rodríguez-Torres et al. 2016; Chaves-Montero et al. 2016; Contreras et al. 2021; Yu et al. 2022; Favole et al. 2022; Contreras et al. 2023; Gao et al. 2024; Ortega-Martinez et al. 2024) models capable of reproducing, with different levels of precision, the clustering signals of galaxy multi-tracers and their evolution with redshift. However, these models still lack a comprehensive physical interpretation of the ELG configuration and its connection with LRGs, particularly in understanding the impact of peculiar motions and intra-halo dynamics on the small-scale anisotropic clustering and quenching mechanisms.

As part of the *MUSICA*⁷ project, within the *COSMIC SIGNAL*⁸ mock pipeline, in this work we present a novel physically motivated Halo Occupation Model (“HOME”, hereafter) to produce high-fidelity reference catalogs for DESI Y1 ELG, LRG and ELG×LRG tracers based on the ABACUSSUMMIT simulation suite. This new approach includes a dynamical treatment of satellite halos—not tracked by the halo finder in the simulation—via dark-matter (DM) particle positions, and is *applicable to any galaxy survey, galaxy tracer, and simulation*.

Our method reconciles different perspectives from current SHAM, HOD, hydrodynamical and SAM studies about ELGs and LRGs within their host halos (e.g., Chaves-Montero et al. 2016; Hadzhiyska et al. 2021a,b; Favole et al. 2022; Orsi & Angulo 2018), and extends previous SHAM results (Yu et al. 2022) down to $200 h^{-1}\text{kpc}$ scales, with ~ 20 times better resolution, dramatically improving the accuracy of current clustering models (e.g., Prada et al. 2025) on sub-Mpc scales.

Our results demonstrate that the fraction and velocity bias of satellites with respect to their hosts, together with the exclusion mechanism happening between pairs of massive halos, and the quenching of ELG satellites in LRG hosts, are pivotal to accurately predict the anisotropic clustering of both tracers below $4 h^{-1}\text{Mpc}$. The fine interplay between these model ingredients determines HOME’s unprecedented sensitivity, which opens new paths for understanding systematics, constraining

the dynamical nature of DM, and breaking degeneracies between galaxy bias and cosmology.

We present HOME within a two-level Bayesian inference framework that allows us to constrain the physically meaningful parameters—those shaping the clustering and HOD of DESI galaxy multi-tracers—marginalizing over a set of nuisance parameters that drive analytic prescriptions used to build the latent properties of the halo input catalogs for HOME.

To guarantee the latent variables are properly informed by precise phase-space information and DM distribution, we calibrate the analytic prescriptions against independent predictions from external high-resolution N -body simulations. For our analysis we adopt UCHUU, that has the same volume of ABACUSSUMMIT.

In this way, the inference process is robust and computationally optimized at the same time, as we do not need to regenerate the full model at each point of the parameter space, which would be unfeasible.

The aim of this work is threefold: (i) presenting the HOME scheme, including full satellite treatment via ABACUSSUMMIT DM particles, as well as the two-level Bayesian inference framework; (ii) apply it to DESI Y1 observations to accurately predict the two-point ELG, LRG and ELG×LRG correlation functions, and their halo occupation distribution down to $s = 200 h^{-1}\text{kpc}$; (iii) interpreting the HOME results in terms of intra-halo dynamics to shed light on the physics of peculiar motions, redshift-space distortions, halo exclusion and quenching, reconciling them with the current picture from SHAM, HOD, hydrodynamical and SAM studies.

In our analysis we adopt the ABACUSSUMMIT ΛCDM fiducial cosmology, which is consistent with Planck Collaboration et al. (2020): $\Omega_m = 0.31519$, $h = 0.6736$, $n_s = 0.9649$, $\sigma_8 = 0.807952$.

2. DATA

2.1. DESI Y1 observations

We use the LSS catalog (Ross et al. 2025; Adame et al. 2025a) part of the DESI Y1 Data Release (DESI Collaboration et al. 2025), which includes observations collected between May 2021 and June 2022, following a survey validation phase (Lamman et al. 2024).

DESI employs robotic fiber positioners to simultaneously capture spectra for 5,000 celestial targets organized in tiles, routing light through ten spectrographs. The survey observing time is classified into “bright” and “dark” programs based on conditions; both ELGs (Rai-choor et al. 2023) and LRGs (Zhou et al. 2023) are targeted in dark time (see DESI Collaboration et al. 2025).

The DESI Y1 ELG sample comprises 243,202 good redshifts in $0.8 < z < 1.6$, covering $5,914 \text{ deg}^2$ (Adame

⁷ Multi-tracer Skies for hIgh-precision Cosmological Analyses

⁸ COSMIC SIMulated Galaxy Networks Applied on Lightcones

et al. 2025a). ELGs are the DESI targets with the lowest priority: their fiber assignment completeness is 35.5% in Y1, then growing to 60% in the final dataset of 14,000 deg². The LRG sample includes 2,138,600 good redshifts in $0.4 < z < 1.1$, over 5,840 deg², with 69.2% fiber assignment completeness in Y1, then increasing to 90% in the final release.

The ELG and LRG samples (Adame et al. 2025a) span different redshift ranges, with significant overlap only at $0.8 < z < 1.1$. We adopt this shared redshift window as the fiducial region where modeling both their auto- and cross-correlations using HOME.

Employing the same nomenclature as in Adame et al. (2025a), we analyze the clustering of the ELG1 and LRG3 samples, as well as their cross-correlation ELG1×LRG3, at $0.8 < z < 1.1$. The number and density of targets in each sample is reported in Table 1, and we assume $z_{\text{eff}} = 0.95$ as the most representative redshift of the above range (see Adame et al. 2025b).

2.2. The ABACUSSUMMIT simulation

We analyze DESI Y1 observations (§ 2.1) using the ABACUSSUMMIT⁹ suite of 139 large-volume ($L_{\text{box}} = 2h^{-1}\text{Gpc}$), high-resolution ($2 \times 10^9 h^{-1} M_{\odot}$ particle mass) “base” N -body cosmological simulations (Maksimova et al. 2021; Garrison et al. 2021). We use the COMPASO halo catalogs (Hadzhiyska et al. 2022) that include only central host halos (“h”, hereafter).

Here, the halo central core is robustly identified using a L2 halo finding algorithm, rather than simply defining quantities relative to the centre of mass of each COMPASO object. To circumvent the lack of satellites, which are not tracked by the halo finder, we assign them based on DM particle and host positions, as described in § 3.2.

To ensure reliable halo properties, we consider only halos with at least $N_p \geq 65$ DM particles, corresponding to a lower halo mass limit of $1.3 \times 10^{11} h^{-1} M_{\odot}$. This minimal cut returns a population of nearly 225 million central halos—all potential hosts for satellites—including about 1.5×10^{10} DM particles.

We implement HOME on the closest ABACUSSUMMIT snapshot to the effective redshift of the DESI tracers to model (see § 2); this is $z_A = 0.8$, as shown in Table 1. The impact of redshift errors in estimating halo velocities can be quantified as the ratio of the growth factors evaluated at the redshifts of interest: $z_{\text{err}} = 1 - G(z_{\text{eff}})/G(z_A)$. In our case the impact is minimal, as all deviations are within 6% (see Table 1).

In addition to the $2h^{-1}\text{Gpc}$ ABACUSSUMMIT base boxes, we also adopt 1800 $500 h^{-1}\text{Mpc}$ boxes (“small”,

hereafter) at the base mass resolution to estimate our model covariances.

3. METHODOLOGY

In what follows, we describe the ingredients and implementation of our Halo Occupation Model (HOME) for the DESI Y1 ELG1, LRG3, and ELG1×LRG3 samples, in the fiducial redshift range $0.8 < z < 1.1$, using the ABACUSSUMMIT simulation snapshot $z_A = 0.8$.

3.1. Central halos

We characterize central halos (“cen”, hereafter) in HOME by extracting and assigning them the relevant properties of their ABACUSSUMMIT central hosts (§ 2.2) at the snapshot of interest, z_A (Table 1). These are:

- *Maximum circular velocity*: in the ABACUSSUMMIT notation, this is called `vcirc_max_L2com` and is computed relative to the center of mass position and velocity, based on the particles in the L1 CompasO halo¹⁰. We assume $V_{\text{max}}^{\text{cen}} \equiv V_{\text{max}}^{\text{h}}$.
- *Peak circular velocity*: it corresponds to the peak V_{max} value of the halo along its main progenitor branch. We compute it by matching the `HaloIndex` of each halo at the z_A of interest with the `HaloIndex_mainprog` of all its progenitors from previous snapshots, both primary and secondary ones¹¹. We then assume $V_{\text{peak}}^{\text{cen}} \equiv V_{\text{peak}}^{\text{h}}$.
- *Cartesian positions*: we assume the 3-d spatial coordinates of the central halo center—`x_L2com[:,i=0,1,2]` in the ABACUSSUMMIT notation—to coincide with the center of mass of the largest L2 subhalo, meaning that:

$$\vec{r}_{\text{cen}} \equiv \vec{r}_{\text{h}} = (x_{\text{h}}, y_{\text{h}}, z_{\text{h}}). \quad (1)$$

- *Velocity dispersion*: we adopt the 3-d velocity dispersion (σ_{vd}) of the inner 50% of particles as a proxy for the entire halo. In ABACUSSUMMIT, this is called `sigmav3d_r50_L2com` and is estimated as the square root of the sum of eigenvalues of the second moment tensor of the velocities relative to the center of mass.

¹⁰ In ABACUSSUMMIT, L0 groups are large sets of DM particles typically encompassing several L1 groups. These correspond to classical halos, while L2 groups identify with “halo cores” or “subhalos”. For further details, see <https://abacussummit.readthedocs.io/en/latest/compaso.html>

¹¹ <https://abacussummit.readthedocs.io/en/latest/data-products.html>

⁹ <https://abacussummit.readthedocs.io/en/latest/>

Table 1. Observed number (N) and number density (n) at the effective redshift (z_{eff}) of the DESI Y1 ELG1 and LRG3 samples, as given in Adame et al. (2025b). We also show the redshift error (z_{err}) affecting our velocity estimates, the ABACUSUMMIT snapshot (z_A) used for modeling, and the UCHUU snapshot (z_U) chosen for calibration.

DESI Y1 sample	observed z range	z_{eff}	z_A	z_{err}	$N(z_{\text{eff}})$	$n(z_{\text{eff}}) \times 10^4$ [$h^3 \text{Mpc}^{-3}$]	z_U
ELG1	$0.8 < z < 1.1$	0.95	0.8	-0.06	99575	6.56	0.78
LRG3	$0.8 < z < 1.1$	0.95	0.8	-0.06	48491	3.40	0.78

- *Peculiar velocity*: assuming that the line-of-sight (LOS) is parallel to the \vec{z} direction, we adopt the center of mass LOS velocity of the largest L2 subhalo, which is `v_L2com[:,2]` in the ABACUSUMMIT notation. In this way, the peculiar velocity contribution to the central halo position in redshift space comes all from that of its host, v_z^h .

We modulate it further using a constant velocity bias parameter, b_{cen} (see Rocher et al. 2023):

$$v_z^{\text{cen}} = v_z^h + b_{\text{cen}} \sigma_{\text{vd}} \mathcal{N}(0, 1), \quad (2)$$

where $\mathcal{N}(0, 1)$ is a normal random realization with mean 0 and variance 1, and σ_{vd} is the halo velocity dispersion (see above).

- *Virial mass*: we calculate the host halo virial mass by multiplying the individual particle mass, `ParticleMassHMsun`, available in the header of the ABACUSUMMIT catalogs, by the number `N` of its particles. We assign $M_{\text{vir}}^{\text{cen}} \equiv M_{\text{vir}}^h$.
- *Virial radius*: we assign central halos their host virial radius, $R_{\text{vir}}^{\text{cen}} \equiv R_{\text{vir}}^h$. As a proxy for this quantity, we follow Rocher et al. (2023) and adopt the radius enclosing 98% of the halo mass relative to the L2 center, denoted `r98_L2com` in the ABACUSUMMIT catalog.
- *Type*: we flag all central halos with `type = 0` to distinguish them from satellites, which have `type = 1` (see § 3.2.2).

3.2. Satellite halos

Since the ABACUSUMMIT halo finder does not track satellite properties, these must be generated externally. This step is essential for HOME, which relies on abundance matching (AM) and therefore requires accurate satellite information.

We construct satellites by combining the properties of the ABACUSUMMIT DM particles and central host halos. Specifically, we build and assign each satellite the

following key quantities for HOME: $V_{\text{peak}}^{\text{sat}}$, x_{sat} , y_{sat} , z_{sat} , v_z^{sat} , M_{vir}^h , R_{vir}^h , `type = 1`. Here, the superscripts “sat” (“h”) indicates that the property refers to the satellite (parent host) halo.

Unless explicitly mentioned, in what follows we treat central and satellite V_{peak} values in the same manner, with no distinction, and we use the `type` flag whenever we need to discriminate them.

To assign satellite positions, we randomly select 30% of the DM particles available in *all* ABACUSUMMIT host halos (see § 2.2), which provide about 4.5×10^9 potential locations. This large reservoir of satellites has an impact on the conformity level and orphan satellite predictions of our model; see discussion in § 6.2.4.

By combining these particle properties with their hosts’ ones, and applying physically motivated prescriptions that we calibrate against predictions from the UCHUU N -body simulation, we generate the satellite population required for HOME. In the following, we describe how each satellite property is constructed.

3.2.1. Peak circular velocities

Implementing the abundance matching scheme in HOME requires rank-ordering both the ABACUSUMMIT halos and the DESI galaxy tracers by key properties. For halos, we adopt their peak circular velocity V_{peak} (§ 3.1), as it has been proven to correlate tightly with galaxy luminosity and stellar mass, representing an accurate proxy for abundance matching in general (see e.g., Reddick et al. 2013; Chaves-Montero et al. 2016).

Since ABACUSUMMIT does not provide satellite V_{peak} values, we sample them *conditional* to their host peak circular velocities using a cumulative distribution function (CDF) that we build in six steps:

1. We fit the ABACUSUMMIT host abundance, in bins of V_{peak} , at the z_A of interest using the analytic formula by Klypin et al. (2011):

$$n(V_{\text{peak}}, z) = A V_{\text{peak}}^{-3} \exp\left(-\left[\frac{V_{\text{peak}}}{V_0}\right]^\gamma\right), \quad (3)$$

which depends on 3 parameters and, implicitly, on redshift. We obtain $n_h^A(V_{\text{peak}}, z_A)$, whose optimal parameters $(A, V_0, \gamma)_h^A$ are given in Table 3. We explore their posterior distribution using a Monte Carlo Markov Chain (MCMC) coupled with an emcee sampler (Foreman-Mackey et al. 2013); the results are discussed in § 6.1.

- Using Eq. 3, we fit the satellite and central halo abundances predicted by the UCHUU N -body simulation (Ishiyama et al. 2021). This has 12800³ particles, as well as satellite properties, in the same volume as ABACUSSUMMIT ($L_{\text{box}} = 2 h^{-1} \text{Gpc}$), resulting in higher mass resolution, i.e. $3.28 \times 10^8 h^{-1} M_\odot$ ¹². We adopt the closest available UCHUU snapshot ($z_U = 0.78$, hereafter) to the observed effective redshift. The UCHUU abundance fits and results, with optimal parameters $(A, V_0, \gamma)_{\text{cen}}^U$ and $(A, V_0, \gamma)_{\text{sat}}^U$, are shown in § 6.1.
- From the central-to-satellite ratio of the UCHUU abundance fits, we calculate the correction factor:

$$R(V_{\text{peak}}, z_U) = \frac{n_{\text{cen}}^U(V_{\text{peak}}, z_U)}{n_{\text{sat}}^U(V_{\text{peak}}, z_U)}. \quad (4)$$

- We define the probability density function (PDF) to sample satellite V_{peak} values in ABACUSSUMMIT as that of their hosts, obtained from step 1 above, rescaled by the correction factor just computed:

$$n_{\text{sat}}^A(V_{\text{peak}}, z_A) = \frac{n_h^A(V_{\text{peak}}, z_A)}{R(V_{\text{peak}}, z_U)}. \quad (5)$$

- By integrating Eq. 5 and normalizing it to unity, we obtain the satellite V_{peak} CDF, conditional to their hosts:

$$\Psi_{\text{sat}}(V_{\text{peak}}, z_A) = \frac{\int_{V_{\text{low}}}^{V_{\text{peak}}} n_{\text{sat}}^A(V', z_A) dV'}{\int_{V_{\text{low}}}^{V_{\text{up}}} n_{\text{sat}}^A(V', z_A) dV'}. \quad (6)$$

Here, $V_{\text{low}} \equiv 0.2 V_{\text{peak}}^h$ and $V_{\text{up}} \equiv V_{\text{peak}}^h$ are the lower and upper velocity limits set by the hosts. We choose the lower limit to be 20% the host velocity to have an homogeneous V_{peak} distribution, when combining central and satellite halos. Lower than that, satellites are segregated to extremely low velocity values, which are unphysical.

- Finally, we inverse transform sampling the satellite V_{peak} values from Eq. 6, by drawing uniform random numbers $u_i \sim \mathcal{U}(0, 1)$, and solving:

$$V_{\text{peak}}^{i, \text{sat}} = \Psi_{\text{sat}}^{-1}(u_i), \text{ where } i = 1, \dots, N_{\text{sat}}, \quad (7)$$

at fixed z_A . In this way, the sampled satellite velocities follow the probability distribution set by the hosts.

3.2.2. Satellite positions and placement in hosts

We randomly place satellites at the ABACUSSUMMIT DM particle locations using a normalized particle-level occupation scheme.

First, for each host we compute its expected mean number of satellites using a power-law function of its virial mass (see e.g., Berlind & Weinberg 2002; Kravtsov et al. 2004; Zheng et al. 2005; Avila et al. 2020; Alam et al. 2021; Rocher et al. 2023; Yuan et al. 2025):

$$\langle N_{\text{sat}} \rangle = \left(\frac{M_{\text{vir}}^h - \kappa M_{\text{cut}}}{M_1} \right)^\beta, \quad (8)$$

to ensure that more massive hosts are assigned a larger number of satellites. Here, M_1 is the typical halo mass hosting one satellite, while M_{cut} (κM_{cut}) is the minimum halo mass to host a central (satellite) galaxy.

The parameter κ acts as a satellite-onset shifter: lowering κ allows satellites to populate lower-mass halos, boosting the 1-halo term and steepening the small-scale monopole and quadrupole, while increasing κ delays satellite formation to higher masses, reducing the satellite fraction and flattening small-scale clustering without affecting large-scale bias.

This expected number is then distributed across the halo's particles by assigning each particle a selection probability equal to:

$$p_{\text{sat}} = \frac{\langle N_{\text{sat}} \rangle}{N_p}, \quad (9)$$

where N_p is the total number of particles available per halo. We then perform a Bernoulli trial per particle, with retain probability p_{sat} , to decide whether or not a satellite will occupy its position. In case of success, we flag the particle with **type** = 1 to distinguish satellites from central mocks in the resulting catalog (see § 3.1).

This particle-level approach, where we directly sample satellite positions from particle locations, has the great advantage of preserving the spatial correlations of the underlying DM field, providing HOME natural anisotropy and stochasticity, especially on small scales (further details in Appendix A).

Dark matter particles in N -body simulations exhibit more centrally concentrated radial profiles within halos, compared to resolved satellite subhalos (e.g., Nagai & Kravtsov 2005; Gao et al. 2008). This difference arises since particles trace the full mass distribution, including regions where subhalos have been disrupted or stripped, while satellite catalogs only include resolved, surviving substructures.

¹² <https://www.skiesanduniverses.org/Simulations/Uchuu/>

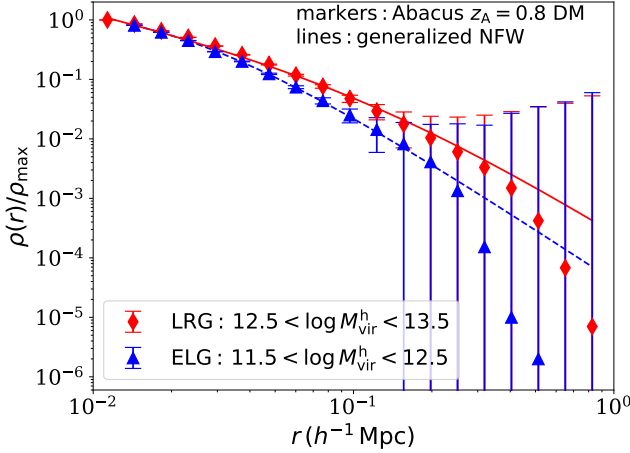


Figure 1. Radial profile of the ABACUSSUMMIT DM particles in hosts with typical ELG (blue triangles, dashed line) and LRG (red diamonds, solid line) halo virial masses, in units of $(h^{-1}M_{\odot})$. The error bars are the standard deviation in each radial bin.

As a result, satellite profiles are typically suppressed in the inner halo due to physical effects such as tidal disruption, dynamical friction, or finite resolution (e.g., van den Bosch et al. 2005; Behroozi et al. 2013a), as opposed to cuspy DM profiles, such as Navarro-Frenk-White (NFW; Navarro et al. 1997).

As shown in Figure 1, DM particles populating ABACUSSUMMIT halos with typical ELG ($3.2 \times 10^{11} - 3.2 \times 10^{12} h^{-1}M_{\odot}$) and LRG masses ($3.2 \times 10^{12} - 3.2 \times 10^{13} h^{-1}M_{\odot}$) naturally follow a generalized NFW profile:

$$\rho_A(r) = \frac{\rho_s}{\left(\frac{r}{r_s}\right)^{\delta} \left(1 + \frac{r}{r_s}\right)^{\eta-\delta}}, \quad (10)$$

where (ρ_s, r_s) are the scale parameters, and (δ, η) are the inner and outer slopes; their best-fit values are reported in Table 2.

For the above reasons, especially in high-resolution simulations, sampling satellites directly from the particle distribution, or from a pure NFW profile, systematically leads to an excess of clustering in projection on scales $r_p \lesssim 1 h^{-1}\text{Mpc}$. In redshift space, this is smeared by peculiar velocities, in a way that its impact on the anisotropic clustering becomes negligible.

In terms of intra-halo dynamics, such an excess has two contributions: (i) satellites too concentrated around the host in the halo core; (ii) satellite-satellite pairs where the two objects are too close to each other. The latter has a stronger impact on the clustering.

Whereas traditional HOD models often assumed that satellite galaxies follow a pure NFW profile—adequate on intermediate and large scales—modern analyses ex-

tend to sub-Mpc and kpc scales, where NFW tends to overpredict the number of close galaxy pairs.

To mitigate this excess, either one combines a radial suppression mechanism with a probabilistic core-suppression downsampling (see Appendix B) or, more easily and with less parameters, fine tunes the inner halo profile by modulating the relative distance between pairs, while preserving the outer halo profile. We choose this second strategy and explain it later on.

After directly sampling satellite positions from the ABACUSSUMMIT particle locations—so that our model inherits the full DM realism and structure—we modulate the cuspy particle profile to account for the observational evidence that ELGs preferentially occupy the outskirts of their host halos (e.g., Blanton & Berlind 2007; Wetzel et al. 2012; Chen et al. 2017; Kraljic et al. 2018; Guo et al. 2021; Dutta et al. 2024), while LRGs prefer the central regions (e.g., Tal et al. 2012; Hoshino et al. 2015).

In line with semi-analytic (e.g. Orsi & Angulo 2018) and HOD models (e.g., Avila et al. 2020; Rocher et al. 2023; Hadzhiyska et al. 2021a; Alam et al. 2021), that have successfully reproduced the ELG clustering properties by placing satellites in the outskirts of their hosts, we redefine the satellite positions as:

$$\vec{r}_{\text{sat}} \equiv \vec{r}_h + K_{\text{out}}(\vec{r}_{\text{dm}} - \vec{r}_h). \quad (11)$$

Here, $\vec{r} = (x, y, z)$ are the vectors of cartesian real-space¹³ positions, and K_{out} is a model parameter that changes the halo density profile acting as a scaling factor on the radial offset from the halo center. When DM particles are randomly selected, for $K_{\text{out}} = 1$ ($K_{\text{out}} = 0$), satellites occupy the particle (host) position, while $0 < K_{\text{out}} < 1$ pulls them towards the host center, and $K_{\text{out}} > 1$ pushes them outward into the halo outskirts. However, when DM particles go through non-random selection processes—such as the AM (§ 3.3) or the joint-occupation (§ 3.3.4) down-samplings— K_{out} compensates for the bias introduced by over-correcting the spatial profile (see also § 6.2.4).

To prevent the rescaling from unphysically ejecting satellites outside the virial boundary, we impose a physical cap on the effective displacement such that

$$|\vec{r}_{\text{sat}} - \vec{r}_h| \leq R_{\text{vir}}, \quad (12)$$

ensuring satellites remain bound within their parent halo.

By redefining the satellite positions through Eq. 11, HOME gains additional leverage to place satellites in

¹³ i.e., before applying redshift-space distortions due to peculiar velocities (§ 3.2.3)

Table 2. Best-fit parameters of the generalized NFW profiles for ABACUSSUMMIT DM particles in hosts with typical ELG and LRG masses, as shown in Figure 1.

$M_{\text{h}}^{\text{vir}} (h^{-1}\text{Mpc})$	$\rho_{\text{s}} (h^2\text{M}_{\odot} \text{Mpc}^{-3})$	$r_{\text{s}} (h^{-1}\text{Mpc})$	δ	η	$\chi^2/15 \text{ dof}$
$10^{11.5} - 10^{12.5}$	$(1.02 \pm 0.28) \times 10^{-2}$	25.03 ± 10.44	-1.65 ± 0.51	2.90 ± 0.16	1.7
$10^{12.5} - 10^{13.5}$	0.17 ± 0.18	0.11 ± 0.18	0.71 ± 0.07	6.06 ± 4.66	2.3

different regions of their host halos depending on the galaxy population. This flexibility is key to match the distinct 1-halo clustering signatures of ELGs and LRGs.

3.2.3. Peculiar motions

Inspired by Orsi & Angulo (2018), we model satellites as *coherent flows* with a velocity bias with respect to their host halos.

Assuming that the line-of-sight is parallel to the \hat{z} direction (see §3.1), we define the satellite peculiar motions as the sum of a radial and a tangential component—modulated by velocity bias parameters b_r and b_t —relative to their host, plus a random contribution proportional to the host velocity dispersion.

With the particle-host radial vector and unit direction given by:

$$\vec{r} = \vec{r}_{\text{dm}} - \vec{r}_{\text{h}}, \quad \hat{r} = \frac{\vec{r}}{|\vec{r}|}, \quad (13)$$

the radial and tangential velocity components are:

$$\begin{aligned} v_{\text{rad}} &= (\vec{v}_{\text{dm}} - \vec{v}_{\text{h}}) \cdot \hat{r}, \\ v_{\text{tan}} &= (\vec{v}_{\text{dm}} - \vec{v}_{\text{h}}) - \vec{v}_{\text{rad}} \text{ with } \vec{v}_{\text{rad}} = v_{\text{rad}} \cdot \hat{r}. \end{aligned} \quad (14)$$

Combining all these ingredients, the satellite peculiar velocity along the LOS is:

$$v_z^{\text{sat}} = v_z^{\text{h}} + b_r v_{\text{rad},z} + b_t v_{\text{tan},z} + \mathcal{N}(0, f_{\sigma} \sigma_{\text{vd}}), \quad (15)$$

where the host peculiar velocity, v_z^{h} , represents the coherent component, and the DM particle velocity v_z^{DM} the dispersed one.

The last term in Eq. 15 is a Gaussian random realization with zero mean and dispersion proportional to the DM velocity dispersion σ_{vd} (§3.1), rescaled by the f_{σ} parameter (Rocher et al. 2023). This term maintains the model realistic, avoiding artificial correlations.

The radial velocity bias, b_r , allows us to control the infall of satellites towards their hosts: $b_r < 1$ ($b_r > 1$) translates into slow (fast) infall motions, resulting in weaker (stronger) compression on $5 - 10 h^{-1}\text{Mpc}$ scales (Kaiser 1987).

As discussed in §6.2.3, peculiar intra-halo motions have strong impact on the satellite dynamics and are responsible of shaping the small-scale anisotropic clustering.

3.3. Halo Occupation Model (HOME)

To connect DESI ELGs and LRGs with their ABACUSSUMMIT host halos, we revisit the abundance matching (“AM”, hereafter) prescriptions by Rodríguez-Torres et al. (2016) and Favole et al. (2016b, 2017, 2022), and generalize them to galaxy multi-tracers. All these methods modify the standard AM (e.g., Conroy et al. 2006; Behroozi et al. 2010) recipe in different ways to account for the luminosity or stellar mass incompleteness of the galaxy sample to model, hence they are suitable for multi-tracer analyses.

The standard AM assumes that more massive (or luminous) galaxies occupy more massive halos, with deeper gravitational potential wells. In its basic version, the method rank-orders halos and galaxies based on some primary properties, and puts them in correspondence allowing some scatter between them.

On the halo side, we adopt V_{peak} as proxy for the halo mass, and use it to rank-order the ABACUSSUMMIT halos (see §3.2.1). Note that, at this stage of our model pipeline, the input halo catalog for HOME is composed of central (**type** = 0) and satellite (**type** = 1) halos including all the relevant properties to perform AM and clustering analysis—i.e., V_{peak} , positions, peculiar velocities—as built in the previous sections.

On the galaxy side, we consider as main property the stellar mass (M_{\star}) for both ELGs and LRGs. One could alternatively use the [O II] line (r -band) luminosity for ELGs (LRGs), but it is preferable to choose a unique consistent proxy for all tracers, so M_{\star} is more adequate.

We sample the M_{\star} values from the current fits (see Appendix D) to the star-forming (ELG) and quiescent (LRG) populations observed in COSMOS (Weaver et al. 2023). Besides the matching, we do not employ the stellar masses in our analysis.

Besides the minimal cut in the number of particles per halo (see §2.2), we also impose a lower velocity threshold, $V_{\text{peak}}^{\text{min}}$, that we fix for each galaxy sample to match its large-scale bias. This threshold is not free parameter in our model, and its values for ELGs and LRGs are reported in Table 4.

Between V_{peak} and M_{\star} , we allow a constant scatter in order to be physical. This is introduced by perturbing

V_{peak} using a random Gaussian realization (\mathcal{N}) with zero mean and dispersion σ_{AM} , which is a model parameter:

$$V'_{\text{peak}} = V_{\text{peak}} [1 + \mathcal{N}(0, \sigma_{\text{AM}})]. \quad (16)$$

In HOME, the abundance matching procedure establishes the galaxy–halo connection without distinguishing between central and satellite halos. However, during the construction of the mock catalog, each central (satellite) mock is flagged with `type=0 (1)`, enabling separation by type in what follows.

Once the basic catalog is assembled, further refinement can be achieved by matching secondary halo and galaxy properties conditioned on M_* (e.g., Favole et al. 2022), enhancing the predictive power of the high-fidelity mocks; we defer such extensions to follow-up work.

We then incorporate the ELG and LRG incompleteness effects by downsampling the final number of objects in the mock catalog to match the observed DESI Y1 ELG and LRG number densities (Adame et al. 2025a). This downsampling alters the shape of the stellar mass functions in § D by selecting ELG and LRG populations that are incomplete with respect to the original ones.

The downsampling is applied separately to central and satellite mocks—identified through the above `type` flag—using probability values computed in bins of V_{peak} , as (see Rodríguez-Torres et al. 2016; Favole et al. 2017):

$$p_{\text{cen (sat)}} = \frac{N_{\text{tot}}^{\text{cen (sat)}}(V_{\text{peak}})}{N_{\text{Gauss}}^{\text{cen (sat)}}(V_{\text{peak}})}, \quad (17)$$

each one normalized to unity.

Here, $N_{\text{tot}}^{\text{cen (sat)}}(V_{\text{peak}})$ are the total number of central (satellite) halos in bins of V_{peak} , meaning their velocity functions computed from the simulation. The $N_{\text{Gauss}}^{\text{cen (sat)}}(V_{\text{peak}})$ counterparts are central (satellite) Gaussian velocity functions that we compute from V_{peak} values sampled using a multi-tracer Gaussian PDF, which considers ELG and LRG as complementary populations. This is:

$$\begin{aligned} \phi(V_{\text{peak}}, V_{\text{elg}}, \sigma_{\text{elg}}, V_{\text{lrg}}, \sigma_{\text{lrg}}) = \\ w_{\text{elg}}(z) [\mathcal{G}_{\text{elg}}^{\text{cen}}(V_{\text{peak}}, V_{\text{elg}}, \sigma_{\text{elg}}) + \mathcal{G}_{\text{elg}}^{\text{sat}}(V_{\text{peak}}, V_{\text{elg}}, \sigma_{\text{elg}})] + \\ w_{\text{lrg}}(z) [\mathcal{G}_{\text{lrg}}^{\text{cen}}(V_{\text{peak}}, V_{\text{lrg}}, \sigma_{\text{lrg}}) + \mathcal{G}_{\text{lrg}}^{\text{sat}}(V_{\text{peak}}, V_{\text{lrg}}, \sigma_{\text{lrg}})], \end{aligned} \quad (18)$$

where $\mathcal{G}_{\text{elg}}^{\text{cen}}$ and $\mathcal{G}_{\text{elg}}^{\text{sat}}$ are *independent* Gaussian realizations for central and satellite ELG (LRG) mocks defined, in the same way, as a function of 4 model pa-

rameters:

$$\begin{aligned} \mathcal{G}_{\text{elg (lrg)}}^{\text{cen}}(V_{\text{peak}}, V_{\text{elg (lrg)}}, \sigma_{\text{elg (lrg)}}) = \\ \mathcal{G}_{\text{elg (lrg)}}^{\text{sat}}(V_{\text{peak}}, V_{\text{elg (lrg)}}, \sigma_{\text{elg (lrg)}}) = \\ \frac{1}{\sqrt{2\pi} \sigma_{\text{elg (lrg)}}} \exp \left[-\frac{1}{2} \left(\frac{V_{\text{peak}} - V_{\text{elg (lrg)}}}{\sigma_{\text{elg (lrg)}}} \right)^2 \right]. \end{aligned} \quad (19)$$

Here, the parameters $V_{\text{elg, (lrg)}}$ and $\sigma_{\text{elg, (lrg)}}$ represent the typical mean maximum circular velocities of the tracers, and the corresponding scatter.

We emphasize that the two Gaussian realizations—one for centrals and one for satellites—yield different outcomes, as the sampling is performed independently for each population.

The contribution of each tracer to the PDF in Eq. 18 is weighted by its observed number as a function of redshift (Adame et al. 2025a), i.e. $N_{\text{elg (lrg)}}(z)$. The ELG (LRG) weights are defined as:

$$w_{\text{elg (lrg)}}(z) = \frac{N_{\text{elg (lrg)}}(z)}{N_{\text{elg}}(z) + N_{\text{lrg}}(z)}, \quad (20)$$

so that, when modeling their auto-correlation functions, the complementary tracer does not contribute, since $N_{\text{lrg (elg)}}(z) = 0$.

Note that the full redshift evolution is accounted for only when working with a light-cone. For a fixed simulation snapshot, as in our case, we evaluate $N_{\text{elg (lrg)}}(z_{\text{eff}})$, as reported in Table 1.

The Gaussian realizations in Eq. 19 are normalized to match the observed ELG and LRG numbers in terms of 4 model parameters as:

$$\begin{aligned} \int (w_{\text{elg}} \mathcal{G}_{\text{elg}}^{\text{cen}} + w_{\text{lrg}} \mathcal{G}_{\text{lrg}}^{\text{cen}}) dV_{\text{peak}} = \\ (1 - f_{\text{sat}}^{\text{elg}}) N_{\text{elg}}(z) + (1 - f_{\text{sat}}^{\text{lrg}}) N_{\text{lrg}}(z), \end{aligned}$$

$$\begin{aligned} \int (w_{\text{elg}} \mathcal{G}_{\text{elg}}^{\text{sat}} + w_{\text{lrg}} \mathcal{G}_{\text{lrg}}^{\text{sat}}) dV_{\text{peak}} = \\ f_{\text{sat}}^{\text{elg}} N_{\text{elg}}(z) + f_{\text{sat}}^{\text{lrg}} N_{\text{lrg}}(z). \end{aligned} \quad (21)$$

This guarantees HOME sufficient flexibility to precisely and simultaneously model the ELG1 and LRG3 auto- and cross-correlation functions below $4 h^{-1}$ Mpc, where the 1–halo contribution to the clustering is particularly strong (Rocher et al. 2023).

3.3.1. Orphan treatment

The $f_{\text{sat}}^{\text{elg}}$ and $f_{\text{sat}}^{\text{lrg}}$ terms in Eq. 21 represent the *total* fractions of satellite ELGs and LRGs calculated with respect to the total number of objects in the final mock

catalog. Note that, in principle, these fractions can include:

- ELG (LRG) satellites orbiting a ELG (LRG) host, meaning a maximally conformal configuration;
- ELG (LRG) satellites living in a host of the complementary species, meaning minimal conformity;
- Orphans, i.e. satellites whose central host halos are not part of the resulting mock catalog.

Contrarily to SHAM models, standard HOD frameworks typically omit orphan satellites by construction because satellites are only populated in halos that already host a central. Only a few modified HOD schemes have explicitly allowed for orphans (see e.g. Pujol et al. 2017), despite growing evidence that their inclusion can be important for reproducing the small-scale clustering signal. This point has been emphasized in semi-analytic models, where disrupted or unresolved centrals naturally generate satellite populations without an identified host (e.g., Reddick et al. 2013; Behroozi et al. 2019).

In HOME, orphans are not parametrized nor constrained by the likelihood. Rather, the relative ELG and LRG orphan abundances emerge naturally and self-consistently within our forward model as pure predictions, as a direct consequence of applying the AM down-sampling of satellites to match the observed number densities of tracers (§3.3), halo exclusion, and the joint-occupation condition (§3.3.4). The resulting orphan fractions (see Table 4) are relatively high by construction, since potential satellite candidates are drawn from the full pool of ABACUSUMMIT DM particles—including those belonging to host halos that are not included in the final mock catalog (§3.2).

3.3.2. Halo exclusion

Halo exclusion refers to the physical constraint that DM halos cannot overlap in space due to their finite sizes (e.g., Asgari et al. 2023). This leads to a suppression of clustering power on small scales and introduces a scale-dependent bias, particularly relevant in the transition between the 1-halo and 2-halo regimes.

In observational data, halo exclusion manifests as a deficit of close galaxy pairs residing in distinct halos, visible in the two-point correlation functions at small separations.

In N -body simulations, exclusion arises naturally from halo finding algorithms—such as Friends-of-Friends (e.g., More et al. 2011a), Spherical Overdensity (e.g., Knebe et al. 2011), or Rockstar (Behroozi et al. 2013b)—where halos are defined as non-overlapping entities. Its effect is especially prominent for massive ha-

los, where the exclusion scale can reach up to several Mpc.

From the modeling perspective, halo exclusion has been successfully incorporated in fast methods for covariance mock generation (see Kitaura et al. 2016). Here, the HADRON (Zhao et al. 2015) approach probabilistically assigns halo masses while accounting for both local and non-local environmental effects, including minimum distance constraints to suppress unphysical clustering among massive halos.

Analytical halo models have incorporated this effect by modifying the 2-halo term with exclusion corrections, using either step-function or soft-exclusion schemes (see e.g., Baldauf et al. 2013; van den Bosch et al. 2013).

HOD frameworks naturally incorporate exclusion by enforcing one central galaxy per halo and restricting the distribution of satellites accordingly. This approach has been successful in modeling SDSS and DES data (see e.g., Zheng et al. 2005; More et al. 2011b; Tinker et al. 2012; Zu & Mandelbaum 2018). Recent observational models incorporate refined exclusion treatments to improve parameter inference and consistency with lensing measurements (e.g., Leauthaud et al. 2017).

Hydrodynamical simulations, as IllustrisTNG, EAGLE, or Horizon-AGN, confirm that halo exclusion persists even when baryonic physics is included. Baryonic processes can alter halo profiles and sizes, but the fundamental exclusion scale remains tied to the DM distribution. These simulations show that models lacking exclusion cannot accurately reproduce galaxy–galaxy lensing or clustering measurements (e.g., Artale et al. 2018).

Halo exclusion has been recently integrated also in the modeling of line-intensity mapping, together with non-linear bias, in a physically motivated and simulation-validated framework (Jun et al. 2025).

In light of these results, we incorporate halo exclusion in HOME by suppressing the probability, for pairs of massive halos (i.e., more massive than a given threshold, M_{excl}), to be closer than a given (small) exclusion radius, r_{excl} . This translates into the condition:

$$\text{If } \begin{cases} M_{\text{vir}}^{\text{cen}, i} > M_{\text{excl}} \\ M_{\text{vir}}^{\text{cen}, j} > M_{\text{excl}} \\ |r_i - r_j| < r_{\text{excl}} \end{cases} \quad (22)$$

$$\Rightarrow \text{randomly remove } i \text{ or } j \text{ with probability } p_{\text{excl}}, \quad (23)$$

where r_{excl} , M_{excl} and p_{excl} are model parameters.

In practice, we apply the exclusion condition to the HOME input catalog—composed of central hosts and satellites—just before sampling the V_{peak} values from the Gaussian PDF (Eq. 18). In this way, we ensure that close, massive pairs are excluded prior to galaxy

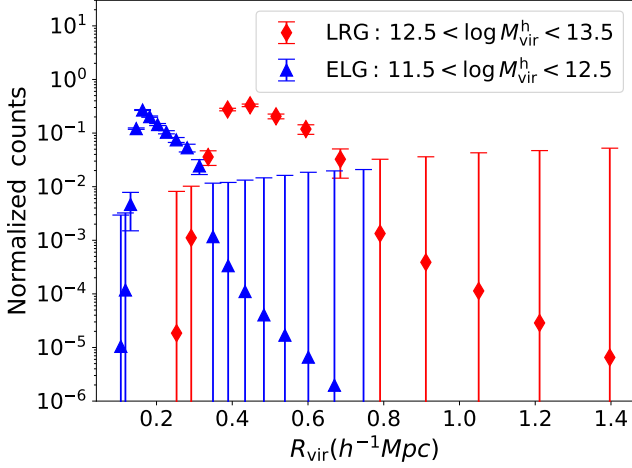


Figure 2. Normalised R_{vir} distribution of the ABACUSSUMMIT central host halos of ELG and LRG.

assignment. This approach naturally embeds exclusion physics into the mock-building process, while preserving the normalization of the PDF above.

Because our exclusion is keyed to the host mass, dropping a massive host automatically drops all of its bound (non-orphan) satellites, i.e. no extra satellite cut is needed there. Hence, the only place where satellite exclusion matters is for orphans, which carry the mass tag of their original hosts from the ABACUSSUMMIT simulation, but these hosts are missing in the HOME input catalog. If left unmitigated, orphans from massive hosts behave like low-mass centrals, adding central–central-like pairs and inflating w_p on $\sim 8 - 10 h^{-1}$ Mpc scales. Therefore, excluding satellites besides centrals, primarily serves to regulate further the presence of orphans in the final mock catalog (i.e., besides mitigating it via f_{orph}) and its impact on non-orphans is redundant once host-based exclusion is in place.

Figure 2 presents the normalized distribution of virial radii (R_{vir}), for ABACUSSUMMIT halos selected within mass ranges typical of ELGs ($3.2 \times 10^{11} - 3.2 \times 10^{12} h^{-1} M_{\odot}$) and LRGs ($3.2 \times 10^{12} - 3.2 \times 10^{13} h^{-1} M_{\odot}$), following the same selection as in Figure 1. While ELG host halos typically peak at $R_{\text{vir}} \sim 0.2 h^{-1} \text{Mpc}$, and extend up to $\sim 0.7 h^{-1} \text{Mpc}$, LRG hosts are substantially larger, peaking around $\sim 0.5 h^{-1} \text{Mpc}$ and reaching up to $\sim 1.4 h^{-1} \text{Mpc}$.

These distributions imply that, for most ELG (LRG) halos, the 2-halo regime starts beyond $R_{\text{vir}} \sim 0.4 h^{-1} \text{Mpc}$ ($0.8 h^{-1} \text{Mpc}$), the latter marking the scale where exclusion between pairs of more massive central halos becomes significant.

3.3.3. ELG and LRG class assignment

We stochastically classify galaxies into ELG or LRG tracers while constructing the mock catalog, using the two-component Gaussian mixture model in Eq. 18. The classification is performed on the fly—separately for central and satellite halos—during the mock assembly, enabling us to track how the combined ELG and LRG HOD is progressively constructed within HOME.

For centrals, the assignment is mutually exclusive by construction. We first assign LRG centrals following their selection probability. Once a halo is flagged as an LRG host, it is removed from the pool of available central halos to prevent reassignment. ELG centrals are then selected from the complementary halo population. This sequential procedure guarantees that a halo hosts at most one central galaxy in the final catalog, preserving physical consistency.

For satellites, however, the assignment is not exclusive to the host tracer type, since any satellite selected from the particle reservoir may inhabit a halo regardless of whether its central is an ELG or LRG. This design naturally allows:

- ELG satellites in LRG hosts, characterizing the environmental quenching regime;
- LRG satellites in ELG hosts, an observationally rare but permitted configuration,

thereby enabling the forward model to predict cross-tracer satellite populations and reveal potential central–satellite conformity.

In practice, for each sampled V_{peak} value¹⁴, we evaluate the unnormalized posterior probabilities:

$$p_{\text{elg}}(\text{lrg})(V_{\text{peak}}) = w_{\text{elg}}(\text{lrg})(z) \mathcal{G}(V_{\text{peak}} | V_{\text{elg}}(\text{lrg}), \sigma_{\text{elg}}(\text{lrg})), \quad (24)$$

which define the normalized ELG-class probability:

$$P_{\text{elg}}(V_{\text{peak}}) = \frac{p_{\text{elg}}(V_{\text{peak}})}{p_{\text{elg}}(V_{\text{peak}}) + p_{\text{lrg}}(V_{\text{peak}})}. \quad (25)$$

A uniform draw $u \sim \mathcal{U}(0, 1)$ then determines the label:

$$\text{class}(V_{\text{peak}}) = \begin{cases} \text{ELG,} & \text{if } u < P_{\text{elg}}(V_{\text{peak}}) \\ \text{LRG,} & \text{otherwise} \end{cases} \quad (26)$$

Thus, HOME performs probabilistic Bayesian classification for centrals and satellites, while enforcing central exclusivity and preserving the freedom for physically motivated cross-tracer satellite configurations.

¹⁴ Remember that the sampling is performed separately for centrals and satellites, hence classes are assigned accordingly.

3.3.4. Modeling environmental quenching through the joint halo occupation of ELGs and LRGs

Understanding the mechanisms that drive galaxy quenching, i.e. the cessation of star formation, remains one of the central challenges in galaxy evolution.

Satellite galaxies, in particular, are observed to quench rapidly upon infall into dense environments. Observations show that ELGs cease star formation shortly after entering the potential wells of massive hosts (e.g. Guo et al. 2021; Wetzel et al. 2013; Hirschmann et al. 2014; Rhee et al. 2024).

Large cluster surveys support a delayed-then-rapid scenario in which satellites continue forming stars for roughly 1-2 Gyr after infall before undergoing a rapid shutdown (e.g. Wetzel et al. 2013; Haines et al. 2015). Baxter et al. (2023) further identify two dominant pathways: core quenching, acting swiftly on satellites reaching the inner regions of their hosts, and starvation, a slower process driven by the exhaustion of gas in the outskirts.

Recent IFU surveys, such as K-CLASH, also show evidence for environmental quenching induced by ram-pressure stripping and strangulation, i.e. the halt of cosmic gas inflow (Vaughan et al. 2020).

On the theoretical side, semi-analytic and hydrodynamical studies find that strangulation dominates quenching in low-mass galaxies, while ram-pressure stripping or overconsumption are more efficient at high redshift or in dense environments (Peng et al. 2015; McGee et al. 2014).

Numerical simulations, such as AREPO, confirm a two-phase picture in which gas depletion via starvation precedes rapid stripping during pericentric passages (Steinhauser et al. 2016).

Machine-learning analyses of cosmological simulations also identify black-hole mass and central potential depth as key predictors of quenching in massive systems, highlighting AGN feedback as the principal internal mechanism (Piotrowska et al. 2022; Bluck et al. 2023). Taken together, these results support a dual-channel view of galaxy quenching: internal AGN feedback dominates in massive centrals, while environment-driven processes govern the shutdown of star formation in satellites.

In HOME, we emulate environmental quenching statistically, through a joint-occupation condition that regulates the co-existence of ELGs and LRGs within the same halos. Instead of explicitly evolving star-formation histories, we modulate the ELG occupation probability by the local density field traced by massive LRG hosts, effectively suppressing the presence of star-forming galaxies in dense environments.

For each ELG halo i , we compute a kernel-weighted suppression field:

$$S_i = \sum_j \left[\frac{M_{\text{vir},j}^{\text{lr}}}{M_0} \right]^{m_{\text{slope}}} \exp \left[- \left(\frac{r_{ij}}{R_0} \right)^\delta \right], \quad (27)$$

where r_{ij} is the comoving separation between the ELG candidate and the j -th LRG host. Here, $M_{\text{vir},j}^{\text{lr}}$ is the LRG halo virial mass, while the M_0 is the threshold mass above which a LRG halo is considered massive enough to influence ELG quenching in its vicinity.

The kernel decays exponentially with distance over a characteristic scale R_0 , while the exponent δ controls its steepness, and the mass-weighting term, m_{slope} , enhances the contribution of massive hosts. This effectively encodes the environmental influence of nearby LRG halos, i.e. those most likely to drive quenching through tidal interactions, ram-pressure stripping, or starvation.

In practice, we apply the joint-occupation condition by rescaling the baseline AM probability for a halo to be populated by an ELG—i.e., $p_{\text{elg}}(V_{\text{peak}})$ in Eq. 24—via the above suppression field, as:

$$p_{\text{elg}}^{\text{joint}}(V_{\text{peak}}) = p_{\text{elg}}(V_{\text{peak}}) \exp(-\alpha S_i), \quad (28)$$

where the parameter α controls the strength of environmental suppression. Here, high-density regions (i.e., large S_i values), correspond to LRG-dominated environments where quenching is efficient, yielding a smaller $p_{\text{elg}}^{\text{joint}}$, while isolated regions retain high ELG occupation probabilities.

This exponential coupling therefore emulates quenching statistically, that is reducing the abundance of central and satellite ELGs near massive hosts, without the need for an explicit treatment of gas physics or feedback.

As such, the joint occupation model serves as a phenomenological but physically motivated proxy for environmental quenching, connecting the observed scarcity of star-forming ELGs in cluster cores with the underlying DM halo distribution.

4. HIERARCHICAL BAYESIAN INFERENCE FRAMEWORK

We adopt a *two-level hierarchical Bayesian inference model* designed to account for the uncertainty and physical realism in the generation of mock catalogs for galaxy multi-tracers based on precise N -body simulations.

Our aim is to forward model the observed clustering statistics (\mathbf{D} , hereafter) using mock catalogs generated coupling the ABACUSSUMMIT host halo properties with the latent properties that we build for satellites.

These latent satellite variables are constructed—conditional to their host and DM particle properties—using analytic prescriptions based on a set of physically motivated nuisance parameters (θ , hereafter).

Incorporating θ in the likelihood used for cosmological inference would require regenerating the full set of latent variables for all halos at every point in parameter space—a task that is computationally prohibitive. To overcome this, we structure our inference strategy in two steps:

- **Level-I inference:** we generate the latent variables by calibrating the nuisance parameters θ against independent predictions from the UCHUU N -body simulation (Ishiyama et al. 2021); this has the same volume as ABACUSSUMMIT, but higher resolution, and it includes substructures. We then use the UCHUU posterior distribution to sample Gaussian priors to build the latent catalogs we need as inputs for HOME in the next step.
- **Level-II inference:** we build high-fidelity mock catalogs by coupling level-I posterior samples (i.e., the latent catalogs above) with our Halo Occupation Model, which depends on a set of physically motivated parameters, ϕ . Using these mocks, we forward-model the clustering statistics to constrain ϕ .

The above separation allows us to decouple the expensive generative step—i.e., producing and assigning the latent satellite variables to the ABACUSSUMMIT hosts) from the cosmological inference—at the cost of approximating the marginalization over θ using a finite number of latent sample realizations.

The HOME workflow, including all its parameters and the physical processes they drive, is schematically illustrated in Figure 3.

4.1. Posterior formulation

The full posterior distribution over all parameters is:

$$P(\phi, \theta | \mathbf{D}) \propto P(\mathbf{D} | \phi, \mathcal{C}(\phi, \theta)) P(\mathcal{C}(\phi, \theta) | \theta) P(\phi) P(\theta), \quad (29)$$

where:

- $P(\mathcal{C}(\phi, \theta) | \theta)$ encodes the generation of the mock catalog $\mathcal{C}(\phi, \theta)$ based on both the nuisance (θ) and the HOME (ϕ) parameters;
- $P(\mathbf{D} | \phi, \mathcal{C})$ represents the likelihood of the observations, given a forward model evaluated on the mock catalog \mathcal{C} ;
- $P(\theta)$ and $P(\phi)$ are priors on the nuisance and model parameters, respectively.

4.2. Likelihood structure

Since jointly sampling the posterior in Eq. 29 is computationally unfeasible, we split the inference in two levels, that we detail here.

4.2.1. Level-I: nuisance parameter calibration

We group our 9 nuisance parameters, which are defined in § 3.2.1, in the vector:

$$\theta = \{(A, V_0, \gamma)_h^A, (A, V_0, \gamma)_{\text{cen}}^U, (A, V_0, \gamma)_{\text{sat}}^U\}, \quad (30)$$

where the 3 sets of (A, V_0, γ) values—one for the ABACUSSUMMIT hosts, and the others for UCHUU central and satellite halos—govern the satellite V_{peak} sampling conditional to their host velocities.

To marginalize over θ , we calibrate the analytic prescriptions in § 3.2.1 against external predictions (\mathcal{D}_{sim} , hereafter) from the UCHUU N -body simulation (Ishiyama et al. 2021); the results are discussed in § 6.1.

In this way, the analytic prescription used to sample satellite V_{peak} values in ABACUSSUMMIT, that shapes our galaxy-halo connection model, is informed by precise DM distribution, ensuring that the latent satellite variables are consistent with the gravitational dynamics.

As a result, we infer the level-I posterior distribution:

$$P(\theta | \mathcal{D}_{\text{sim}}) \propto P(\mathcal{D}_{\text{sim}} | \theta) P(\theta), \quad (31)$$

from which we sample $N = 30$ sets of parameters $\{\theta_i\}_{i=1}^N$ that we use as Gaussian priors to generate corresponding realizations of the latent catalog (see below).

4.2.2. Level-II: forward modeling and likelihood averaging over latent realizations

In the second stage of our inference pipeline, we construct high-fidelity mock galaxy catalogs, denoted as $\mathcal{C}_i(\phi, \theta_i)$, by coupling the N latent realizations $\{\theta_i\}_{i=1}^N$ obtained from level I with our physically motivated HOME prescriptions driven by 37 parameters grouped in the vector:

$$\begin{aligned} \phi = & \{(\kappa, M_{\text{cut}}, M_1, \beta)^{\text{elg}}, K_{\text{out}}^{\text{elg}}, (b_{\text{cen}}, b_r, b_t, f_{\sigma})^{\text{elg}}, \\ & (\sigma_{\text{AM}}, V, \sigma_V)^{\text{elg}}, f_{\text{sat}}^{\text{elg}}, (M_{\text{excl}}, r_{\text{excl}}, p_{\text{excl}})^{\text{elg}}, \\ & (\kappa, M_{\text{cut}}, M_1, \beta)^{\text{lrg}}, K_{\text{out}}^{\text{lrg}}, (b_{\text{cen}}, b_r, b_t, f_{\sigma})^{\text{lrg}}, \\ & (\sigma_{\text{AM}}, V, \sigma_V)^{\text{lrg}}, f_{\text{sat}}^{\text{lrg}}, (M_{\text{excl}}, r_{\text{excl}}, p_{\text{excl}})^{\text{lrg}}, \\ & (M_0, R_0, m_{\text{slope}}, \delta, \alpha)\}, \end{aligned} \quad (32)$$

where, for both tracers, we have:

- $(\kappa, M_{\text{cut}}, M_1, \beta)$: HOD parameters determining the number of satellites assigned per host at their DM particle locations (see § 3.2.2);

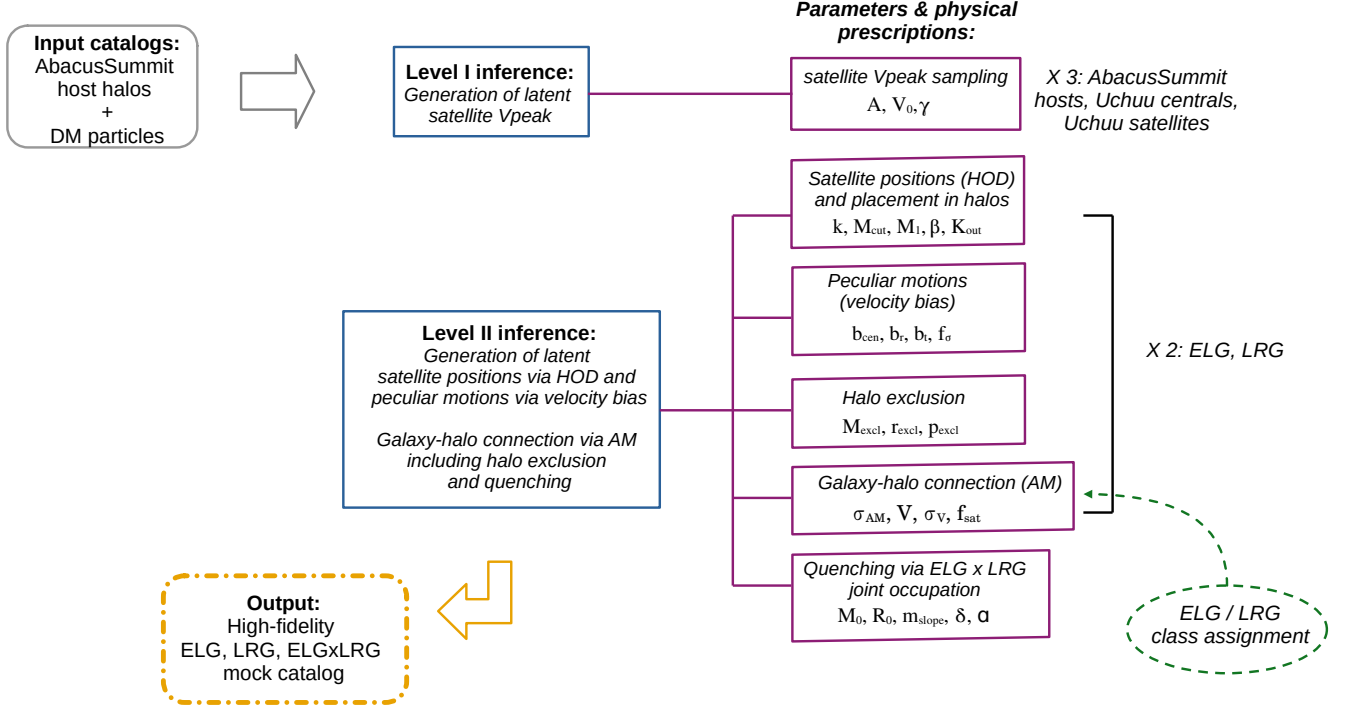


Figure 3. Schematic illustration of the HOME workflow. We start from the ABACUSUMMIT input halo and DM particle catalogs and generate the latent satellite V_{peak} values in level-I inference. In level II, we apply the HOME HOD prescription to assign satellite positions from DM particles, and the velocity bias model to generate their peculiar motions. Then, we perform galaxy-halo connection via abundance matching, probabilistically assigning ELG/LRG classes to the halos. Just prior to the matching, in the HOME input catalog we model halo exclusion. We then mimic the environmental quenching of ELG satellites in massive LRG hosts statistically, through the joint occupation condition. Finally, by constraining HOME physical parameters (37 in total) of our level-II inference, we obtain the high-fidelity mock catalog for DESI multi-tracers.

- K_{out} : regulates the spatial distribution of satellites within halos (§ 3.2.2);
- $(b_{\text{cen}}, b_r, b_t, f_\sigma)$: control central and satellite peculiar motions, modulating redshift-space distortions (§ 3.1, 3.2.3);
- $(\sigma_{\text{AM}}, V, \sigma_V)$: parametrize abundance matching (§ 3.3);
- f_{sat} : normalize the final halo occupation based on the observed number density of tracers (§ 3.3).
- $(M_{\text{excl}}, r_{\text{excl}}, p_{\text{excl}})$: drive the halo exclusion mechanism in massive tracers (§ 3.3.2);

and for the joint occupation condition:

- $(M_0, R_0, m_{\text{slope}}, \delta, \alpha)$: regulate the coexistence of ELGs and LRGs in the same halos mimicking the effect of environmental quenching (§ 3.3.4).

To constrain the full parameter space of ϕ , we explore its posterior distribution using MCMC sampling. For each proposed set of ϕ , we generate $N = 30$ mock

realizations $\mathcal{C}_i(\phi, \theta_i)$ by applying HOME to each of the 30 latent halo configurations θ_i . The model likelihood is then approximated by averaging over the N mocks as:

$$P(\phi | \mathbf{D}) \propto P(\phi) \cdot \frac{1}{N} \sum_{i=1}^N P(\mathbf{D} | \mathcal{C}_i(\phi, \theta_i)), \quad (33)$$

where each term in the average likelihood above is a Gaussian likelihood.

Assuming the data are divided in N_b bins, normally distributed around the model prediction \mathcal{C}_i , and that the total uncertainty—encompassing both data (d) and mock (m) contributions—is captured by the covariance matrix \mathbf{C}_{tot} (see § 5 for details on its computation),

$$\mathbf{C}_{\text{tot}} = \mathbf{C}_{\text{d}} + \mathbf{C}_{\text{m}}, \quad (34)$$

each individual likelihood in Eq. 33 takes the form:

$$\begin{aligned} \log P(\mathbf{D} | \mathcal{C}_i(\phi, \theta_i)) = & \\ & - \frac{1}{2} [\mathbf{D} - \mathcal{C}_i(\phi, \theta_i)]^T \mathbf{C}_{\text{tot}}^{-1} [\mathbf{D} - \mathcal{C}_i(\phi, \theta_i)] \\ & - \frac{1}{2} \log \det \mathbf{C}_{\text{tot}} - \frac{N_b}{2} \log(2\pi), \end{aligned} \quad (35)$$

where $N_b = 25$ is the number of spatial bins we use to measure the clustering statistics \mathbf{D} (see § 5).

This Monte Carlo marginalization provides a tractable way to account for uncertainty in the latent halo properties θ_i without regenerating them for every step in parameter space. As a result, we are able to propagate cosmological and nuisance uncertainties from the halo level to the final galaxy statistics in an efficient and robust way.

5. CLUSTERING MEASUREMENTS AND FITS

We employ the two-point correlation function (2PCF) measurements of the DESI Y1 ELG1, LRG3 and ELG1×LRG3 samples (Ross et al. 2025; Adame et al. 2025a). Specifically, we consider the first two even multipoles, $\xi_{l=0,2}(s)$, computed as (Chuang & Wang 2013):

$$\xi_l(s) = \frac{2l+1}{2} \int_{-1}^1 \xi(s, \mu) L_l(\mu) d\mu, \quad (36)$$

where L_l is the l -th order Legendre polynomial, and the projected function (Davis & Peebles 1983):

$$w_p(r) = 2 \int_0^{\pi_{\max}} \xi(r_p, \pi) d\pi. \quad (37)$$

The correlation functions $\xi(s, \mu)$ in Eq. 36 and $\xi(r_p, \pi)$ in Eq. 37 are evaluated in $N_b = 25$ logarithmic bins of s (r_p), where $s = \sqrt{r_p^2 + \pi^2}$, between $0.17 h^{-1} \text{Mpc}$ and $32 h^{-1} \text{Mpc}$, 200 linear bins of μ in $[-1, 1]$, and 40 linear bins of π between zero and $\pi_{\max} = 40 h^{-1} \text{Mpc}$.

Together with the DESI Y1 measurements, we adopt the jackknife covariance matrices (\mathbf{C}_d) estimated from $N_{\text{res}} = 128$ re-samplings on the Y1 survey footprint (Ross et al. 2025).

Using the same binning scheme, we calculate the multipole and projected 2PCFs of the HOME high-fidelity mock catalog using the FCFC code (Zhao 2023) coupled with the natural estimator (Davis & Peebles 1983).

To estimate the mock covariances (\mathbf{C}_m), we impose the HOME best-fit configuration to the available $N_r = 1800$ realizations of the small ABACUSSUMMIT boxes (§ 2.2), and compute corresponding 2PCFs for each tracer. The model covariance for each tracer is then computed as:

$$\mathbf{C}_m = \frac{1}{N_{\text{res}} - 1} \sum_{i=1}^{N_{\text{res}}} \left(\mathbf{X}_m^{(i)} - \bar{\mathbf{X}}_m \right) \left(\mathbf{X}_m^{(i)} - \bar{\mathbf{X}}_m \right)^T, \quad (38)$$

where $\mathbf{X}_m = (\xi_0(s), \xi_2(s), w_p(r_p))$ is the grouped vector of the model clustering statistics, stacked on the same binning used in the likelihood, and $\bar{\mathbf{X}}_m$ its average over the $N_{\text{res}} = 1800$ realizations given by:

$$\bar{\mathbf{X}}_m = \frac{1}{N_{\text{res}}} \sum_{i=1}^{N_{\text{res}}} \mathbf{X}_m^{(i)}. \quad (39)$$

We jointly fit the monopole, quadrupole and projected correlation functions of each galaxy tracer under study (i.e., ELG1, LRG3, and ELG1×LRG3), and estimate its χ^2 as (e.g., Favole et al. 2021; Rocher et al. 2023):

$$\chi^2 = (\mathbf{X}_d - \mathbf{X}_m)^T \hat{\Psi} (\mathbf{X}_d - \mathbf{X}_m), \quad (40)$$

where $\hat{\Psi}$ is the total assembled precision matrix:

$$\hat{\Psi} = \left[\frac{\mathbf{C}_d}{(1 - H_d)} + \frac{\mathbf{C}_m}{(1 - H_m)} \right]^{-1}. \quad (41)$$

Here, $\mathbf{X}_{m(d)}$ is the grouped vector of the model (data) clustering statistics, and $H_{d(m)}$ their Hartlap factors computed as (Hartlap et al. 2007):

$$H_{d(m)} = (N_{\text{res}} - N_b - 2) / (N_{\text{res}} - 1), \quad (42)$$

with $N_b = 25$, and $N_{\text{res}} = 128$ (1800) in H_d (H_m).

Following Rocher et al. (2023) and Yuan et al. (2024), in the likelihood estimation we reduce the noise in the jackknife covariances by replacing their off-diagonal terms with those of the covariances from the 1800 small ABACUSSUMMIT mocks (see § 2.2). In this way, the resulting HOME covariances are more stable, their inversion is well-behaved, and the likelihood estimation more robust.

6. RESULTS

In what follows, we present the results of our DESI Y1 ELG and LRG clustering analysis structured as a two-level Bayesian inference scheme (see § 4).

First, we discuss level-I results, that is the validation of the posterior distributions of the nuisance parameters through independent N -body predictions (§ 6.1).

Then, we present and discuss our main findings from level-II inference: the HOME galaxy clustering predictions (§ 6.2.1) and halo occupation distribution (§ 6.2.4) for DESI Y1 galaxy multi-tracers.

6.1. Nuisance parameter posterior validation

We fit the abundance formula in Eq. 3 to the V_{peak} function of the ABACUSSUMMIT central hosts at $z_A = 0.8$. Then, we fit the same formula to the V_{peak} functions of the central and satellite halos in the UCHUU N -body simulation (Ishiyama et al. 2021) at $z_U = 0.78$ (see Table 1). From the UCHUU fits we calculate the correction factor (Eq. 4), which we use to build the CDF to sample V_{peak} values for the ABACUSSUMMIT satellites.

For consistency with ABACUSSUMMIT, we impose UCHUU a minimal $M_h^{\text{vir}} \geq 2.1 \times 10^{10} h^{-1} \text{M}_\odot$ cut, corresponding to $N_p \geq 65$ particles (§ 2.2).

Figure 4 compares the ABACUSSUMMIT and UCHUU V_{peak} functions (note that the central contributions in

Table 3. *Top:* best-fit parameters of the ABACUSSUMMIT host V_{peak} functions at the redshift snapshots of interest, compared with the UCHUU central and satellite results shown in Figure 4. The analytic function employed for fitting is given in Eq. 3. Next to each parameter, we report the Gaussian priors (\mathcal{N}) used to explore the posterior distributions shown in Figure 5.

z_{snap}	halo type	$A (h^{-1} \text{M}_{\odot} / s^{-1} \text{km})^{-3}$	$V_0 (s^{-1} \text{km})$	γ	χ^2/dof	dof
AbacusSummit						
z_A						
0.8	hosts	$52804^{+21}_{-21} \mathcal{N}(60000, 15000)$	$407.38^{+0.14}_{-0.15} \mathcal{N}(550, 200)$	$1.418^{+0.001}_{-0.001} \mathcal{N}(1.0, 0.5)$	1.79	25
Uchuu						
z_U						
0.78	satellites	$14585^{+10}_{-10} \mathcal{N}(18000, 8000)$	$297.36^{+0.09}_{-0.09} \mathcal{N}(450, 200)$	$1.777^{+0.002}_{-0.002} \mathcal{N}(1.5, 0.5)$	2.05	21
0.78	centrals	$39831^{+16}_{-16} \mathcal{N}(40000, 10000)$	$497.76^{+0.16}_{-0.16} \mathcal{N}(550, 200)$	$1.665^{+0.001}_{-0.001} \mathcal{N}(1.5, 0.5)$	2.19	25

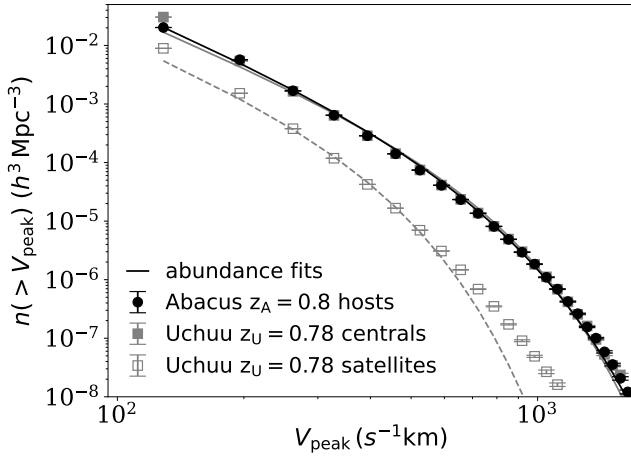


Figure 4. V_{peak} functions (markers), and corresponding best fits (lines) based on Eq. 3, for the ABACUSSUMMIT host halos (black dots), compared to the UCHUU central (grey full squares almost perfectly overlapping with the black dots) and satellite (grey empty squares) halos at the fiducial redshift. For UCHUU the closest snapshot to $z_A = 0.8$ is $z_U = 0.78$. The uncertainties are computed from 30 bootstrap re-samplings. All the results are normalized to the simulation volume, that is $(2 h^{-1} \text{Gpc})^3$ for both ABACUSSUMMIT and Uchuu. The optimal parameters are reported in Table 3. The posterior distributions are shown in Figure 5

both simulations almost perfectly overlap) with their best fits, whose optimal parameters are in Table 3.

We employ an emcee sampler to explore the full posterior distributions of both simulations; the results are presented in Figure 5.

From these posteriors, we sample Gaussian priors and use them to build the latent satellite catalogs needed as inputs for HOME in the second level of our inference process (§ 4.2.2). This approach enables us to validate the physical plausibility and predictive power of the nuisance parameters in Eq. 30.

6.2. HOME predictions

In what follows we present our main findings: the galaxy clustering and HOD predictions for the DESI Y1 ELG1, LRG3, and ELG1×LRG3 samples.

6.2.1. Galaxy clustering results

Figures 6, 7, and 8 compare the DESI Y1 ELG1, LRG3, ELG1×LRG3 monopole, quadrupole and projected correlation functions with our HOME high-fidelity mock.

We emphasize that a single model run outputs a unique mock catalog simultaneously fitting the ELG and LRG auto- and cross-correlation functions, both multipoles and projected.

The observational uncertainties are obtained from 128 jackknife re-samplings on the Y1 survey footprint (Ross et al. 2025). The errors on the models are obtained as the standard deviation of the 2PCFs measured from 1800 mocks constructed by applying the HOME best-fit configuration to 1800 realizations of the ABACUSSUMMIT $500 h^{-1} \text{Mpc}$ boxes (see § 2.2). The correlation matrices of the 1800 mocks from these small boxes are shown in Figure 9, while Figure 10 compares their clustering results with those of the HOME $2 h^{-1} \text{Gpc}$ high-fidelity mocks.

Note that we directly apply HOME with the parameters given in Table 4 to the 1800 small boxes, with only minor adjustments in the satellite fractions. For both tracers and their cross-correlation, the agreement between the small-box mocks and the high-fidelity results is very good across all scales. The small residual differences is mostly due to the limited volume of the $500 h^{-1} \text{Mpc}$ boxes, which amplifies sample variance and reduces the contribution of massive halos and long-wavelength modes, penalizing the strong 1-halo term in the ELG clustering (for which we need some retuning in the satellite fractions). Importantly, resolution is not a limiting factor here, since both the $500 h^{-1} \text{Mpc}$ and the $2 h^{-1} \text{Gpc}$ boxes have identical resolution.

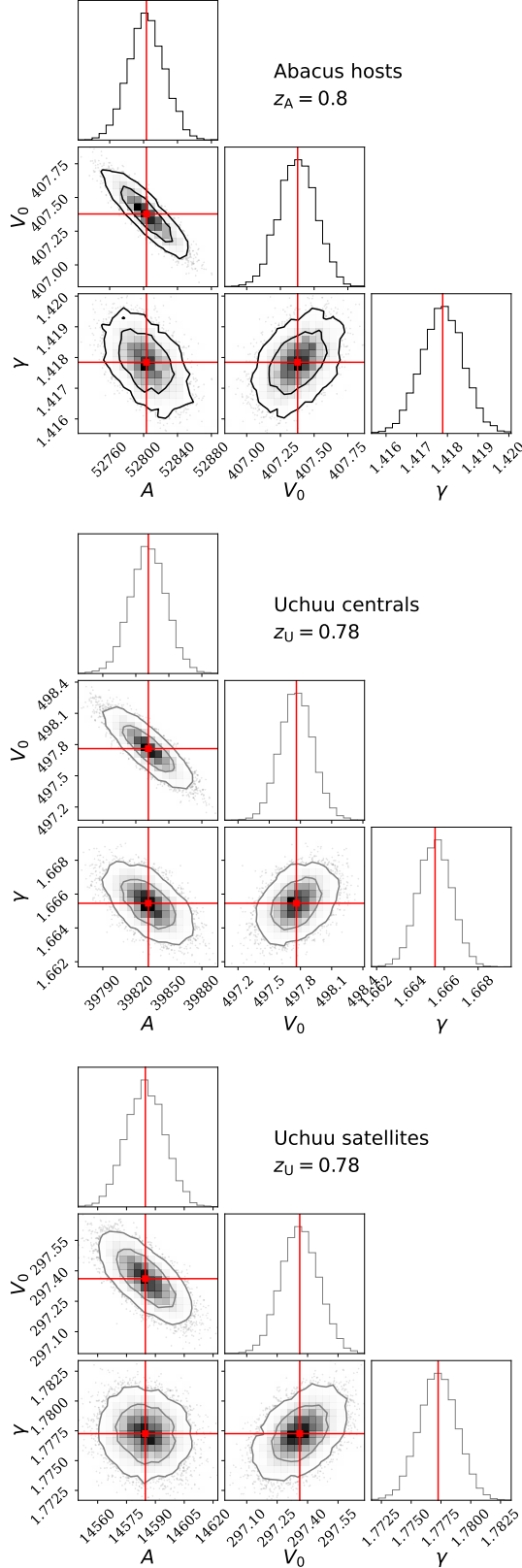


Figure 5. Posterior distributions of the halo abundance fit in Eq. 3 to the ABACUSSUMMIT hosts (top panel), UCHUU central (middle) and satellite (bottom) halos, as shown in Figure 4. The optimal parameters are reported in Table 3.

As previously done by Rocher et al. (2023) and Yuan et al. (2024), in estimating the model likelihood, we reduce the noise of the jackknife covariances by replacing their off-diagonal terms by those of the 1800 small-box covariances. The diagonal elements remain unaltered to preserve the jackknife variance.

The residuals between the HOME high-fidelity mock catalog and the observations, weighted by both uncertainties, are displayed in the lower panels of Figures 6–8. These show remarkable agreement (mostly within 5%) on all scales for all tracers and clustering statistics. The best-fit parameters and χ^2 values are in Table 4.

These results show that we accurately model the observed anisotropy in the Universe, capturing both the complex quadrupole shape on all scales and the strong 1-halo observed both in the monopole and in $w_p(r_p)$.

The model accuracy is particularly remarkable below $2 h^{-1} \text{Mpc}$, where achieving this level of agreement requires HOME to precisely characterize the dynamics of satellites within their host halos—which is highly tracer-dependent. This has strong impact on the conformity level required by DESI observations, which emerges from HOME as a pure prediction (see § 3.3.1 and 6.2.4).

The unprecedented accuracy we achieve in modeling the multi-tracer anisotropic clustering down to $s = 200 h^{-1} \text{kpc}$ enables us to impose stringent constraints on the ELG \times LRG halo occupation distribution, as well as the presence and contribution of orphan satellites to the clustering signal, and the ELG quenching mechanism.

This precision hinges primarily on the physical prescriptions driven by the satellite fraction parameters, $f_{\text{sat}}^{\text{elg, (lrg)}}$, the velocity biases (b_r , b_t , $b_{\text{cen}}^{\text{elg, (lrg)}}$), the halo exclusion levers (M_{excl} , r_{excl} , $p_{\text{excl}}^{\text{elg, (lrg)}}$), and the joint-occupation variables that emulate quenching (M_0 , R_0 , m_{slope} , δ , α).

A key feature of our forward modeling framework is that the $f_{\text{sat}}^{\text{elg, (lrg)}}$ entering the MCMC (Table 4, top part) are input parameters of the model, not direct predictors of the actual number of satellites in the final mock catalog. The *realized satellite fractions* (Table 4, bottom part) instead emerge self-consistently from the coupled AM down-sampling (§ 3.3), the stochastic class assignment scheme, the halo exclusion condition, and the joint-occupation quenching model (§ 3.3.4), which redistribute galaxies between central and satellite roles.

Our best-fit HOME predicts that 9.50% of ELG1 and 14.09% of LRG3 galaxies are satellites, while the remainder are centrals with no satellites. Among these satellites, 1.09% (ELGs) and 3.52% (LRGs) occupy halos whose central is of the same type (maximal conformity), whereas 7.02% (ELGs) and only 0.005% (LRGs) reside in halos hosting a central galaxy of the opposite type

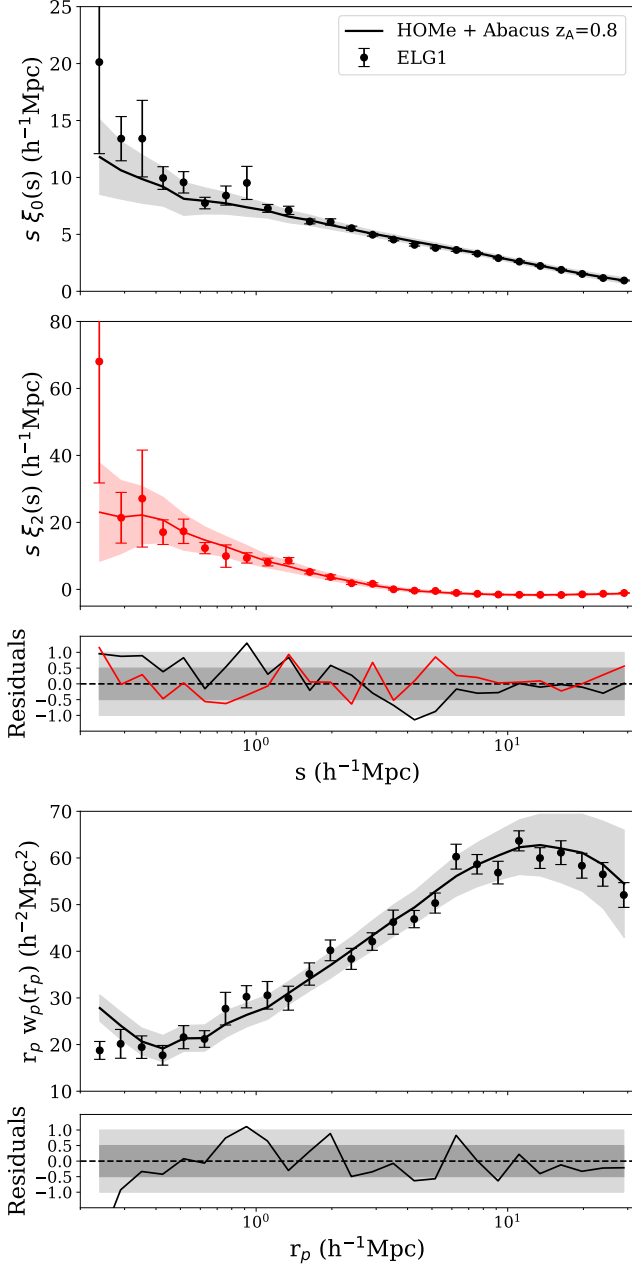


Figure 6. ELG1 monopole (*top panel*, black markers), quadrupole (*top panel*, red) and projected (*bottom panel*, black) auto-correlation functions, compared with the HOME high-fidelity mock (lines color-coded as the markers). The observational uncertainties are computed from 128 jackknife re-samplings on the data; those on the models from 1800 ABACUSUMMIT small boxes (details in the text). The lower panel below of each set of figures shows the residuals between data (d) and models (m), computed as $\text{Residuals} = (d - m) / \sqrt{\sigma_d^2 + \sigma_m^2}$. The grey shades represent the 5% (inner) and 10% (outer) confidence regions. The best-fit parameters are reported in Table 4.

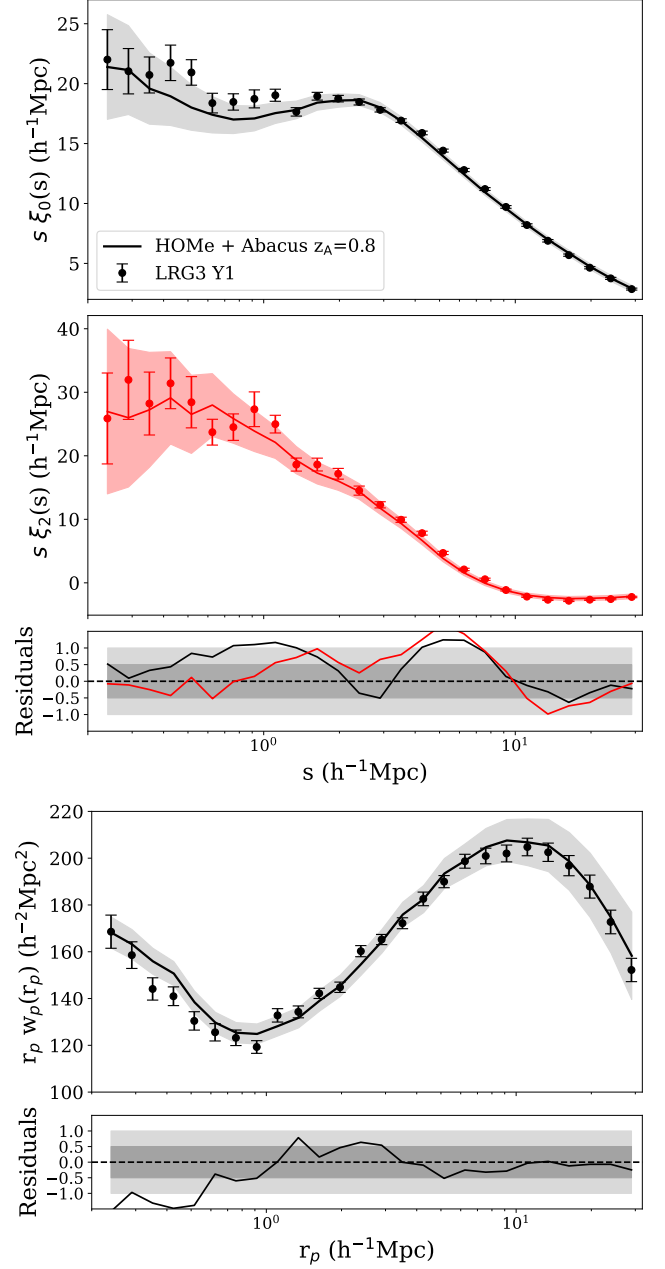


Figure 7. Same result as Figure 6, but for LRG3.

(minimal conformity). The remaining 0.58% (ELGs) and 10.57% (LRGs) are classified as orphans, i.e. satellites whose parent halos do not appear as centrals in the final realization.

According to our model, orphans tend to populate low-mass, low-bias halos that lack resolved substructure. On large scales, they redistribute galaxies toward lower-bias environments, suppressing both monopole and quadrupole amplitudes; on small scales, they retain satellite-like velocity dispersions and thus contribute to FoG damping.

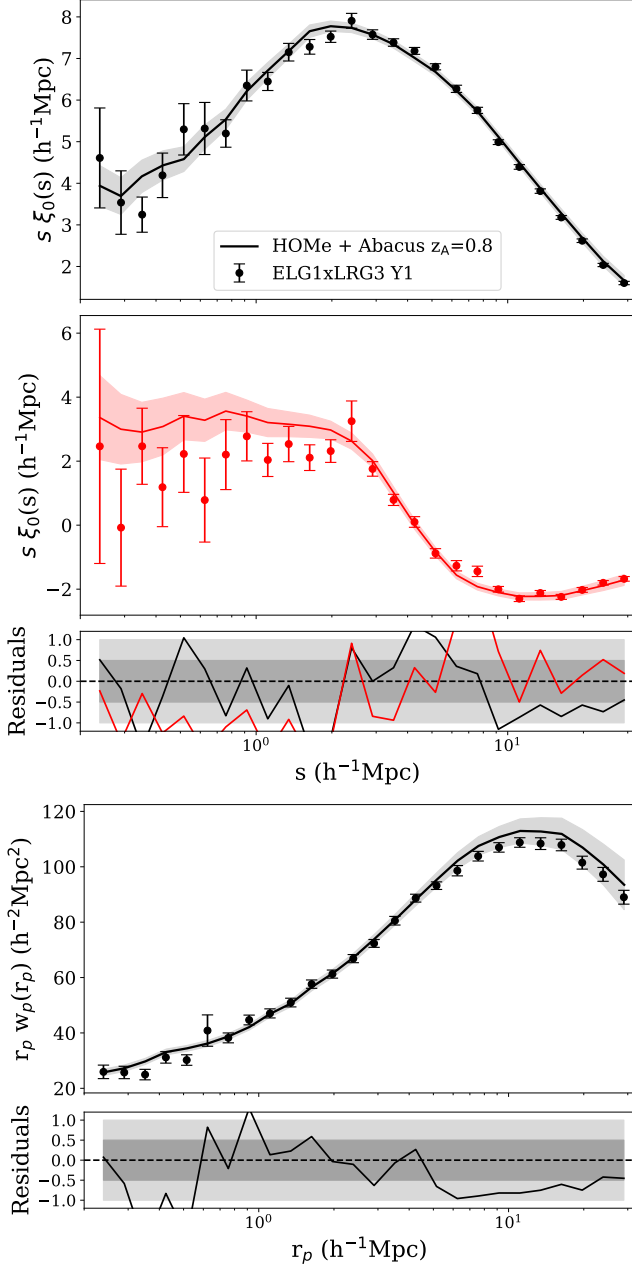


Figure 8. Same result as Figures 6–7, but for ELG1×LRG3.

From the above fractions, we infer that ELG satellites strongly favor minimally conformal environments, orbiting predominantly in LRG-host halos. Conversely, LRG satellites are mostly maximally conformal, orbiting around LRG centrals. The substantially larger orphan fraction among LRGs reflects the halo-selection hierarchy encoded in HOME: LRGs are assigned first and independently, whereas ELG satellites are conditioned on the already-populated LRG halo field.

The stark difference in orphan incidence between the two tracers has both a physical and modeling moti-

vation. For ELGs, the joint-occupation prescription (§3.3.4) suppresses ELG satellites in massive LRG hosts, such that many satellites that would otherwise be orphans are instead placed into LRG halos—consistent with observed environmental quenching. For LRGs, however, no such conditioning is imposed: their orphan fraction is therefore a pure forward-model prediction, reflecting the subhalo survival rates associated with their massive hosts and the resolution limits of the merger tree.

Understanding the astrophysical interpretation of this non-negligible LRG orphan population—including subhalo disruption and selection incompleteness—is an exciting direction for follow-up work, which we plan to pursue using state-of-the-art hydrodynamical simulations, such as IllustrisTNG.

The realized satellite fractions in HOME lie between those obtained in current SHAM analyses (Yu et al. 2022; Prada et al. 2025). They govern the entire small-scale anisotropy budget, especially for ELGs, whose clustering below $\sim 4 h^{-1}\text{Mpc}$ is dominated by 1-halo contributions (Rocher et al. 2023).

The satellite fraction and velocity bias (§6.2.3) exert complementary and competing effects on the anisotropic clustering on small and intermediate scales. While $f_{\text{sat}}^{\text{elg(lrg)}}$ primarily control the clustering amplitude, the radial and tangential velocity biases, b_r and b_t , govern redshift-space distortions. These effects manifest both in the so-called finger-of-god (‘FoG’) regime below $1 h^{-1}\text{Mpc}$, where random peculiar motions dominate, and on larger scales, around $10 h^{-1}\text{Mpc}$, where satellite coherent infall towards overdensities induces the Kaiser squashing.

In the 2-halo regime, a third effect becomes significant: the mutual exclusion between close pairs of massive hosts. This mechanism, particularly relevant to shape the 1-to-2-halo transition in the ELG1, LRG3 and ELG1×LRG3 monopole correlation functions.

Specifically, from our best-fit HOME we find that ELG1 (LRG3) halos with $\log(M_{\text{vir}}/(h^{-1}M_{\odot})) \gtrsim 13.45$ ($\log(M_{\text{vir}}/(h^{-1}M_{\odot})) \gtrsim 13.4$) are segregated by a minimum radial distance of about $2.3 h^{-1}\text{Mpc}$ ($3.2 h^{-1}\text{Mpc}$) from any other central tracer of the same mass. These exclusion scales mark the onset of nonlinear halo interactions, which are essential for accurately modeling the 1-to-2-halo transition in the clustering.

Another key ingredient in reproducing the ELG1×LRG3 cross-correlation is the joint-occupation condition, which acts as a phenomenological model for environmental quenching. In this prescription, each ELG candidate receives a kernel-weighted suppression factor that depends on the masses and distances of nearby LRG

Table 4. Best-fit values of the model input parameters for the DESI ELG1 and LRG3 tracers, producing the clustering signal in Figures 6–8. In parentheses we report the Gaussian priors adopted in the `emcee` sampler. Here the satellite fractions are total ones, i.e., computed with respect to the total number of mocks in the final catalog. We show the reduced χ^2 obtained by jointly fitting the multipoles and the projected auto- and cross-correlation functions of both tracers. We also report the realized values of total satellite and orphan fractions, together with the fraction of satellites that are maximally (minimally) conformal, i.e., occupying central hosts of the same (complementary) species. Note that these are pure predictions of our forward model resulting from the interplay of the AM down-sampling, halo exclusion, and joint occupation condition. The V_{peak} minimal selection cuts are shown at the bottom of the table; these are fixed values—i.e., not free parameters constrained in the likelihood—chosen to match the large-scale bias of each tracer.

Best-fit values (model inputs)		
Parameter / prescription	ELG	LRG
HOD (satellite positions)		
κ	$0.721^{+0.046}_{-0.049} \mathcal{N}(0.7, 0.2)$	$0.473^{+0.105}_{-0.096} \mathcal{N}(0.7, 0.20)$
$\log(M_{\text{cut}}/h^{-1}\text{M}_{\odot})$	$11.651^{+0.137}_{-0.138} \mathcal{N}(11.6, 0.3)$	$13.151^{+0.129}_{-0.090} \mathcal{N}(12.7, 0.3)$
$\log(M_1/h^{-1}\text{M}_{\odot})$	$11.801^{+0.071}_{-0.088} \mathcal{N}(11.6, 0.3)$	$13.402^{+0.145}_{-0.108} \mathcal{N}(13.6, 0.4)$
β	$0.634^{+0.110}_{-0.086} \mathcal{N}(0.6, 0.2)$	$0.992^{+0.109}_{-0.128} \mathcal{N}(0.8, 0.3)$
Satellite placement in halos		
K_{out}	$1.028^{+0.124}_{-0.117} \mathcal{N}(1.2, 0.3)$	$1.105^{+0.098}_{-0.114} \mathcal{N}(1.5, 0.3)$
Velocity bias (peculiar motions)		
b_{cen}	$0.116^{+0.070}_{-0.069} \mathcal{N}(0.1, 0.3)$	$0.134^{+0.028}_{-0.021} \mathcal{N}(0.1, 0.3)$
b_{r}	$0.873^{+0.093}_{-0.082} \mathcal{N}(0.7, 1.2)$	$0.959^{+0.095}_{-0.130} \mathcal{N}(0.9, 0.4)$
b_{t}	$0.802^{+0.146}_{-0.106} \mathcal{N}(0.7, 1.3)$	$1.183^{+0.098}_{-0.107} \mathcal{N}(0.8, 1.4)$
f_{σ}	$0.128^{+0.050}_{-0.057} \mathcal{N}(0.2, 0.2)$	$0.053^{+0.075}_{-0.059} \mathcal{N}(0.5, 0.2)$
Halo exclusion		
$\log(M_{\text{excl}}/h^{-1}\text{M}_{\odot})$	$13.452^{+0.129}_{-0.125} \mathcal{N}(13.5, 0.3)$	$13.417^{+0.128}_{-0.126} \mathcal{N}(14.0, 0.3)$
$r_{\text{excl}} (h^{-1}\text{Mpc})$	$2.306^{+0.489}_{-0.323} \mathcal{N}(2.2, 1.0)$	$3.226^{+0.268}_{-0.259} \mathcal{N}(4.5, 0.5)$
p_{excl}	$0.631^{+0.088}_{-0.123} \mathcal{N}(0.6, 0.3)$	$0.480^{+0.081}_{-0.067} \mathcal{N}(0.3, 0.3)$
AM (galaxy–halo connection)		
σ_{AM}	$0.294^{+0.065}_{-0.053} \mathcal{N}(0.3, 0.2)$	$0.301^{+0.056}_{-0.070} \mathcal{N}(0.3, 0.2)$
$V (s^{-1}\text{km})$	$185.903^{+82.474}_{-10.786} \mathcal{N}(190, 100)$	$347.927^{+27.715}_{-4.294} \mathcal{N}(370, 100)$
$\sigma_V (s^{-1}\text{km})$	$88.135^{+29.430}_{-12.407} \mathcal{N}(100, 90)$	$134.890^{+20.4284}_{-8.835} \mathcal{N}(170, 60)$
$f_{\text{sat}} (\%) \text{ total}$	$6.921^{+0.370}_{-0.452} \mathcal{N}(7.8, 1.5)$	$9.311^{+0.629}_{-0.557} \mathcal{N}(10.4, 1.5)$
Quenching (via joint occupation)		
α	$0.501^{+0.065}_{-0.057} \mathcal{N}(0.4, 0.2)$	—
$R_0 (h^{-1}\text{Mpc})$	$4.498^{+0.255}_{-0.237} \mathcal{N}(5.0, 2.0)$	—
δ	$2.987^{+0.325}_{-0.308} \mathcal{N}(3.0, 1.5)$	—
$\log(M_0/h^{-1}\text{M}_{\odot})$	$13.232^{+0.055}_{-0.060} \mathcal{N}(13.0, 0.4)$	—
m_{slope}	$0.997^{+0.075}_{-0.072} \mathcal{N}(1.0, 0.4)$	—
$\chi^2_{\text{joint}}/\text{dof}$	1.37	1.61
dof	119	(26 data points \times 3 observables \times 2 tracers \rightarrow 156 data points – 37 parameters)
Realized values (pure predictions)		
$f_{\text{sat}} (\%) \text{ total}$	9.50	14.09
$f_{\text{sat}} (\%) \text{ max conformal}$	1.09	3.52
$f_{\text{sat}} (\%) \text{ min conformal}$	7.02	0.005
$f_{\text{orph}} (\%) \text{ total}$	0.58	10.57
Minimal selection cuts		
$V_{\text{peak}}^{\text{min}} (s^{-1}\text{km})$	110	370

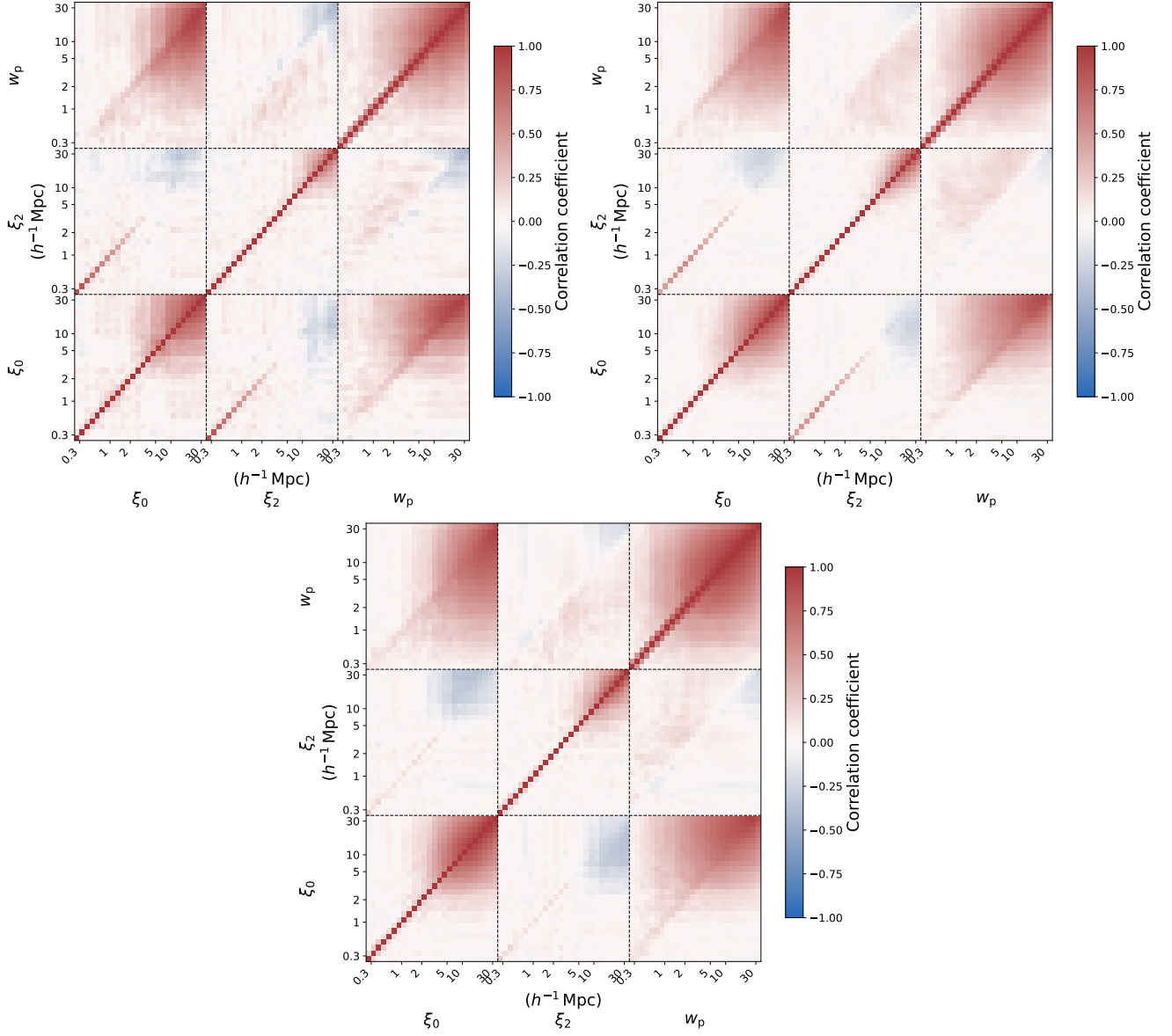


Figure 9. Normalised covariance matrices of the ELG1 (top left), LRG3 (top right), and ELG1 \times LRG3 (bottom) HOME high-fidelity mocks computed from 1800 $500 h^{-1}$ Mpc ABACUSUMMIT boxes.

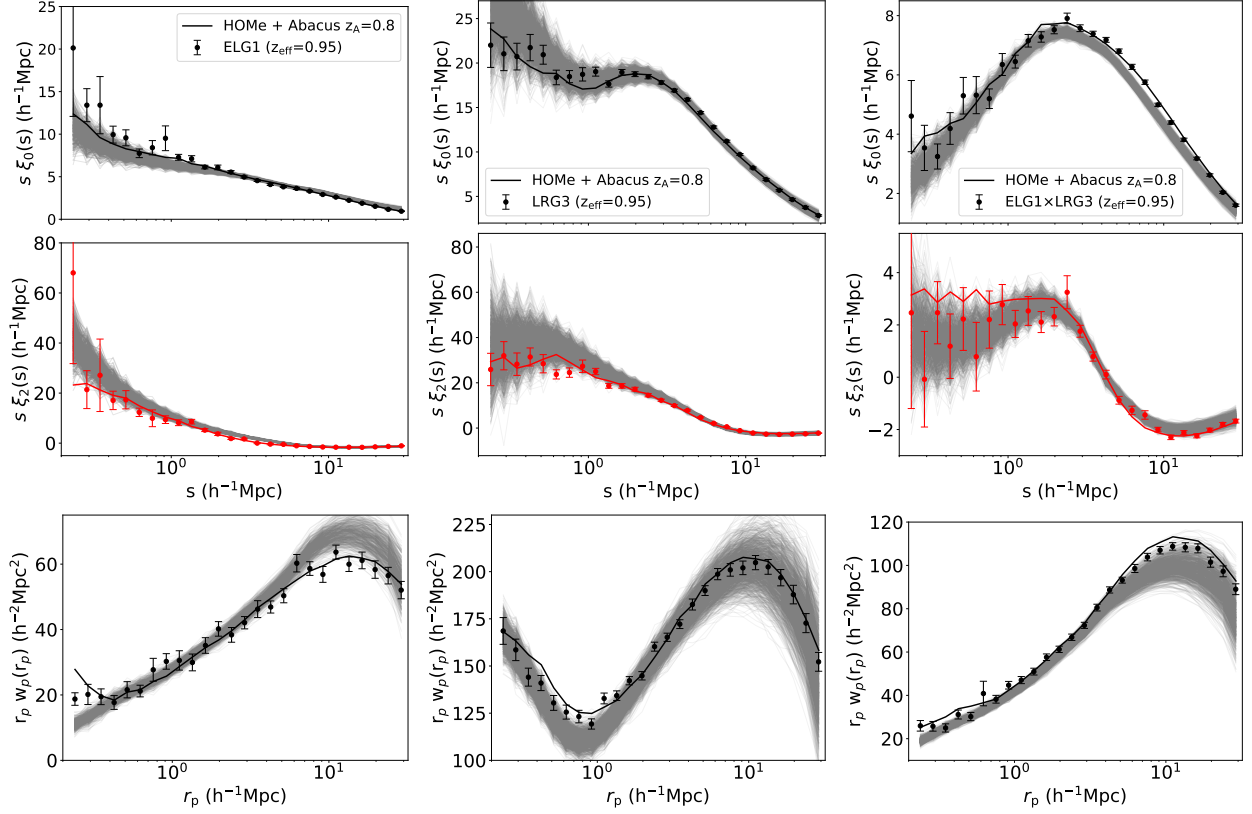


Figure 10. ELG1 (left column), LRG3 (middle), and ELG1×LRG3 (right) correlation functions (markers) with the HOME high-fidelity mocks (thick solid lines), compared with the 1800 2PCFs (grey thin lines) from the $500 h^{-1}\text{Mpc}$ ABACUSSUMMIT boxes used to compute the correlation matrix in Figure 9. Note that all the 1800 2PCFs for the 3 tracers are obtained by imposing the HOME best-fit configuration obtained from the $2 h^{-1}\text{Gpc}$ boxes (see Table 4) to the small boxes, with minor adjustments only for ELG1. Here, the discrepancies observed are mainly due to the limited volume of the small boxes, which enhances sample variance and suppresses the contribution of massive halos and long-wavelength modes.

hosts, such that ELGs are progressively disfavored in high-density, LRG-dominated environments.

Our best-fit parameters in Table 4 indicate a strongly local and mass-dependent effect: massive LRG halos within a few Mpc exert the strongest suppression, while more distant or lower-mass systems contribute negligibly. This interaction naturally reduces the ELG occupation around LRG hosts and thereby controls the 1-halo contribution to the ELG1×LRG3 cross-correlation, yielding the level of conformity required by the data without invoking explicit baryonic physics. The resulting modulation of ELG centrals is mild on large scales but crucial for matching the small-scale anisotropic signal.

In conclusion, the non-trivial interplay among satellite fraction, velocity biases, halo exclusion and environmental quenching (via joint occupation) underpins the sensitivity and accuracy of our forward modeling approach. The individual impact of each model parameter on the clustering is shown and discussed in Appendix C.

6.2.2. HOME posterior distribution

Figures 11–15 present the posterior distributions, obtained from level-II inference, of the physical parameters of our model (37 in total) for DESI ELGs (blue contours and black straight lines) and LRGs (red contours and grey lines). The high dimensionality of the parameter space prevents us from representing them in unique corner plots; we split them in different panels, grouped by the physical prescription (see the captions for details).

Overall, the posterior distributions are compact and close to Gaussian for both tracers, demonstrating that the DESI two-point clustering measurements provide strong constraining power on the main ingredients of our forward model. The lack of strong non-Gaussian features or extended degeneracy tails suggests that the model parameters are well determined by the combination of real- and redshift-space clustering, and that residual parameter correlations are moderate.

We adopt the maximum likelihood estimate (MLE) as our best-fit model, which simultaneously reproduces the ELG1 auto-, LRG3 auto-, and ELG1×LRG3 cross-

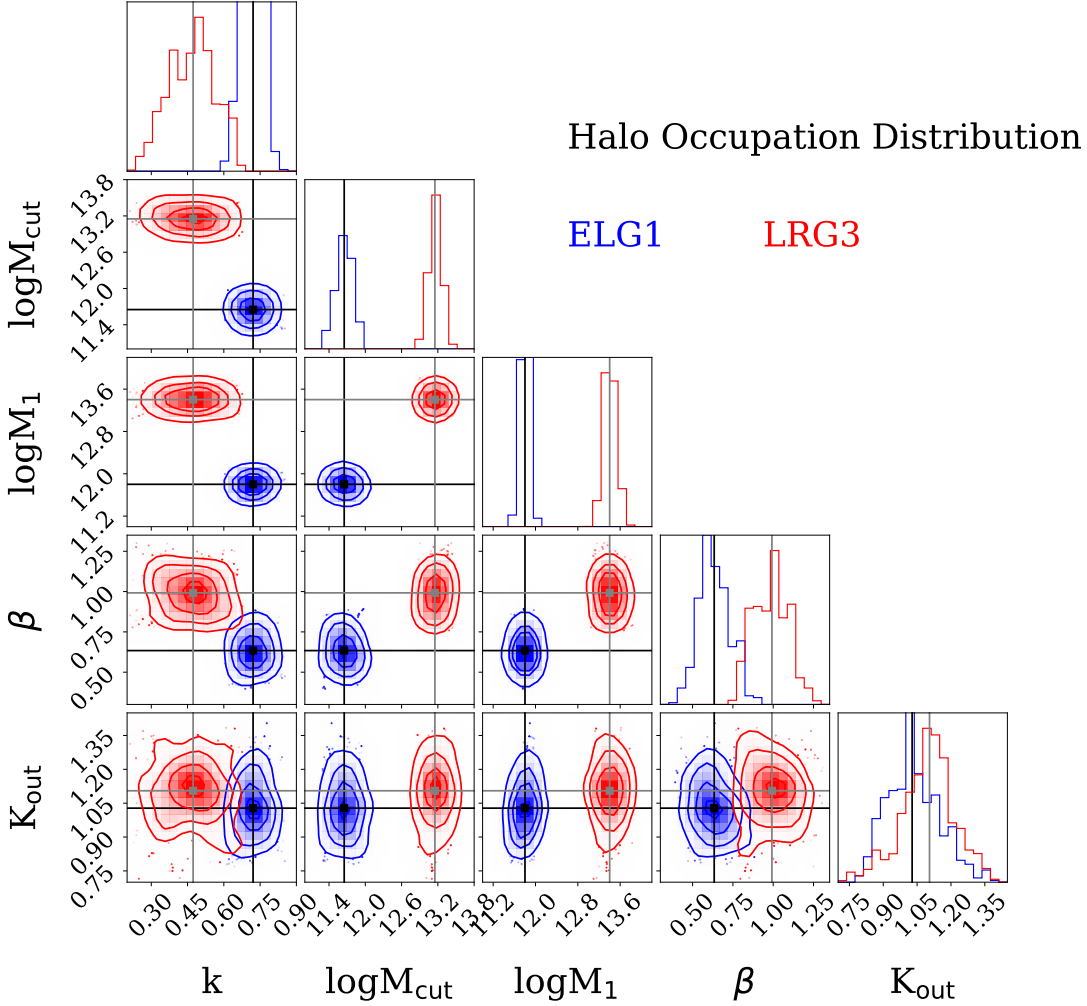


Figure 11. Posterior distribution of the HOD model parameters for the **ELG1** (blue contours and black straight lines) and **LRG3** (red contours and grey lines) samples showing the HOD parameters. The best-fit parameter values are written above each panel as well as in Table 4, and they are highlighted by the intersection of the straight lines; the resulting models are shown in Figure 6.

correlation functions. The best-fit parameter values are highlighted by the intersection of the straight lines and we report them in Table 4.

We sample HOME full posterior, for each latent realization $\{\theta_i\}_{i=1}^N$ in Eq. 31, using emcee with 37 dimensions coupled with 80 walkers and 1500 steps per walker. We set the number of walkers more than 2.5 times that of the parameters, and choose the number of steps per walker based on the maximum autocorrelation time (τ), so that $n_{\text{steps}} > 50 \tau_{\text{max}}$, which guarantees convergence (Foreman-Mackey et al. 2013).

To ensure reliable parameter inference, we apply a conservative burn-in procedure, but no thinning, to the MCMC chains. We determine the burn-in length from the integrated autocorrelation time, which we compute for each parameter using emcee with a relative tolerance of 0.01. We remove correlations with the initial

conditions by discarding the first $5 \tau_{\text{max}}$ steps of each walker. We estimate $\tau_{\text{max}} = 24.5$, a relatively small value that ensures good mixing. This implies that: (i) the walkers move broadly across the posterior, exploring all high-probability regions; (ii) the samples are weakly correlated, i.e. the chain does not remain close to the same value for many steps; (iii) the full posterior shape is properly recovered, including any modes, tails, or correlations between parameters.

After checking the autocorrelation functions of all parameters, we kept all post-burn-in samples without thinning as this is not required for unbiased posterior estimation and only reduces the effective sample size at fixed runtime, so we adopt $\text{thin} = 1$.

The posterior distributions of the HOD parameters in Figure 11 reveal that ELGs and LRGs occupy distinct regions of the parameter space, reflecting their different

astrophysical natures. ELGs favor lower halo masses, with tight constraints around lower values of both $\log M_{\text{cut}}$ and $\log M_1$, consistent with their association to younger, late-forming halos with shallow potential wells. This picture is fully consistent with the ELG (LRG) HOD inferred from DESI One-Percent data by [Rocher et al. \(2023\)](#) ([Yuan et al. \(2024\)](#)), who found that ELGs (LRGs) populate halos of $M_{\text{vir}} \sim 5 \times 10^{11} - 10^{12} h^{-1} M_{\odot}$ ($M_{\text{vir}} \sim 10^{13} h^{-1} M_{\odot}$), with a modest (non-negligible) satellite fraction and a shallow (steep) high-mass tail.

Their occupation slope β is similarly lower, indicating a more gradual rise of the satellite population with halo mass. In contrast, the LRG posteriors peak at significantly larger $\log M_{\text{cut}}$ and $\log M_1$, characteristic of older, more massive and biased environments hosting quenched, early-type systems. Despite this large mass separation, both tracers exhibit well-constrained k parameters—governing the satellite number normalization—with LRGs favoring a steeper increase in satellite abundance at high masses, as expected for quenched massive halos.

Finally, the constraints on K_{out} reinforce the complementary environmental behavior of these samples—ELGs favoring a placement slightly below the DM particle positions (cooler, more diffuse outskirts), while LRGs require satellites to be distributed somewhat beyond the average DM profile (mild over-concentration compensation). Together, these constraints demonstrate that the HOD ingredients in HOME are not only tightly determined by the observations, but also align with the established understanding of ELG and LRG formation and environment.

The posterior distributions of the velocity-bias parameters presented in Figure 12 show that anisotropic clustering places tight constraints on satellite kinematics, directly informing how galaxy peculiar velocities deviate from those of their host dark matter halos.

For ELGs, we find $b_r, b_t < 1$ and $f_{\sigma} \ll 1$, corresponding to dynamically cool satellites that retain coherent infall motions and have not yet been isotropized. This interpretation is fully consistent with the observational modeling of DESI ELGs by [Rocher et al. \(2023\)](#), who likewise require sub-virial satellite motions to suppress excessive small-scale clustering power in ELG samples. Our forward model strengthens this picture by showing that such subdued kinematics arise naturally once ELGs occupy lower-mass, still-assembling halos where environmental quenching has only recently begun.

For LRGs we recover $b_r < 1$ and $b_t > 1$, implying suppressed radial but slightly enhanced tangential motions—the hallmark of a population that has experienced substantial orbital decay and tidal processing

in massive halos. Dynamical friction efficiently removes satellites on plunging orbits, leaving survivors on more circular paths that broaden the transverse velocity field but reduce coherent infall signatures.

These results align well with high-resolution hydrodynamical expectations ([Anbajagane et al. 2022](#)), and with DESI HOD constraints for LRGs from [Yuan et al. \(2024\)](#), who similarly find sub-virial radial motions with mild tangential heating at $z \sim 1$. The agreement confirms that LRG satellites are dynamically cooler than the dark matter but retain orbital anisotropy driven by their accretion histories.

Finally, the extremely small central velocity biases ($b_{\text{cen}} \ll 1$) ensure centrals remain nearly comoving with their halo bulk, correctly avoiding artificial FoG broadening in the 1-halo regime.

The HOME exclusion posteriors presented in Figure 13 show that both tracers require a probabilistic halo-halo exclusion operating at group/cluster scales, i.e. $\log(M_{\text{excl}}/(h^{-1} M_{\odot})) \sim 13.2-13.4$ and $r_{\text{excl}} \sim 3-4 h^{-1}$, precisely where the 1-halo to 2-halo transition is observed in the anisotropic clustering. LRGs favor a slightly higher exclusion mass and smaller exclusion radius than ELGs, consistent with their more massive and concentrated host halos, while the transition steepness (p_{excl}) is similar for both samples. These values are fully consistent with earlier HOD treatments of halo exclusion for massive galaxies and extend that picture to the ELG population within a single, jointly-fit framework.

The posterior distributions of the abundance-matching parameters shown in Figure 14 reveal clear and physically meaningful differences between ELGs and LRGs. The stellar-to-halo connection for LRGs favors higher values of the characteristic peak circular velocity scale (V) and its dispersion (σ_V), consistent with these galaxies occupying deeper potential wells and tracing more massive halos. ELGs instead prefer lower values, as expected for systems residing in younger, less massive hosts where recent accretion and star formation remain more prevalent. The tight, nearly Gaussian constraints on the AM scatter parameter (σ_{AM}) for both tracers imply strong sensitivity of the clustering data to how galaxies populate the halo velocity function—i.e., the rank-order mapping between V_{peak} and galaxy stellar mass must remain sharp to reproduce the observed two-point statistics.

Finally, the satellite fraction parameter (f_{sat})—note that this input parameter differs from the *realized* satellite fraction emerging, as a pure prediction, from our forward model (see Table 4)—is well constrained and naturally separates the two samples: ELGs exhibit a much smaller intrinsic satellite abundance than LRGs,

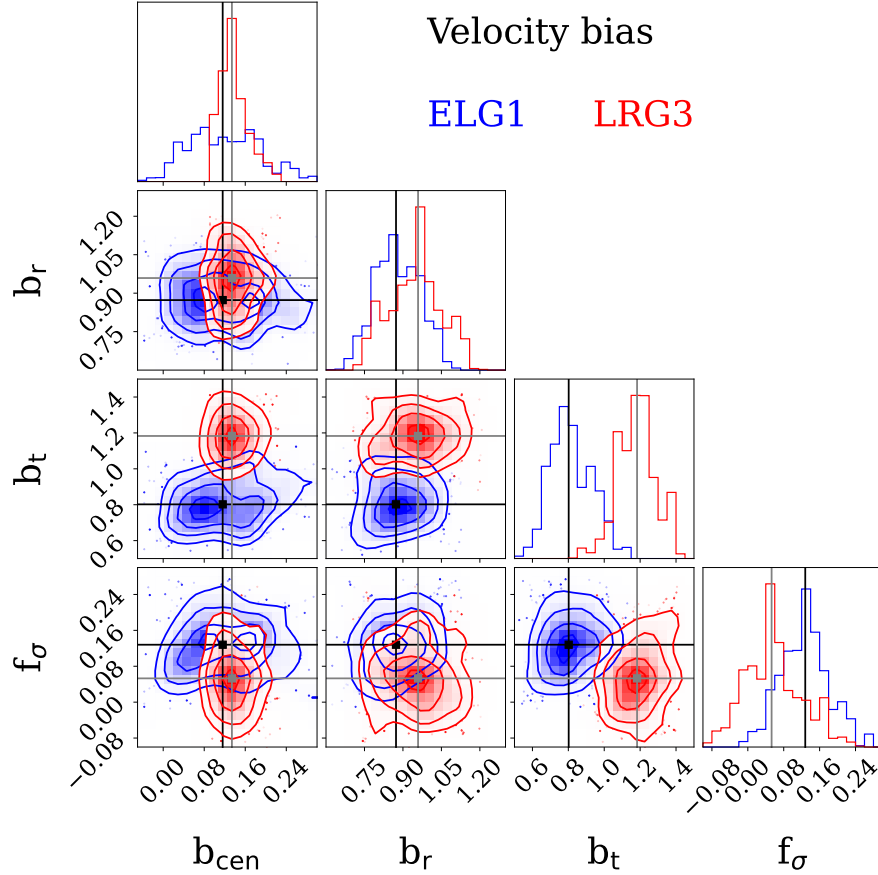


Figure 12. Posterior distribution of the ELG and LRG velocity-bias parameters.

reflecting the role of environment-driven quenching that disfavors ELG satellites in massive halos.

Taken together, these posteriors show that the galaxy–halo connection inferred by HOME for both tracers is highly informative, internally consistent, and closely aligned with the current picture of ELG and LRG formation and evolution.

The ELG×LRG joint-occupation posterior in Figure 15 confirm that the ELG×LRG cross-correlation functions place strong constraints on satellite quenching physics. The model infers:

- A characteristic quenching mass of $\log M_0 \sim 13.2$, corresponding to LRG-host halos where ELG satellites are strongly suppressed;
- A steep transition with $\delta \sim 3$, indicating rapid quenching after infall into massive halos;
- A radial scale $R_0 \sim 4 - 5 h^{-1} \text{Mpc}$, showing that environmental effects extend beyond the virial radius—consistent with backplash and pre-processing;

- A normalization $\alpha \sim 0.5$, meaning that only about half of the potential ELG satellites survive in these massive environments.
- A steep mass dependence with $m_{\text{slope}} \sim 1$, implying that the quenching efficiency rises rapidly with halo mass: slightly above M_0 , ELG satellites are only moderately suppressed, but deep in the group/cluster regime they are almost fully removed from the ELG population.

Together, these parameters describe a picture where environmental quenching is strongly mass- and radius-dependent: ELG satellites are preferentially removed in and around massive LRG halos, with efficiency that increases both with host mass and proximity to the halo center. This is fully consistent with semi-analytic results, such as Orsi & Angulo (2018) or Gonzalez-Perez et al. (2018), which likewise predict that ELG-like galaxies avoid the most massive, quenched environments.

The tightness of the posteriors indicates that the cross-correlation is especially informative, forcing the model to accurately partition satellites into quenched (LRG-like) and star-forming (ELG-like) environments. Because HOME discovers these quenching signatures

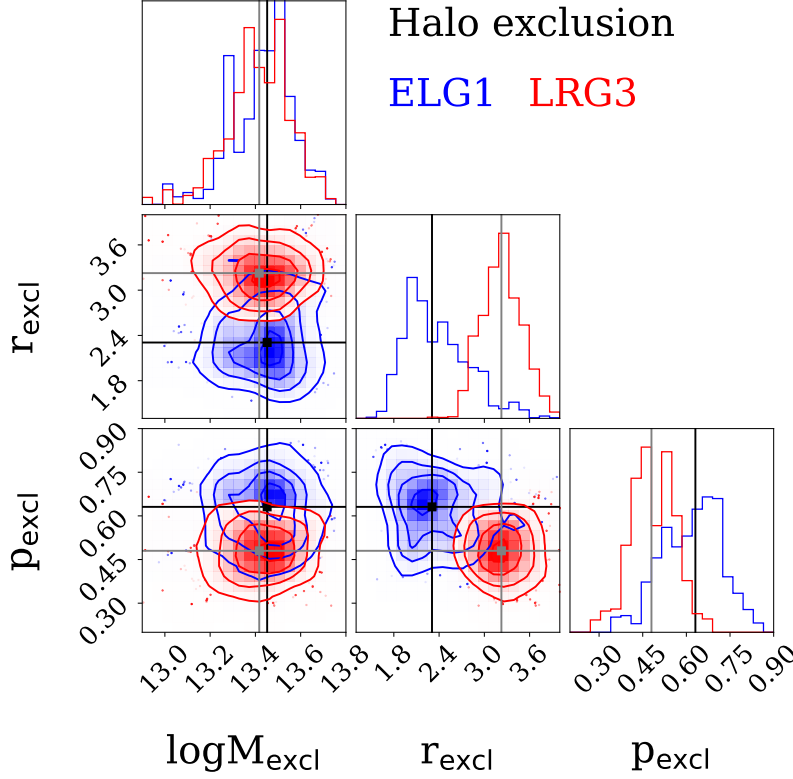


Figure 13. Posterior distribution of the ELG and LRG halo-exclusion parameters.

purely through forward-modeling of positions and velocities, the agreement with semi-analytic predictions provides strong validation of the approach.

6.2.3. Impact of peculiar motions on the anisotropic clustering

In our coherent-flow prescription in Eq. 15, the two velocity-bias parameters, b_r and b_t , scale the amplitude, not the direction, of the radial-infall and tangential-orbital components that satellites inherit from the DM particles bound to the same halo. A value of $b_r = 1$ ($b_t = 1$) means that satellites on average follow the same radial (tangential) velocity field as the underlying DM. Conversely, $b < 1$ corresponds to cooler kinematics (i.e., slower infall or more circular orbits), whereas $b > 1$ indicates hotter motions.

In this framework, it is important to distinguish between the model definition of satellite motions and their observational imprint. By construction, satellites remain part of coherent flows tied to their host halos: their velocities are rescaled versions of the underlying DM radial and tangential components, preserving the dynamical coupling to the halo potential. However, when projected into redshift space, these flows do not align with the large-scale streaming motions of halos and instead appear observationally as incoherent, virial-like dispersions that drive the FoG effect. In practice, the ve-

locity-bias parameters control the relative weight of the coherent components, while the additional random term f_σ captures residual scatter. This dual description allows HOME to remain physically grounded in the halo velocity field while still reproducing the apparent incoherent small-scale anisotropy in galaxy clustering.

For ELG1, the model predicts $b_r \sim 0.873$ and $b_t \sim 0.802$, indicating sub-virial velocity dispersions in both the radial and tangential components, with only mild orbital anisotropy. In contrast to previous ELG HOD studies (e.g. Rocher et al. 2023), which typically infer $b_r, b_t \gtrsim 1$, suggesting satellites dynamically hotter than the dark matter, HOME does not require such tangential heating. Instead, ELG satellites appear kinematically cooler than the host halo particles and only gently biased toward radial motions.

This behavior is physically consistent with the idea that ELGs are, on average, recently accreted satellites, which have not yet undergone strong dynamical processing (e.g., tidal stirring, harassment) nor fully experienced environmental quenching in massive halos. Their phase-space properties therefore reflect a population still transitioning from infall to virialization.

For LRG3, we infer $b_r \sim 0.959$ and $b_t \sim 1.180$, indicating mildly suppressed radial motions but tangential dispersions modestly hotter than those of the dark mat-

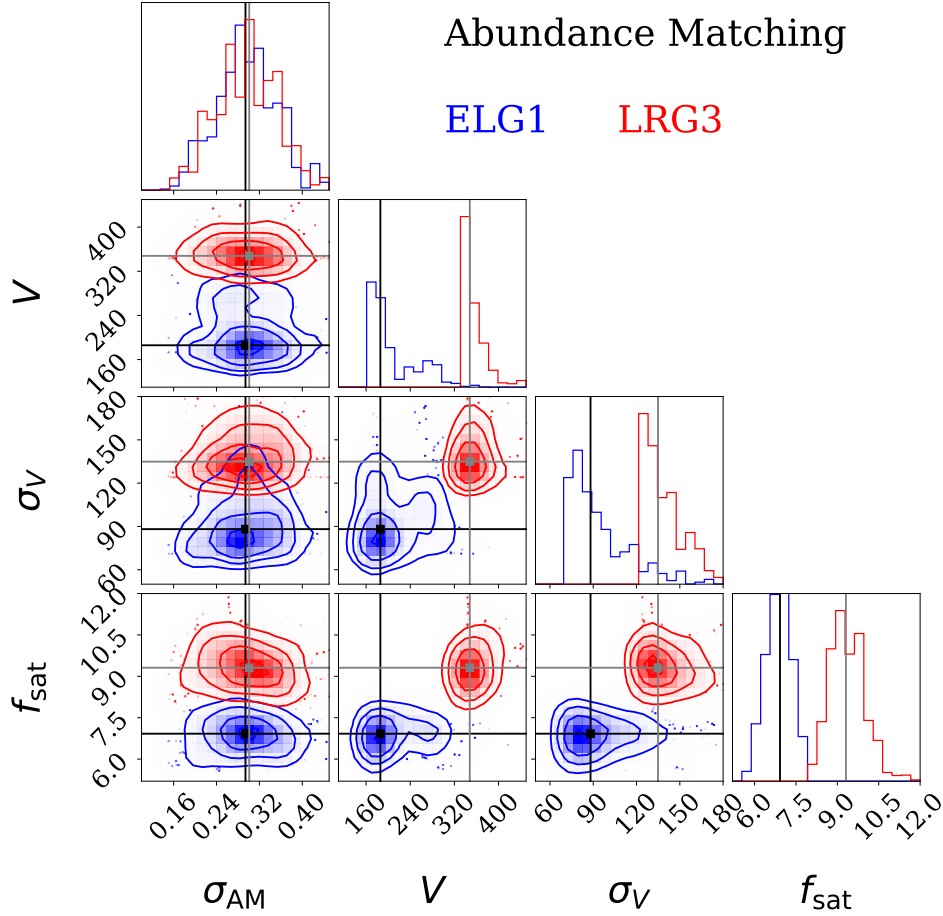


Figure 14. Posterior distribution of the ELG and LRG AM parameters.

ter. This anisotropy suggests that LRG satellites have undergone significant dynamical evolution: efficient orbital decay and tidal stripping reduce their radial kinetic energy, while the preferential removal of satellites on plunging orbits leaves the surviving population on more circular, tangentially supported trajectories. Such sub-virial radial motions combined with mild tangential heating are a natural outcome of long-term dynamical friction and environmental processing within massive halos.

Importantly, while the b_r and b_t values we find still describe satellites as part of coherent flows around their hosts, the balance of those flows is shifted: radial infall is suppressed ($b_r < 1$) and tangential dispersion is enhanced ($b_t > 1$). This freedom is essential to reproduce the observed anisotropy level in the small-scale clustering. In other words, satellites in both the ELG1 and LRG3 samples remain dynamically coupled to their hosts, but with different anisotropic weights in the radial versus tangential components, such that the flows no longer resemble simple radial infall but instead reflect hotter, tangentially biased orbits.

These findings align with predictions from state-of-the-art hydrodynamical simulations, such as IllustrisTNG, which show that satellite velocity bias is typically suppressed below unity for massive galaxies, with only weak dependence on host halo mass and satellite properties (Anbajagane et al. 2022). They are also consistent with recent DESI HOD constraints for LRGs (Yuan et al. 2024), which similarly indicate sub-virial satellite motions across the relevant redshift range. Together, these comparisons support a dynamical picture in which LRG satellites are cooler than the surrounding dark matter, consistent with long-term orbital decay and stripping within massive hosts.

Earlier semi-analytic results (Orsi & Angulo 2018) predicted b_r and b_t values closer to or above unity for LRG-like tracers, implying kinematically hotter satellites. The slight departure from those findings likely reflects differences in the physical treatments of environmental quenching and tidal processing, and emphasizes that DESI clustering adds new constraining power on satellite dynamics.

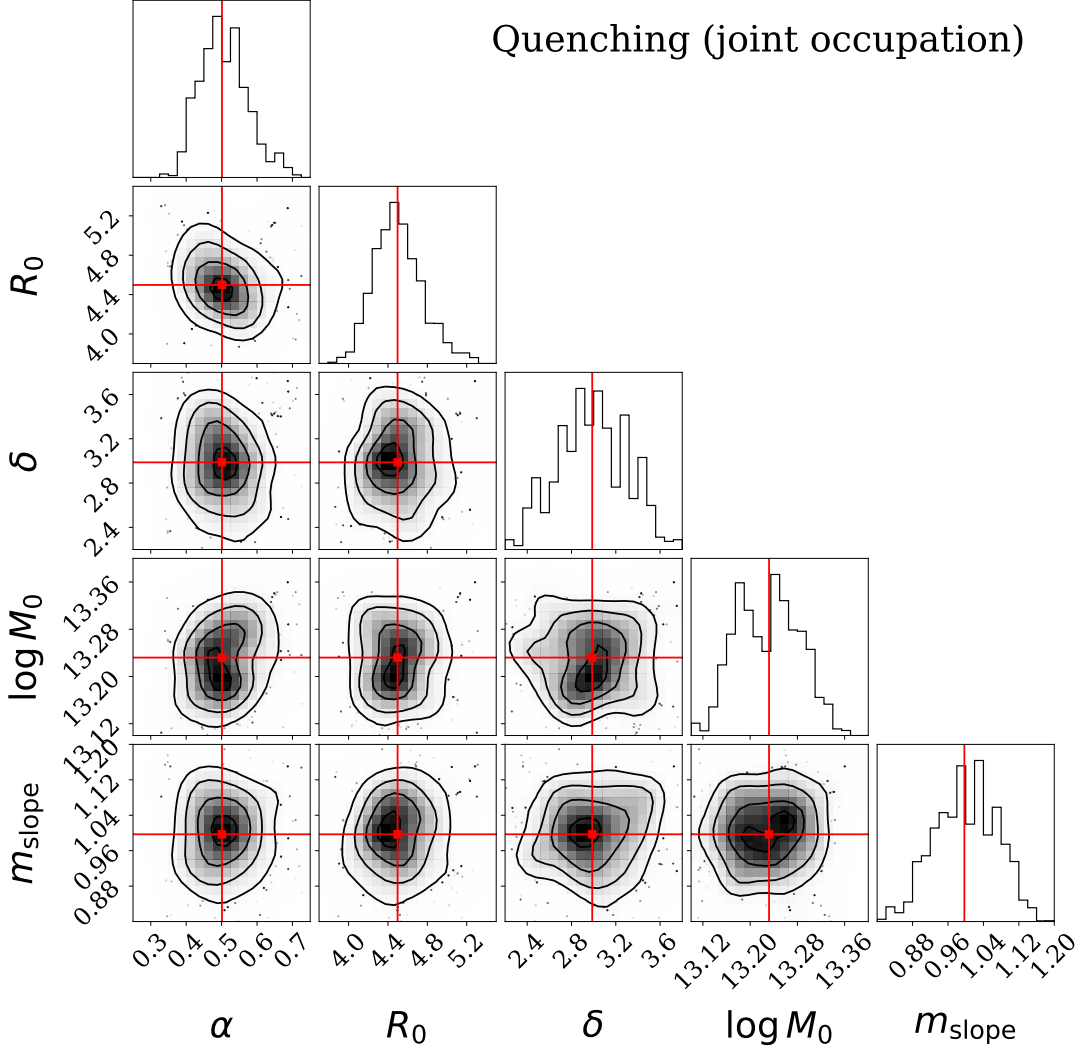


Figure 15. Posterior distribution of the model parameters driving the joint-occupation condition that statistically emulates the effects of environmental quenching of satellite ELG in massive LRG hosts.

As highlighted in § 6.2.1, the satellite fraction parameters compete with the physics of peculiar motions driven by the velocity-bias parameters: increasing (decreasing) b_r or b_t amplifies (suppresses) the clustering amplitude below $10 h^{-1} \text{Mpc}$, making velocity anisotropy a key lever for matching DESI redshift-space observables.

For the central velocity bias, we obtain $b_{\text{cen}} \sim 0.116$ and $b_{\text{cen}} \sim 0.130$ for ELG1 and LRG3, respectively. In our implementation (Eq. 1), centrals sit at the halo center and follow the bulk peculiar velocity of their host. The parameter b_{cen} controls an additional residual motion relative to the halo center-of-mass, modeled as a fraction of the local dark matter velocity dispersion.

These very small b_{cen} values indicate that centrals are nearly at rest with respect to their host halo, as expected if they closely trace the minimum of the gravitational potential. While this residual motion has negli-

ble impact on large scales, even a small non-zero b_{cen} can slightly broaden the line-of-sight distribution of pairs involving centrals. This leads to a mild suppression of the quadrupole on small, FoG-dominated scales—acting together with the satellite velocity anisotropy to match the observed redshift-space distortions.

In Eq. 15, the parameter f_σ sets the amplitude of an additional stochastic LOS velocity component, expressed in units of the DM 1D velocity dispersion. This term is meant to capture small-scale, uncorrelated motions not described by the coherent radial and tangential components controlled by b_r and b_t . We find $f_\sigma \sim 0.128$ for ELG1 (i.e., $\sim 13\%$ of the DM 1D dispersion), and 0.050 for LRG3 ($\sim 5\%$). These values introduce a modest additional random LOS velocity contribution, which enhances FoG damping on small scales. As expected, the effect of f_σ is partially degenerate with b_r and b_t ,

since all three parameters enter the total LOS velocity dispersion of satellites and therefore jointly shape the small-scale redshift-space anisotropy.

These results demonstrate that a realistic treatment of satellite peculiar motions is essential to reproducing the observed redshift-space anisotropy, and they highlight how peculiar velocities can serve as a sensitive probe of satellite dynamics in future cosmological analyses.

6.2.4. HOME HOD and conformity predictions

The HOME-inferred halo occupation distribution of the DESI Y1 ELG1 and LRG3 tracers is schematically illustrated in Figure 16 and highlights both the predictive power and internal consistency of our model.

Its behavior is a direct consequence of the probabilistic class assignment based on the mixture model (§ 3.3.3), where galaxy types are not predetermined, but stochastically sampled from a Gaussian multi-tracer PDF formulated as a function of V_{peak} . This PDF is weighted and normalized using the input satellite fractions (Table 4) and the observed number densities of ELGs and LRGs (Eq. 21) to determine the relative contribution of each tracer to the clustering. This process yields a high-fidelity mock galaxy catalog simultaneously reproducing the auto- and cross-correlation functions of ELGs and LRGs with unprecedented accuracy.

Figure 16 shows that, for both tracers, the dominant configuration predicted by our model is that of central halos hosting no satellites—90.50% for ELGs and 85.91% for LRGs—while the remaining 9.50% (ELGs) and 14.09% (LRGs) are satellites. Among these, only 1.09% (3.52%) of ELG (LRG) satellites reside in halos whose central galaxy is of the same tracer type, i.e. the maximally conformal configuration. On the other hand, a substantial fraction of ELGs (7.02%) and a negligible fraction of LRGs (0.005%, consistent with observations) inhabit hosts with a central galaxy of the complementary type, leading to minimally conformal configurations. The remainder—0.58% of ELGs and 10.57% of LRG—are orphan satellites, i.e. satellites whose parent halos do not appear as centrals in the final realization.

From these numbers, we deduce that *satellite ELG strongly prefer minimally conformal configurations, while satellite LRG are mostly maximally conformity and orphan field galaxies.*

A sizable orphan contribution is expected in HOME because satellites are drawn from the full reservoir of DM particles surviving abundance-matching selection. Since LRGs are assigned first, without any conditional dependence on ELGs, it is encouraging that the model still produces a non-negligible fraction of maximally conformal LRG satellites. For ELGs, the

joint-occupation (environmental quenching) condition strongly restricts their ability to remain satellites inside massive, LRG-dominated halos. This not only matches physical expectations from gas-depletion processes but also naturally reduces the orphan fraction while enhancing the cross-occupancy signal.

Therefore, it is crucial to highlight that *the relative proportions of satellites in maximally/minimally conformal environments—and the orphan content of each tracer—are not imposed inputs but direct forward-model predictions that emerge self-consistently from the interplay of abundance matching, halo exclusion, and environmental quenching.* These predictions can be validated with hydrodynamical simulations and forthcoming data, enabling direct tests of environmental quenching pathways.

In particular, the ELG×LRG joint-occupation condition captures, in a statistical way, the environmental quenching experienced by ELG satellites as they enter the deep potential wells of massive LRG hosts—an event that our model predicts to happen in most of the ELG satellites (7.02% out of 9.50%). The same prescription also suppresses the occurrence of LRG satellites in ELG halos, making such configurations extremely rare (0.005%), in line with current observational evidence.

Taken together, the physical ingredients of our model—i.e., satellite fractions, stochastic class assignment, halo exclusion, joint-occupation condition—reinforce the physical realism of HOME, demonstrating that the quenching of ELG satellites in massive LRG environments and the lack of LRG satellites orbiting ELG hosts arise self-consistently from the forward model rather than being imposed by hand.

Figure 17 shows two slices of our high-fidelity HOME mock catalog, $5 h^{-1}\text{Mpc}$ thick along the z coordinate, where we identify all possible configurations of the DESI Y1 ELG1 and LRG3 tracers as schematically described in Figure 16.

The top panel in Figure 18 shows the HOME-inferred HOD of the ELG1 and LRG3 tracers as a function of the parent host halo mass. Here, the satellite contribution is the total one including the (B), (C), and (D) configurations in Figure 16. Even though the orphans have no central host in the resulting mock catalog, we are able to represent them here as we keep track of the parent halo mass of the DM particles in the simulation. In the bottom panel we separate the contributions of maximally conformal, minimally conformal, and orphan satellites.

The central occupations inferred for ELG1 and LRG3 are consistent with predictions from recent HOD (e.g., Gonzalez-Perez et al. 2018; Avila et al. 2020; Hadzhiyska et al. 2021b; Yuan et al. 2022; Rocher et al. 2023;

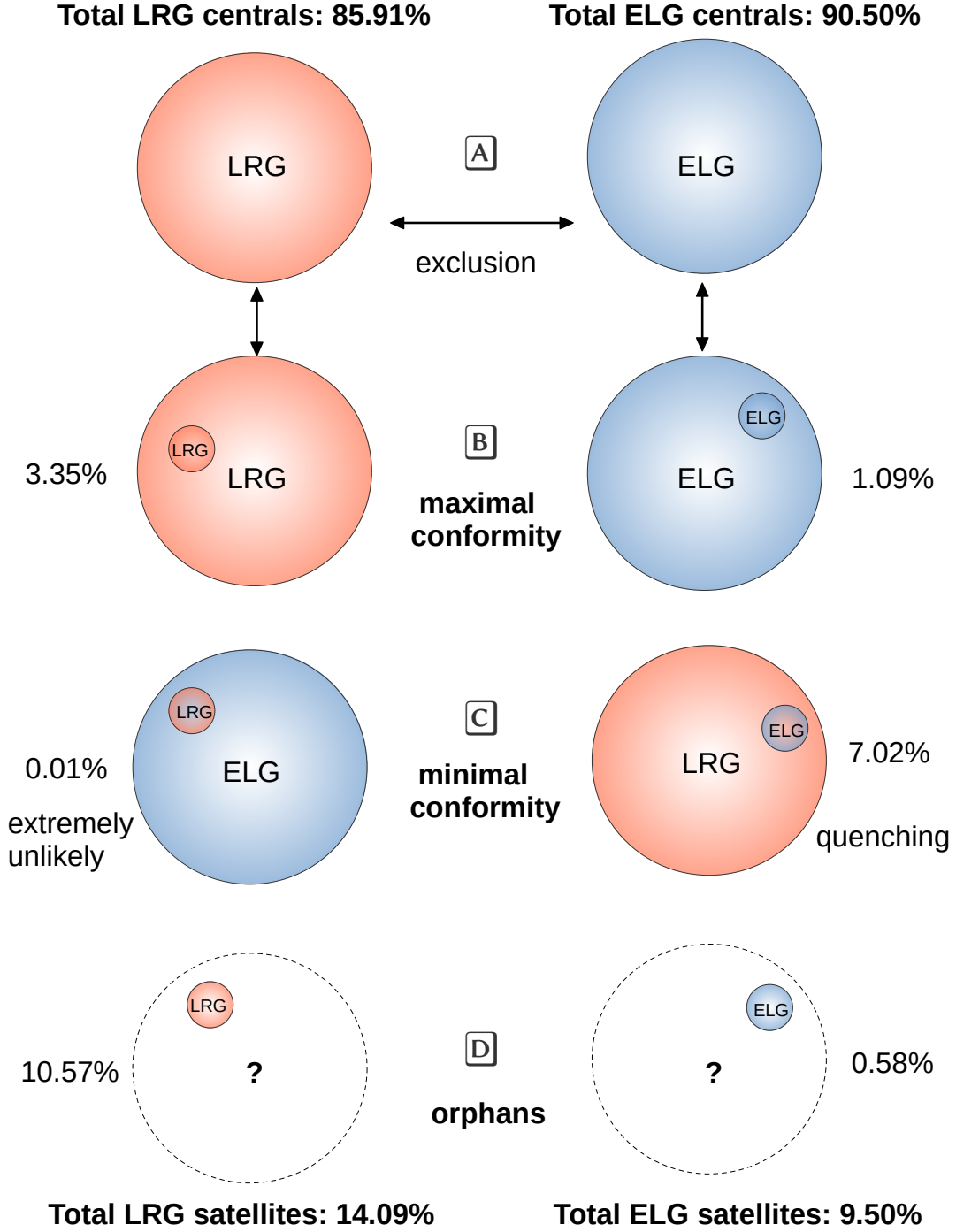


Figure 16. Cartoon illustration of the HOME -inferred halo occupation configuration for the DESI Y1 ELG1 and LRG3 tracers. Larger (smaller) solid circles denote central (satellite) halos, while orphan satellites—i.e. satellites with no corresponding central in the final mock catalog—are shown as satellites inside dashed circles. For each tracer we identify four characteristic configurations: (A) central galaxies residing in halos with no satellites; (B) central systems hosting one or more satellites of the same tracer species, corresponding to maximal conformity; (C) central systems hosting one or more satellites of the complementary tracer, representing minimal conformity; and (D) orphan satellites with no corresponding central host in the catalog. The percentages next to each configuration are our model predictions.

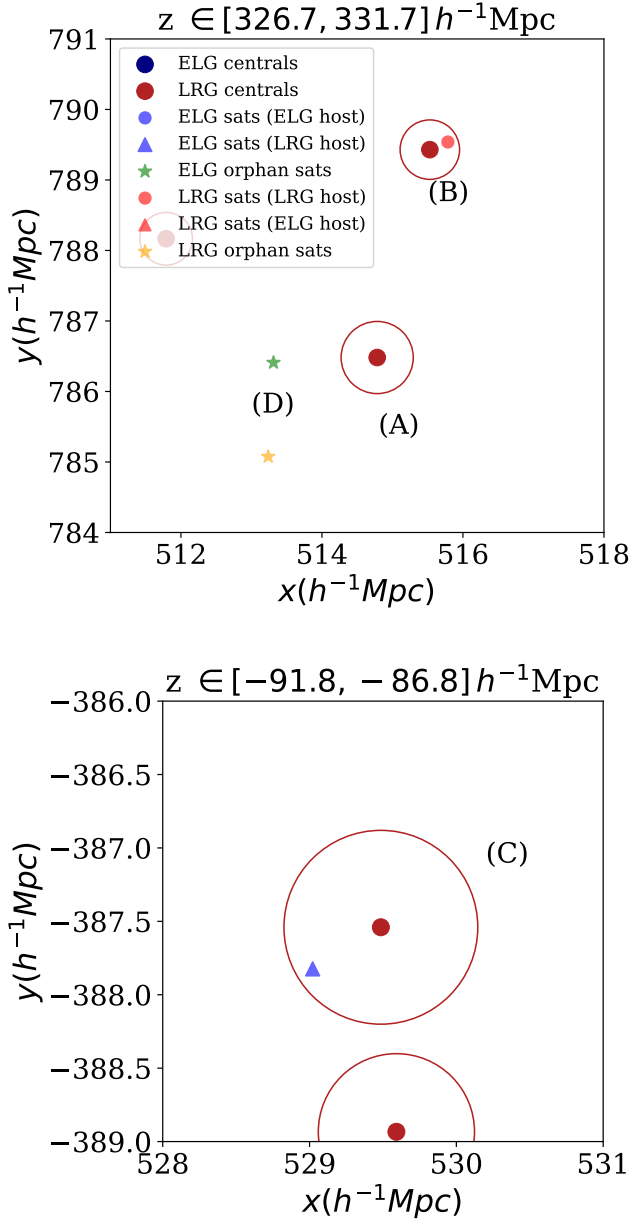


Figure 17. Slices— $5 h^{-1} \text{Mpc}$ thick in z —of our high-fidelity mock catalog for DESI Y1 ELGs and LRGs, showing the four configurations predicted by our forward model, which are schematically represented in Figure 16.

Yuan et al. 2024) and SHAM (e.g., Yu et al. 2022; Prada et al. 2025) studies. As shown in Figure 18, central ELGs (LRGs) predominantly occupy lower- (higher-) mass halos, with characteristic masses of $M_{\text{vir}} \sim 6.6 \times 10^{11} h^{-1} \text{M}_{\odot}$ for ELGs and $M_{\text{vir}} \sim 1.2 \times 10^{13} h^{-1} \text{M}_{\odot}$ for LRGs. Notably, the shape of the ELG central and satellite HODs exhibits an excellent match with previous HOD and SHAM analyses, in particular Gonzalez-Perez et al. (2018), including the location of the turnover and

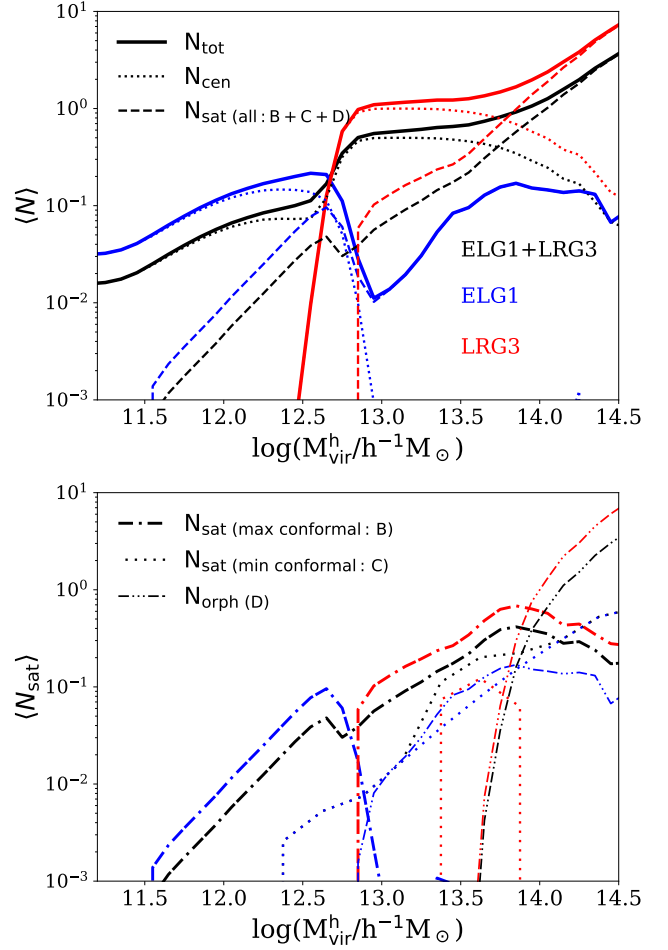


Figure 18. Home-inferred HOD as a function of the parent host halo virial mass. The contributions from ELG1 and LRG3 are respectively shown in blue and red; the global one is in black. The expected numbers of total, central, and satellite mocks are represented as solid, dotted and dashed lines, respectively. In the top panel the number of satellites is the total one, including the configurations (B), (C), (D) in Figure 16. In the bottom panel we separate the satellite contributions: maximally (minimally) conformal satellites are represented as dot-dashed (dotted) lines, and orphans as dot-dot-dot-dashed; these are the (B), (C), and (D) contributions which, once summed up, return the total satellite curves in the top panel. Note that we are able to isolate the contributions of orphans because we are showing the HOD as a function of the parent host mass, and for orphans we keep track of the parent halo mass of the DM particles in the simulation.

the high-mass suppression, reinforcing the physical robustness of our abundance-matching prescription.

For LRG3, the satellite component follows the steep, nearly power-law scaling with halo mass reported in earlier LRG clustering studies (e.g., Zheng et al. 2009; Reid & Spergel 2009; Yuan et al. 2024). Including orphan satellites preserves this canonical shape, whereas

Table 5. Percentages of DESI ELG and LRG tracers hosting 1, 2, and 3 satellites, as predicted by HOME.

N_{sat}	ELG1	LRG3
1	93.17	85.94
2	3.01	3.86
3	0.18	1.00

removing them slightly flattens the high-mass tail, although the overall mass scale and normalization remain consistent with published constraints.

At higher masses, the ELG occupations departs from a pure power law due to the combined effects of ELG satellite quenching in massive hosts—through mechanisms such as ram-pressure stripping, starvation, or tidal heating—and the halo-exclusion condition; for LRG the suppression comes from exclusion only.

This high-mass suppression is a signature of central-satellite conformity and is essential to reproducing the observed shape and amplitude of the ELG $w_p(r_p)$ upturn around $r_p \sim 10 h^{-1} \text{Mpc}$, which is sensitive to the interplay between ELG and LRG environments.

Orphan satellites contribute increasingly at high masses, becoming a large fraction of the already small satellite budget above $M_{\text{vir}}^h \gtrsim 10^{14} h^{-1} \text{M}_{\odot}$.

As reported in Table 5, HOME predicts that the large majority of central ELG1 and LRG3 host individual satellites (93.17% and 85.94%, respectively), few of them host 2 (3.01%; 3.86%), while more than 2 satellites are rare. These results are in line with previous SHAM studies at lower z showing that only 1.3% of ELG hosts have more than 1 satellite (Favole et al. 2016b).

Our satellite placement scheme combines host and particle positions through Eq. 11, with the parameter K_{out} rescaling the intrinsic dark-matter profile. We find that ELG1 and LRG3 favor $K_{\text{out}} \sim 1.028$ and 1.105, respectively. At first glance, this might seem counterintuitive—ELGs are typically associated with more extended, diffuse satellite distributions, whereas LRG satellites are expected to concentrate toward halo centers. However, this trend is fully consistent with the host-halo selection imposed via the minimal velocity thresholds $V_{\text{peak}}^{\text{min}}$ (Table 4).

The relatively low ELG1 threshold ($V_{\text{peak}}^{\text{min}} > 110 s^{-1} \text{km}$) selects late-forming halos with shallower gravitational potentials and intrinsically lower concentrations. Their satellite distributions are already ex-

tended; thus, K_{out} must be close to unity—and even slightly below—to avoid over-expanding satellites and inflating the small-scale clustering.

In contrast, the high threshold for LRG3 ($V_{\text{peak}}^{\text{min}} > 370 s^{-1} \text{km}$) preferentially selects earlier-forming, more concentrated environments. Here, $K_{\text{out}} > 1$ is needed to counteract this concentration bias and reproduce the observed flattening of LRG w_p at sub-Mpc scales.

Taken together, this highlights the role of K_{out} as a concentration-correction parameter: it compensates for assembly-bias effects introduced by the velocity-based halo selection while preserving realistic halo density profiles and maintaining agreement with observed one-halo clustering signatures.

7. SUMMARY AND CONCLUSIONS

We have introduced HOME, a physically motivated Halo Occupation Model designed to generate high-fidelity mock galaxy catalogs for any galaxy tracer observed by any survey, using any N -body cosmological simulation—including those lacking resolved satellite halos. The method is embedded in a two-level hierarchical Bayesian inference framework, optimized to tightly constrain the physical parameters of the model and deliver realistic mocks with unprecedented accuracy.

The excellent performance of the method has been demonstrated by analyzing DESI Y1 ELG, LRG, and ELG×LRG clustering measurements using the ABACUS-SUMMIT N -body cosmological simulation products.

HOME galaxy-halo connection scheme is a hybrid mixture of abundance matching and halo occupation distribution which overcomes the lack of substructures (not tracked by the halo finder in ABACUS-SUMMIT) by assigning satellites via DM particle positions. Our method provides reliable satellite peak circular velocities—based on analytic prescriptions informed by external high-resolution N -body simulations—to jointly model the ELG and LRG populations as complementary tracers of the same underlying dark-matter field. This enables, for the first time, a full reconstruction of their cross halo occupation distribution.

Our scheme fully accounts for the ELG and LRG intra-halo dynamics, halo exclusion, and ELG satellite quenching in LRG hosts. These are crucial ingredients to precisely model the anisotropic clustering on sub-Mpc scales, correctly shaping the 1-halo to 2-halo transition. Galaxy conformity naturally emerges as a byproduct of our forward model. Our main findings are:

1. HOME predicts the DESI Y1 ELG and LRG auto- and cross-correlation functions (multipoles and projected ones) down to $200 h^{-1} \text{kpc}$ with unprecedented accuracy, precisely modeling the intra-halo

dynamics and matching the observed anisotropy in the Universe. We find that satellite ELG dominate the anisotropic clustering below $4 h^{-1}\text{Mpc}$, acting as incoherent flows with a velocity bias relative to their hosts. The HOME-inferred HOD shows that: (i) 90.50% (85.91%) of ELG (LRG) are central galaxies with no satellites, typically residing in halos with masses of $M_{\text{vir}} \sim 6.6 \times 10^{11} (1.2 \times 10^{13}) h^{-1}\text{M}_{\odot}$; (ii) the ELG \times LRG cross-correlation is dominated by central–central pairs and shaped by halo exclusion on $2 - 5 h^{-1}\text{Mpc}$ scales; (iii) the remaining 9.50% (14.09%) of ELG (LRG) are satellites. Of these, 1.09% (3.52%) occupy a parent halo with a central galaxy of the same type (maximal conformity), 7.02% (0.005%) are minimally conformal living in a complementary host, and the remaining 0.58% (10.57%) are orphans.

2. From the above numbers, we conclude that the ELG \times LRG joint occupation not only reliably emulates the quenching of ELG satellites in LRG hosts, but also prevents LRG satellites to orbit ELG centrals, matching current observational constraints (e.g., Guo et al. 2021; Wetzel et al. 2013; Hirschmann et al. 2014; Rhee et al. 2024), in line with recent HOD (Alam et al. 2020; Yuan et al. 2024) and SAM (Orsi & Angulo 2018; Donnari et al. 2021) studies. As a result, ELG satellites tend to prefer a minimally conformal picture, before getting quenched, while LRG satellites are either maximally conformal or orphan field galaxies.
3. The best-fit HOME model casts 9.50% of ELGs as satellites. These dominate the anisotropic clustering signal below $4 h^{-1}\text{Mpc}$, acting as incoherent flows with a velocity bias relative to their hosts. The interplay between halo exclusion and quenching is essential to jointly reproduce the observed clustering of all tracers at all scales considered. Galactic conformity naturally emerges from HOME at the 1-halo level, and the picture we obtain is reminiscent of the conformity built within conditional HODs (e.g., Paranjape et al. 2015; Zu & Mandelbaum 2015, 2016), but arises here without explicit assumptions. By pushing our analysis down to $200 h^{-1}\text{kpc}$, we reach ~ 20 times higher resolution than previous studies (Yu et al. 2022), extracting cosmological information from two-point clustering alone while relying only on the dark matter distribution of the reference N -body simulation.
4. In the HOME configuration, satellite ELGs remain dynamically coupled to their host halos,

with velocity-bias parameters of $b_r \sim 0.873$ and $b_t \sim 0.802$. These values indicate dispersions modestly below those of the dark matter in both components, together with a mild radial preference ($b_r > b_t$). Thus, our model predicts that ELG satellites are kinematically cooler than the virial expectation but not isotropic: their orbits retain slightly stronger radial coherence than tangential support. This subtle anisotropy is sufficient to shape the anisotropic clustering signal below $4 h^{-1}\text{Mpc}$ —not by decoupling satellites from their hosts, but by imprinting a modest departure from isotropic satellite motions. In contrast, satellite LRGs occupy a different dynamical regime. We infer $b_r \sim 0.959$ and $b_t \sim 1.183$, implying that their radial motions are slightly sub-virial while their tangential dispersions are modestly enhanced relative to the dark matter. This anisotropic pattern—cooler radial infall but hotter, more circular orbits—is indicative of a dynamically evolved population in which long-term tidal stripping and dynamical friction have preferentially removed radially plunging satellites, leaving survivors on tangentially supported orbits in massive halos. Their higher satellite abundance ($f_{\text{sat}} \sim 14.09\%$) makes LRGs the dominant contributor to the 1-halo term. Moreover, the additional incoherent velocity term ($f_{\sigma} \sim 0.053$, i.e. $\sim 5\%$ of the DM 1-D dispersion) produces a mild broadening of the line-of-sight pairwise motions, contributing a small but non-negligible suppression of anisotropy on the smallest scales.

5. Interestingly, the sizeable orphan fraction we recover from HOME is almost entirely associated with LRGs, while ELG orphans remain negligible due to the quenching-driven joint-occupation mechanism. These LRG orphans appear as satellites without a corresponding central galaxy in the final realization, placing them in regions of the density field outside the virial extent of any identified host. Physically, such systems may correspond to backsplash galaxies, recently stripped satellites, or objects formerly bound to halos that have since been disrupted below the simulation’s resolution. Alternatively, they could reflect ejected systems that have interacted with massive environments and now linger in the diffuse outskirts of groups and filaments. Pinning down the nature of this population requires further investigation, which we plan to pursue in follow-up work using high-resolution hydrodynamical simulations,

such as IllustrisTNG¹⁵, where the baryonic component allows a more direct connection between galaxy quenching, stripping, and subhalo disruption. This will enable us to quantify the impact of baryonic feedback in our model. Understanding this population is key to refining halo–galaxy connection models and improving the realism of mock catalogs for future spectroscopic surveys.

The presence of this orphan component also motivates a thorough observational census of ELGs and LRGs using deep and wide-field galaxy surveys, such as DESI-II, Subaru PFS, or Rubin–LSST, to clarify their exact satellite fraction and its impact on the small-scale anisotropic clustering. This information, coupled with the remarkable constraining power of our method, will possibly allow us to discriminate among different cosmologies, including alternative gravity frameworks, such as $f(R)$. Our model performance will increase further by doing redshift tomography, which we plan to implement in follow-up studies.

Looking ahead, expanding our analysis to diverse N -body simulations with different cosmologies and incorporating additional physical constraints promises to significantly impact the calibration of the latent satellite properties and further refine the parameter space of the galaxy-halo connection framework.

ACKNOWLEDGEMENTS

GF acknowledges F. Sinigaglia, A. Rocher and S. Saito for insightful discussions during the development of this work. She also thanks A. Carnero, A. Ross, A. de Mattia and D. Chebat for helping with the DESI data model infrastructure.

During this project, GF has been supported by a *Juan de la Cierva Incorporación* grant n.IJC2020-044343-I. GF and FSK acknowledge the Spanish Ministry of Economy and Competitiveness (MINECO) for

financing the **Big Data of the Cosmic Web** project: PID2020-120612GB-I00/AEI/10.13039/ 501100011033 under which this work has been conceived and carried out, and the IAC for continuous support to the **Cosmology with LSS probes** project.

DJE’s contributions were supported by U.S. Department of Energy grant DE-SC0007881, by the National Science Foundation under Cooperative Agreement PHY-2019786 (the NSF AI Institute for Artificial Intelligence and Fundamental Interactions, <http://iaifi.org/>), and as a Simons Foundation Investigator.

SB is supported by the UKRI Future Leaders Fellowship [grant numbers MR/V023381/1 and UKRI2044].

Abacus development has been supported by NSF AST-1313285 and more recently by DOE-SC0013718, as well as by Simons Foundation funds and Harvard University startup funds. NM was supported as a NSF Graduate Research Fellow. The AbacusCosmos simulations were run on the El Gato supercomputer at the University of Arizona, supported by grant 1228509 from the NSF; the ABACUSUMMIT simulations have been supported by OLCF projects AST135 and AST145, the latter through the Department of Energy ALCC program. This research used resources of the Oak Ridge Leadership Computing Facility, which is a DOE Office of Science User Facility supported under Contract DE-AC05-00OR22725, and resources of the National Energy Research Scientific Computing Center (NERSC), a U.S. Department of Energy Office of Science User Facility located at Lawrence Berkeley National Laboratory, operated under Contract No. DE-AC02-05CH11231. We would like to thank the OLCF and NERSC support teams for their expert assistance throughout this project. We would also like to thank Stephen Bailey, Chia-Hsun Chuang, Shaun Cole, Pablo Fosalba, Salman Habib, Katrin Heitmann, Core Francisco Park, Joachim Stadel, Risa Wechsler, and Sihan Yuan for useful conversations about the ABACUSUMMIT program.

APPENDIX

A. SATELLITE PLACEMENT IN HOSTS: PARTICLE- VERSUS HALO-PERSPECTIVE

The satellite occupation scheme in §3.2.2 can be implemented either at the particle or at the halo level with subtle, yet important, differences. We summarize them here:

- *Particle level*: each DM particle is assigned a retention probability computed from Eq. 8. Then a Bernoulli trial is performed for each particle to decide whether it is a satellite, based on that probability.

If not properly normalized, these probabilities tend, by construction, to overpopulate most massive hosts, skewing the 1-halo clustering term. In fact, by sampling a very large number of trials per halo, one tends to systematically

¹⁵ <https://www.tng-project.org>

exceed the intended mean, especially in massive halos, which dominate the total satellite count. As a result, massive halos accumulate more excess, and this shifts the overall satellite abundance upward compared to a single draw per halo.

In principle, this excess could also be mitigated by smoothly truncating the maximum number of satellites per host, but this introduces artifacts, especially in the projected clustering. Therefore, the best is to properly normalize the expected number of satellites to the total number of particles per halo and follow from there.

The particle-level approach has the great advantage that satellites are sampled from a non-parametric, irregular spatial distribution, i.e. the actual particle distribution, which provides the model natural anisotropy and stochasticity, especially on small scales. This leads to a more flexible and descriptive clustering model in the sub-Mpc regime, with satellites tracing different DM features of the halo shape (e.g., triaxiality, concentration, sub-structure).

- *Host level:* each host is assigned an expected number of satellites given by Eq. 8. Then, satellites are selected among its DM particles using a Poisson distribution with that expected number. This guarantees full control on the maximum satellite occupancy in massive hosts, so that normalization or truncation are not necessary.

However, the occupation is completely locked by the host halo, independently from how many particles it has, and does not capture the halo-to-halo variation (i.e., all halos of a given mass look identical). In other words, the halo-level occupation assumes satellites are indistinguishable and not tied to any particular substructure inside the halo. As a consequence, the clustering model loses flexibility and realism in the 1-halo term.

The satellite occupation we adopt in the analysis is at the particle level with proper normalization. In this way, we maximize the control of the occupancy, as well as the model flexibility; see § 3.2.2 for details.

B. SATELLITE CORE SUPPRESSION

The cuspy behavior of DM particle profiles in high-resolution simulations can be mitigated by probabilistically downsampling particles in the halo core using a retain probability defined as:

$$P_{\text{keep}}(r_i) = \left(\frac{r_i}{r_i + R_{\text{h},i}^{\text{vir}}} \right)^\alpha \quad \text{with } i = 1, \dots, N_p, \quad (\text{B1})$$

where r_i is the 3D radial distance of each particle from its central host, $R_{\text{h},i}^{\text{vir}}$ is the host virial radius fixing the scale of the transition, and α determines the steepness of the suppression.

This downsampling reduces the number of satellites selected near the halo core, mimicking halo core disruption, while preserving the outer halo profile. This is especially effective for tuning the projected correlation function, leaving the anisotropic clustering mostly unaffected.

This core suppression can be combined with a radial suppression of close particle-particle (i.e., satellite-satellite) pairs in projected 2D separation, r_p based on a retain probability defined as:

$$P_{\text{keep}}(r_p) = \frac{s}{1 + \left(\frac{r_p}{r_{\text{cut}}} \right)^2}, \quad (\text{B2})$$

where r_p is the projected separation of the satellites composing the pair, s is a parameter regulating the strength of the suppression, and r_{cut} is the maximum radius within which the suppression is applied. This specific shape ensures high suppression at small separations and gradual retention at larger distances.

Note that, in our analysis, we do not apply any of the above downsamplings, as we modulate the satellite profile using the K_{out} parameter (Eq. 11).

C. IMPACT OF THE MODEL PARAMETERS ON THE CLUSTERING

We investigate how the ELG1, LRG3, and ELG1×LRG3 two-point statistics respond to $\pm 10\%$ variations of the HOME physical parameters around their fiducial values reported in Table 4. As expected, the LRG auto-correlation functions are not affected by a change in the ELG model parameters, as the LRG selection is completely independent. On the other hand, the ELG auto-correlations do change with the HOD LRG parameters, since the ELG

selection is conditional to the LRG assignment. In other words, the LRG parameters propagate into the ELG and cross observables, while the ELG variables do not feed back into LRG clustering.

In what follows, we show the ratios of the model including the variation over the fiducial one. We represent a +10% (−10%) variation in blue (cyan) for ELG, in red (orange) for LRG, and in black (grey) for their cross-correlation.

Figure 19 shows the impact of changing the ELG HOD (top) and LRG HOD (bottom) parameters. We observe that:

- $\log M_{\text{cut}}$: Varying the cutoff mass has only a mild impact on the projected correlation functions, regardless of tracer, whereas the monopole and especially the quadrupole remain sensitive to it on small and intermediate scales. When the ELG cutoff mass ($\log M_{\text{cut}}^{\text{elg}}$) is varied (blue/turquoise curves), both the ELG and ELG×LRG clustering respond noticeably—most clearly in the quadrupole—because this parameter controls how many ELG centrals populate the low-mass end of the halo distribution. In contrast, varying the LRG cutoff mass ($\log M_{\text{cut}}^{\text{lr}}g$) (red/orange curves) induces a significant response not only in the LRG multipoles but also in the ELG and cross statistics (blue/turquoise and black/gray curves). This occurs because ELG assignment is conditional on the LRG catalog: shifting the LRG cutoff changes which halos are removed from the pool available to ELGs, thereby propagating LRG-side variations into all tracers.
- $\log M_1$: Varying the satellite-onset mass scale $\log M_1$ produces strong, scale-dependent responses across all tracers, since this parameter controls the mass at which halos begin to host satellites. When the ELG parameter ($\log M_1^{\text{elg}}$) is varied (blue/turquoise curves), the ELG and cross signals respond with a clear enhancement or suppression of the small-scale monopole, quadrupole, and $w_p(r_p)$, reflecting the rapid change in ELG satellite abundance. The impact on the LRG statistics (red/orange curves) is minimal, consistent with ELG variations not propagating backward into the LRG assignment.

By contrast, varying LRG parameter ($\log M_1^{\text{lr}}g$; red/orange curves) induces a strong change not only in the LRG clustering but also in the ELG and cross correlations (blue/turquoise and black/gray curves). Because ELGs are assigned conditional to LRGs, shifting the LRG satellite threshold alters the distribution of halos already occupied by LRG satellites, modifying the pool of available central halos for ELG occupancy. Lowering $\log M_1^{\text{lr}}g$ increases the number of LRG satellites, pushing ELGs into lower-mass halos and thereby reducing their small-scale contrast, whereas raising it has the opposite effect. As a result, the LRG $\log M_1$ parameter has a cascade effect, shaping not only the LRG 1-halo term, but also the ELG and ELG×LRG small-scale amplitudes through the hierarchical selection built into HOME.

- β : Varying the satellite-occupation slope produces clear and highly scale-dependent effects on the small-scale clustering of all tracers, since this parameter regulates how rapidly the satellite number rises above $\log M_{\text{cut}}$. When β^{elg} is varied (blue/turquoise curves), the impact is strongest in the cross monopole and quadrupole (black/gray curves) and remains visible in the ELG signal (blue/turquoise). A steeper slope quickly increases the ELG satellite fraction, amplifying the 1-halo term and deepening the quadrupole suppression from stronger virial motions. Because ELGs are selected based on LRGs, these variations have almost no effect on the LRG auto-correlation (red/orange).

Changes in $\beta^{\text{lr}}g$ (red/orange curves) produce a much broader response: the LRG small-scale clustering is strongly modified—through enhanced or reduced satellite abundance—and this propagates into the ELG and cross statistics (blue/turquoise and black/gray curves). Steeper $\beta^{\text{lr}}g$ values populate more satellites in high-mass halos, boosting the LRG 1-halo amplitude and simultaneously reducing the number of halos available for ELG occupation, which softens the ELG small-scale signal. In the quadrupole, increasing either β^{elg} or $\beta^{\text{lr}}g$ enhances virial motions and deepens the small-scale anisotropy suppression, but the effect is strongest for LRGs due to their higher satellite fraction.

- κ : It regulates how quickly the satellite occupation rises once the halo mass exceeds $\log M_{\text{cut}}$. Its impact is weaker than that of $\log M_{\text{cut}}$ or $\log M_1$, but it still leaves a noticeable imprint on the small- and intermediate-scale clustering. For ELGs (blue/turquoise curves), decreasing κ^{elg} shifts satellites toward lower-mass hosts and steepens the small-scale upturn in all clustering statistics. Because ELGs are assigned after LRGs, varying κ^{elg} also propagates into the cross-correlation, modifying its 1-halo term.

For LRGs (red/orange curves), the effect is milder: their satellite population already resides in massive halos where the occupation is near-saturated, so changing $\kappa^{\text{lr}}g$ mainly induces small rescalings of the monopole and quadrupole. Nonetheless, the ELG signal still responds significantly, again due to the conditional ELG selection.

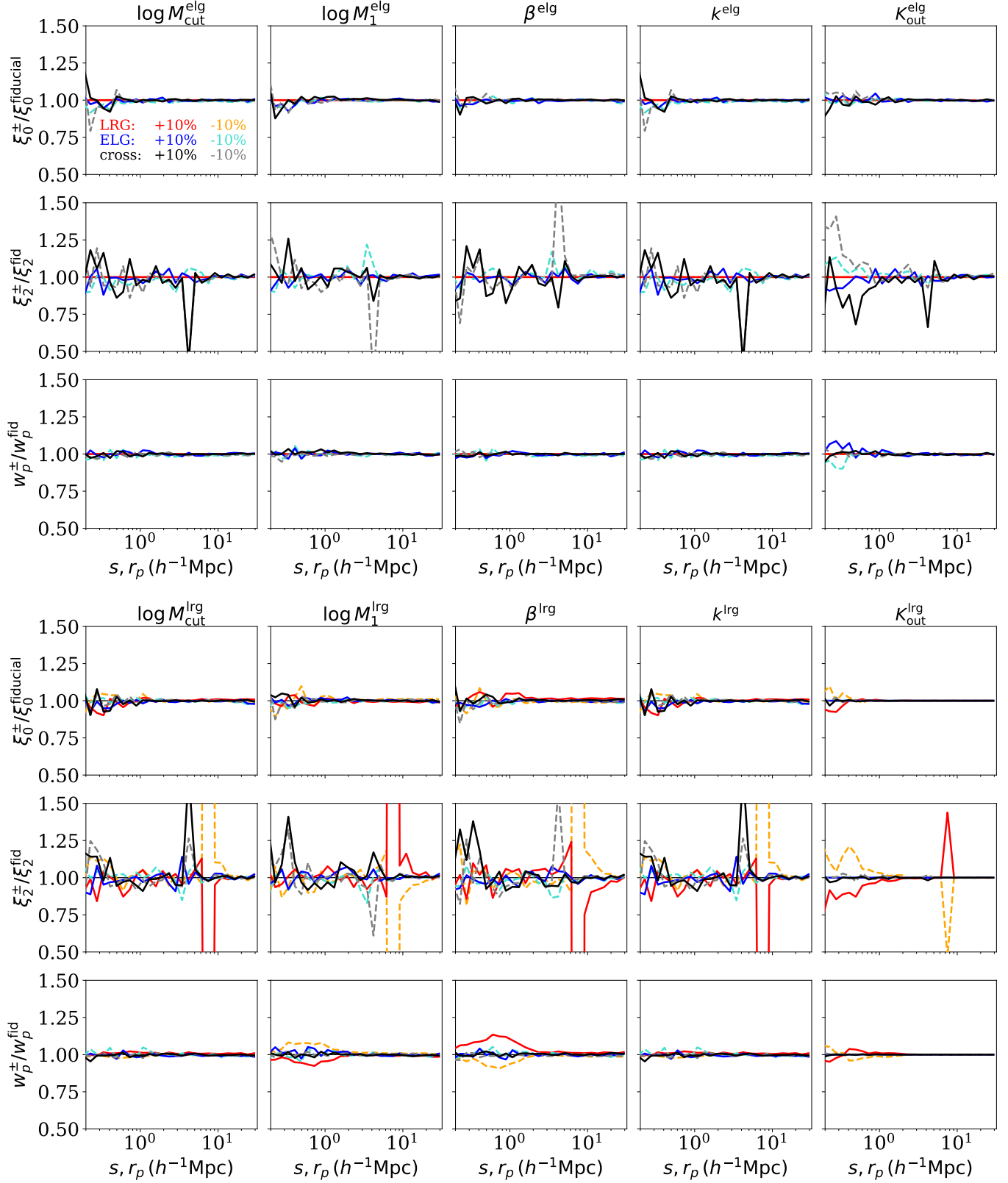


Figure 19. Impact of a $\pm 10\%$ variation in the HOD ELG (top panels) and HOD LRG (bottom) fiducial best-fit parameters on the ELG1 (blue and turquoise), LRG3 (red and orange), and ELG1 \times LRG3 (black and grey) clustering. We show the ratio between the model including the variation and the fiducial one; on top of each panel we indicate the parameter that is varying.

- K_{out} : It controls the radial repositioning of satellites within halos (Eq. 11). It has a strong, highly characteristic impact on all small-scale clustering statistics of both tracers.

Increasing K_{out} spreads satellites to larger radii, thereby suppressing the sharp small-scale rise in $w_p(r_p)$, lowering the monopole at $s \lesssim 2 h^{-1}\text{Mpc}$, and damping the quadrupole (weaker FoG elongation). Decreasing it concentrates satellites toward halo centers and enhances these signatures.

The effect is especially pronounced for LRGs (red/orange curves), whose high satellite fraction makes their 1-halo term extremely sensitive to the radial profile. As a consequence of the hierarchical assignment, varying $K_{\text{out}}^{\text{lr}}g$ also modifies the ELG and cross clustering (blue/turquoise and black/gray curves), because ELGs are placed after LRGs and thus respond to the altered spatial distribution of LRG hosts and satellites. Conversely, varying $K_{\text{out}}^{\text{elg}}$ affects only ELG and ELG×LRG, leaving the LRG auto-correlation essentially unchanged.

Among the HOD ingredients, the parameters that most strongly shape the small- and intermediate-scale clustering are those that directly regulate satellite abundance and spatial distribution. The mass scale for satellite onset, $\log M_1$, is the single most influential lever: lowering it boosts the 1-halo term of all tracers, steepening the $w_p(r_p)$ upturn and enhancing the small-scale monopole and quadrupole. The satellite-occupation slope, β , provides the next most significant modulation, controlling how rapidly satellites accumulate above $\log M_{\text{cut}}$ and therefore tuning the strength and steepness of the 1-halo signal. The parameter K_{out} , which governs the radial placement of satellites, has a comparably strong effect: pushing satellites outward suppresses clustering below a few Mpc, while concentrating them enhances the FoG-induced anisotropy. In contrast, $\log M_{\text{cut}}$ and κ play secondary roles: they influence primarily the abundance of centrals in low-mass halos and only weakly affect the 1-halo term. Taken together, $\log M_1$, β and K_{out} constitute the key physical drivers of the small-scale clustering response in both tracers and their cross-correlation.

We now assess how the ELG and LRG velocity bias parameters affect the clustering by shaping the kinematics of satellites and centrals. As shown in Figure 20, we find that:

- f_σ : The incoherent velocity dispersion of satellites produces strong FoG damping. Larger f_σ suppresses the quadrupole substantially at small scales and reduces the monopole amplitude, especially in ELGs—where intra-halo satellite dynamics is most relevant—and, indirectly, in ELG×LRG. LRGs show a weaker response.
- b_r : The radial velocity bias strongly impacts both the monopole and the quadrupole. Increasing b_r enhances coherent infall, making the quadrupole more negative on $s \lesssim 10 h^{-1}\text{Mpc}$ for all tracers, with the biggest effect in ELGs—where satellites dominate small-scale anisotropy—and LRGs—where the satellite contribution is substantial.
- b_t : Changing the tangential velocity bias alters the balance between coherent infall and tangential support. The biggest impact is in LRGs, followed by ELGs, where increasing b_t by $\sim 10\%$ lowers the small-scale monopole (the extra tangential motion reduces the LOS pairwise compression) and quadrupole. Overall, b_t primarily redistributes small-scale anisotropy.
- b_{cen} : Increasing the central velocity bias adds random motions to centrals, which broadens the redshift-space distribution of the entire sample. This produces a damping of both monopole and quadrupole on small and intermediate scales. The effect is especially pronounced for LRGs and ELG×LRG, where central-central pairs dominate, and milder for ELGs.

Overall, b_r and b_t regulate the anisotropic versus isotropic components of satellite motions, f_σ damps coherent flows with added random scatter, and b_{cen} provides the strongest global control, suppressing both anisotropy and amplitude across all clustering statistics. Importantly, none of these velocity-bias parameters affects the projected correlation function, because w_p is a real-space statistic, and therefore insensitive to redshift-space distortions.

We now examine how the abundance matching parameters affect the clustering, as shown in Figure 21:

- σ_{AM} : Increasing the scatter between stellar mass and V_{peak} weakens the mapping galaxies and halos. This dilutes clustering, especially on small scales, as galaxies are redistributed into lower-bias halos. Both the monopole and $w_p(r_p)$ decrease in amplitude, while the quadrupole becomes less negative, reflecting reduced coherent infall. A tighter relation (smaller σ_{AM}) has the opposite effect, boosting bias and anisotropy. The trend is strongest for ELGs and, from those, it propagates in the cross-signal.

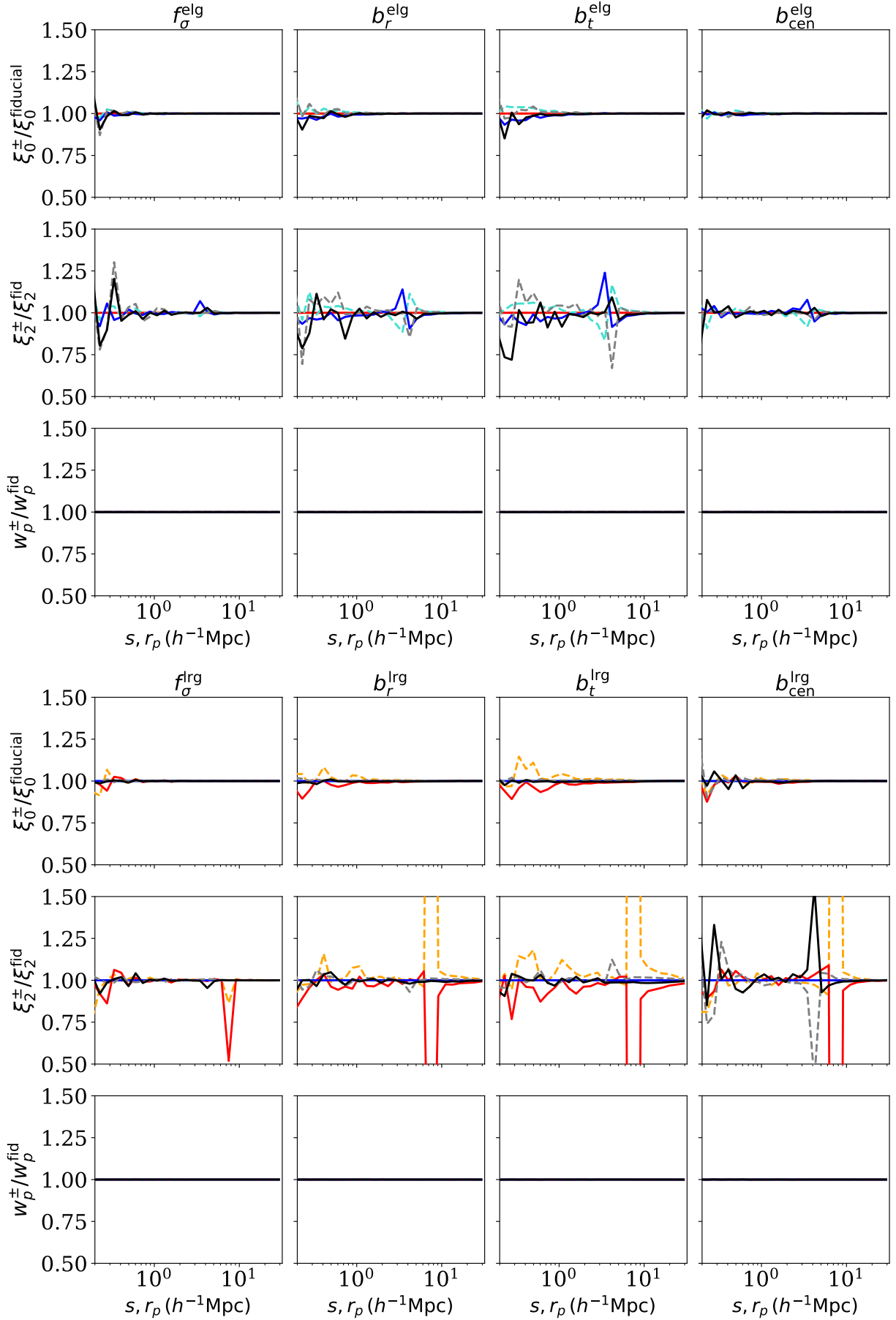


Figure 20. Impact of a $\pm 10\%$ variation in the ELG (top) and LRG (bottom) velocity bias parameters on our clustering model. Lines are color-coded as in Figure 19.

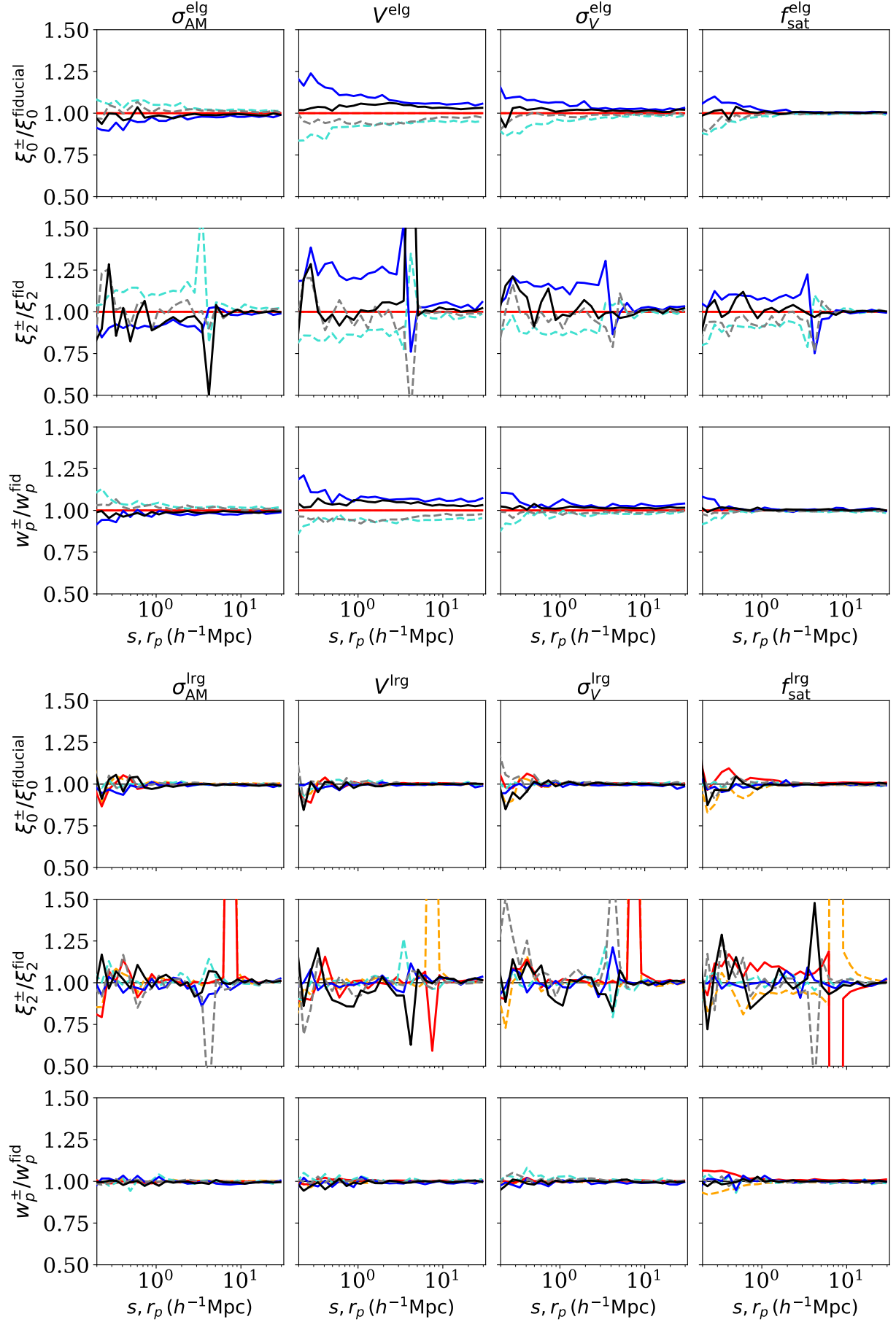


Figure 21. Impact of a $\pm 10\%$ variation in the ELG (top) and LRG (bottom) abundance-matching parameters on the clustering. Lines are color-coded as in Figure 19.

- V : These parameters set the characteristic peak circular velocities, for ELGs and LRGs, both centrals and satellites. Raising them shifts galaxies into more massive halos, increasing large-scale bias and boosting the monopole and w_p amplitude, while making the quadrupole more negative on intermediate scales due to stronger Kaiser squashing. Lowering these thresholds populates lower-mass halos, reducing bias and amplitude. The impact of these parameters is strongest for ELGs, followed by ELG×LRG, and LRG. Changing V^{elg} has stronger impact than changing V^{lg} .
- σ_V : Broadening the distribution of velocities smooths the transition in galaxy assignment, reducing sharp variations in clustering and producing smoother monopole and quadrupole shapes. Narrower distributions sharpen the transition, enhancing scale-dependent features. The effect, again, is strongest for ELGs, and milder for LRGs. The impact of changing σ_V^{elg} is stronger than σ_V^{lg} .
- f_{sat} : The satellite fraction is a key driver of the 1-halo term. Increasing f_{sat} strongly boosts the monopole and quadrupole on sub-Mpc scales and produces a steep upturn in w_p , while lowering it suppresses all small-scale signals. This effect is pronounced both in the ELG and LRG models, underscoring the sensitivity of small-scale clustering to satellite abundance.

Overall, all AM parameters are major drivers of the two-point statistics: σ_{AM} alters the overall bias and anisotropy; V shifts populations coherently across halo mass, producing large-amplitude changes; σ_V reshapes the transfer function between halo mass and tracer type, strongly affecting all clustering signals; f_{sat} controls the 1-halo term and dominates small-scale anisotropy. The four parameters act together as a tightly constrained system governing the full halo mass distribution of ELGs and LRGs, and their joint environmental statistics.

Figure 22 displays how halo exclusion, which regulates the minimum separation between pairs of massive halos, propagates into the clustering observables. We find that:

- M_{excl} : Increasing the exclusion mass thresholds removes close halo pairs among massive hosts, and hence also their satellites. The effect is largest in the LRG and cross-correlation functions, which are dominated by more massive pairs. The stronger the exclusion applied, the lower the 1-halo term in the monopole—since these pairs, with their satellites content, drive much of the small-scale clustering—and the intermediate/larger scales in the multipoles and $w_p(r_p)$. The impact is milder for ELGs and stronger for LRGs and the cross-signal. Lowering M_{excl} has the opposite effect, steepening the rise of the monopole and w_p in the cross-correlation and producing stronger quadrupole squashing.
- r_{excl} : Raising the exclusion radii shifts the boundary where overlap is forbidden. Larger radii strengthen the suppression at the 1-to-2-halo transition, producing a dip in the ELG×LRG monopole and $w_p(r_p)$ around a few Mpc. For ELGs, the dip is present but relatively small, while for LRGs it is barely noticeable. The quadrupole also becomes less negative, as fewer close, anisotropic pairs survive. Conversely, smaller r_{excl} weakens exclusion, allowing halos to be packed more closely and thereby increasing clustering power on small scales.
- p_{excl} : The steepness of the exclusion transition is controlled by this exclusion probability parameter. Higher p_{excl} sharpens the cutoff, making the suppression of pairs more abrupt and visible as a sharper downturn in the monopole and $w_p(r_p)$. The quadrupole also reacts with a stronger transition at the exclusion scale. Lower p_{excl} softens the cutoff, producing a smoother and more gradual suppression, with correspondingly milder quadrupole changes. Again, the effect is strongest in the cross-correlation, milder in ELGs, and small in LRGs.

Halo exclusion primarily impacts the 1-halo to 2-halo transition regime rather than the asymptotic large scales. M_{excl} sets the mass scale of the halos that are impacted, r_{excl} fixes the scale of suppression, and p_{excl} controls its sharpness. Together, they tune the relative smoothness of the transition in all three clustering statistics. The effect of halo exclusion is strongest in LRGs and in the ELG×LRG correlation functions, which are dominated by massive objects, and milder for ELGs.

Finally, we study the impact on clustering of the parameters regulating the joint occupancy of ELGs and LRGs, which emulates the effect of satellite ELG quenching in massive LRG hosts from a statistical point of view. Figure 23 shows that:

- α : Increasing the quenching strength (larger α) reduces the ELG satellite contribution in regions dominated by LRG hosts. This leads to a mild damping of the ELG monopole and quadrupole below $\sim 2 h^{-1}\text{Mpc}$, a similarly

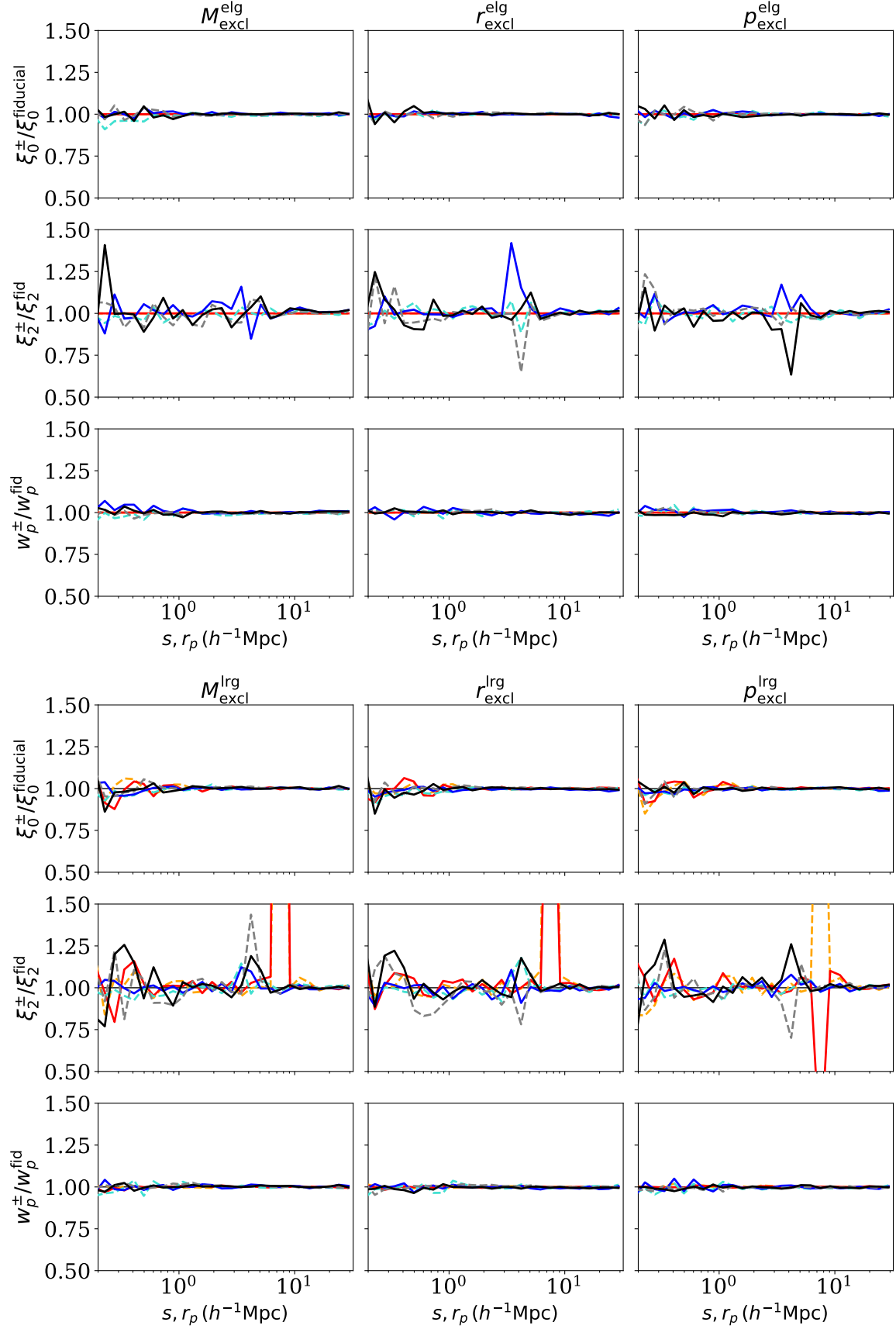


Figure 22. Impact of the ELG (top) and LRG (bottom) halo exclusion parameters on the clustering. Lines are color-coded as in Figure 19.

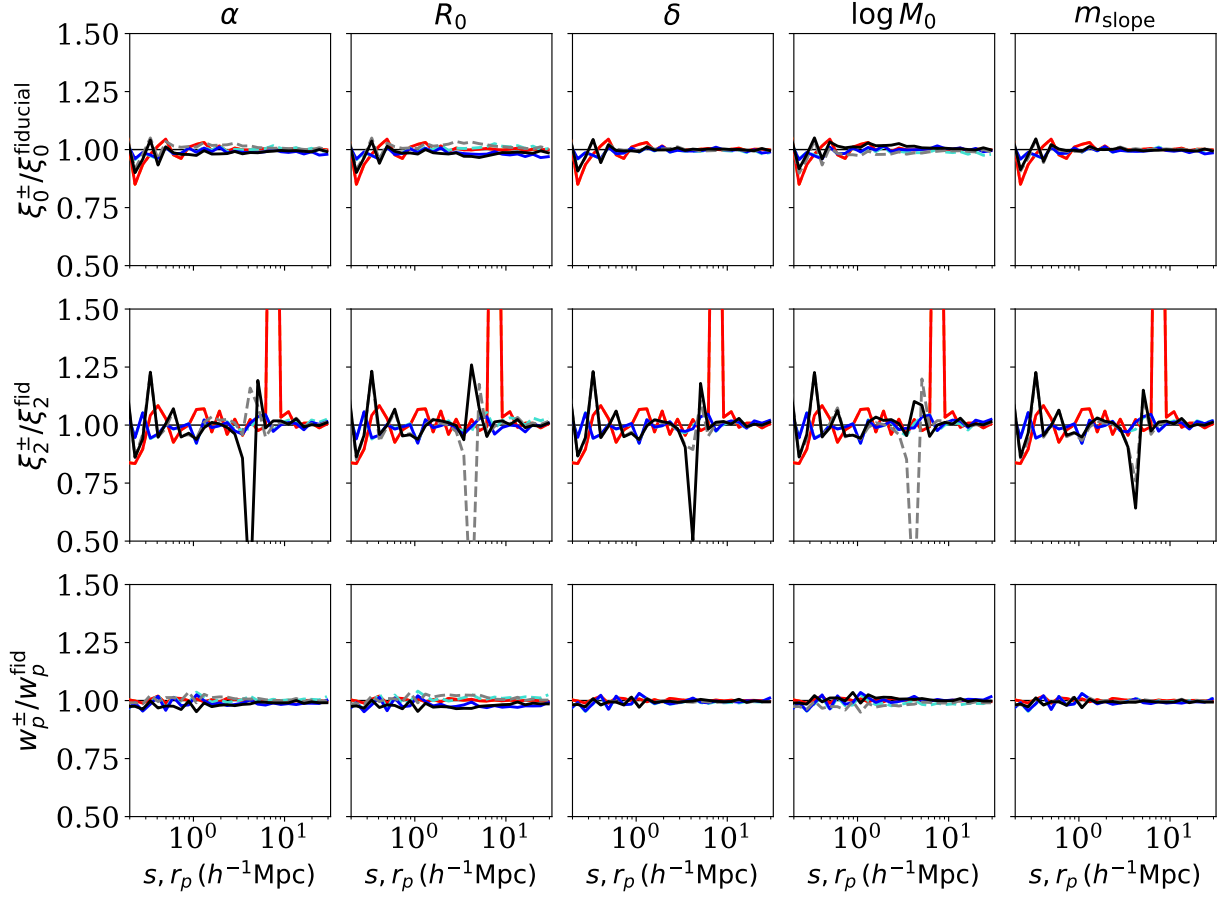


Figure 23. Impact of a $\pm 10\%$ variation in the joint occupancy model parameters that emulate ELG satellites quenching in LRG hosts. Lines are color-coded as in Figure 19.

small effect in the cross-correlation quadrupole, where ELG satellites are rare, but no effect on the LRG auto-correlation. The quadrupole is particularly affected, and becomes less negative across small and intermediate scales as the FoG signature weakens. Lowering α produces the opposite trend—satellite boost in massive halos, steepening of the small-scale rise, and deeper negative quadrupole.—with equally modest amplitude, reflecting the fact that quenching is already saturated near the best fit. Besides reducing the 1-halo term in the clustering, quenching also flattens the satellite HOD.

- R_0 : Increasing it extends the spatial reach of LRG-driven suppression, allowing more LRG halos to influence nearby ELG candidates. This produces a weak reduction of small-scale power in the ELG monopole and $w_p(r_p)$, a slight weakening of the FoG signature in the ELG quadrupole, almost no effect on LRG clustering. Decreasing R_0 tightens the quenching to the immediate neighborhood of LRG hosts, boosting the ELG 1-halo term only marginally.
- δ : Larger δ values make the suppression more sharply localized around LRG halos. However, because ELG satellites in LRG environments are already depleted, the clustering reacts moderately: small adjustments in the ELG and cross-correlation multipoles below $3 h^{-1} \text{Mpc}$, essentially no impact on $w_p(r_p)$ or on the LRG auto-correlation. Thus, δ fine-tunes only the shape of the quenching profile, not its global effect.
- $\log M_0$: This parameter sets the minimal LRG halo mass capable of inducing suppression. At the best-fit point, most LRG halos already lie above this threshold, so $\pm 10\%$ variations produce small adjustments to the ELG 1-halo term, and similar reactions in the cross multipoles. The clustering response remains negligible because raising or lowering M_0 by $\pm 10\%$ hardly changes the set of halos considered massive enough to quench ELGs.

Table 6. Best-fit double Schechter parameters to the total, star-forming, and quiescent galaxy stellar mass functions as observed in COSMOS2020 in our redshift ranges of interest (details in the text).

Tracer	observed z range	$\log(M^*/M_\odot)$	$\Phi_1 \times 10^{-3}$ [Mpc ³ dex ⁻¹]	$\Phi_2 \times 10^{-3}$ [Mpc ³ dex ⁻¹]	α_1	α_2
ELG	$0.8 < z < 1.1$	10.82 ± 0.12	0.85 ± 0.16	0.39 ± 0.21	-1.35 ± 0.03	0.07 ± 0.52
LRG	$0.8 < z < 1.1$	10.87 ± 0.07	0.0007 ± 0.0003	1.0265 ± 0.1427	-2.14 ± 0.21	-0.44 ± 0.09

- m_{slope} : This exponent enhances the contribution of very massive LRG halos to the suppression field. Increasing m_{slope} boosts quenched volumes around the highest-mass LRGs, which yields a faint damping of ELG small-scale anisotropies, the effect on LRG and cross statistics stays at the percent level. Since these massive LRG halos already dominate the suppression at the fiducial parameters, the model sits in a saturated regime where small changes in m_{slope} have limited impact.

Although the ELG×LRG signal is dominated by central–central pairs (§6.2.1), it remains sensitive to satellite quenching in massive hosts. This highlights that even a modest satellite population leaves a measurable imprint on redshift–space anisotropies, with quenching governing how this contribution evolves with halo mass.

In summary, the impact of the HOME physical parameters on the clustering signal is strongly tracer-dependent. Overall, we observe that the dominant effects derive from a change in the AM and HOD parameters, followed by the velocity bias, halo exclusion and quenching ones. In particular, quenching is a pivotal mechanism to precisely model the ELG×LRG joint occupancy of halos, while halo exclusion is fundamental to shape the 1-to-2-halo transition in the cross-correlation functions.

D. OBSERVED STELLAR MASS FUNCTIONS

In order to implement abundance matching (see §3.3), we adopt the COSMOS2020 stellar mass functions (Weaver et al. 2023), which are parametrized by coadding two Schechter functions with individual normalizations (Φ_1^* , Φ_2^*) and slopes (α_1 , α_2), and a single characteristic stellar mass (M^*):

$$\Phi d \log M = \ln(10) \exp(-10^{\log M - \log M^*}) \times \left[\Phi_1 \left(10^{\log M - \log M^*} \right)^{\alpha_1 + 1} + \Phi_2 \left(10^{\log M - \log M^*} \right)^{\alpha_2 + 1} \right] d \log M \quad (\text{D3})$$

Table 6 summarizes the Schechter parameters from Weaver et al. (2023) that we use to abundance match each tracer.

REFERENCES

- Adame, A. G., Aguilar, J., Ahlen, S., et al. 2025a, JCAP, 2025, 017, doi: [10.1088/1475-7516/2025/07/017](https://doi.org/10.1088/1475-7516/2025/07/017)
- . 2025b, JCAP, 2025, 012, doi: [10.1088/1475-7516/2025/04/012](https://doi.org/10.1088/1475-7516/2025/04/012)
- Alam, S., Peacock, J. A., Kraljic, K., Ross, A. J., & Comparat, J. 2020, MNRAS, 497, 581, doi: [10.1093/mnras/staa1956](https://doi.org/10.1093/mnras/staa1956)
- Alam, S., de Mattia, A., Tamone, A., et al. 2021, MNRAS, 504, 4667, doi: [10.1093/mnras/stab1150](https://doi.org/10.1093/mnras/stab1150)
- Anbajagane, D., Aung, H., Evrard, A. E., et al. 2022, MNRAS, 510, 2980, doi: [10.1093/mnras/stab3587](https://doi.org/10.1093/mnras/stab3587)
- Artale, M. C., Zehavi, I., Contreras, S., & Norberg, P. 2018, MNRAS, 480, 3978, doi: [10.1093/mnras/sty2110](https://doi.org/10.1093/mnras/sty2110)
- Asgari, M., Mead, A. J., & Heymans, C. 2023, The Open Journal of Astrophysics, 6, 39, doi: [10.21105/astro.2303.08752](https://doi.org/10.21105/astro.2303.08752)
- Avila, S., Gonzalez-Perez, V., Mohammad, F. G., et al. 2020, MNRAS, 499, 5486, doi: [10.1093/mnras/staa2951](https://doi.org/10.1093/mnras/staa2951)
- Baldauf, T., Seljak, U., Smith, R. E., Hamaus, N., & Desjacques, V. 2013, PhRvD, 88, 083507, doi: [10.1103/PhysRevD.88.083507](https://doi.org/10.1103/PhysRevD.88.083507)
- Baxter, D. C., Cooper, M. C., Balogh, M. L., et al. 2023, MNRAS, 526, 3716, doi: [10.1093/mnras/stad2995](https://doi.org/10.1093/mnras/stad2995)
- Behroozi, P., Wechsler, R. H., Hearin, A. P., & Conroy, C. 2019, MNRAS, 488, 3143, doi: [10.1093/mnras/stz1182](https://doi.org/10.1093/mnras/stz1182)
- Behroozi, P. S., Conroy, C., & Wechsler, R. H. 2010, ApJ, 717, 379, doi: [10.1088/0004-637X/717/1/379](https://doi.org/10.1088/0004-637X/717/1/379)

- Behroozi, P. S., Wechsler, R. H., & Conroy, C. 2013a, *ApJ*, 770, 57, doi: [10.1088/0004-637X/770/1/57](https://doi.org/10.1088/0004-637X/770/1/57)
- Behroozi, P. S., Wechsler, R. H., & Wu, H.-Y. 2013b, *ApJ*, 762, 109, doi: [10.1088/0004-637X/762/2/109](https://doi.org/10.1088/0004-637X/762/2/109)
- Berlind, A. A., & Weinberg, D. H. 2002, *ApJ*, 575, 587, doi: [10.1086/341469](https://doi.org/10.1086/341469)
- Blanton, M. R., & Berlind, A. A. 2007, *ApJ*, 664, 791, doi: [10.1086/512478](https://doi.org/10.1086/512478)
- Bluck, A. F. L., Piotrowska, J. M., & Maiolino, R. 2023, *ApJ*, 944, 108, doi: [10.3847/1538-4357/acac7c](https://doi.org/10.3847/1538-4357/acac7c)
- Chaves-Montero, J., Angulo, R. E., Schaye, J., et al. 2016, *MNRAS*, 460, 3100, doi: [10.1093/mnras/stw1225](https://doi.org/10.1093/mnras/stw1225)
- Chen, Y.-C., Ho, S., Mandelbaum, R., et al. 2017, *MNRAS*, 466, 1880, doi: [10.1093/mnras/stw3127](https://doi.org/10.1093/mnras/stw3127)
- Chuang, C.-H., & Wang, Y. 2013, *MNRAS*, 431, 2634, doi: [10.1093/mnras/stt357](https://doi.org/10.1093/mnras/stt357)
- Conroy, C., Wechsler, R. H., & Kravtsov, A. V. 2006, *ApJ*, 647, 201, doi: [10.1086/503602](https://doi.org/10.1086/503602)
- Contreras, S., Angulo, R. E., Chaves-Montero, J., White, S. D. M., & Aricò, G. 2023, *MNRAS*, 520, 489, doi: [10.1093/mnras/stad122](https://doi.org/10.1093/mnras/stad122)
- Contreras, S., Angulo, R. E., & Zennaro, M. 2021, *MNRAS*, 504, 5205, doi: [10.1093/mnras/stab1170](https://doi.org/10.1093/mnras/stab1170)
- Davis, M., & Peebles, P. J. E. 1983, *ApJ*, 267, 465, doi: [10.1086/160884](https://doi.org/10.1086/160884)
- DESI Collaboration, Aghamousa, A., Aguilar, J., et al. 2016, arXiv e-prints, arXiv:1611.00037, doi: [10.48550/arXiv.1611.00037](https://doi.org/10.48550/arXiv.1611.00037)
- DESI Collaboration, Abareshi, B., Aguilar, J., et al. 2022, *AJ*, 164, 207, doi: [10.3847/1538-3881/ac882b](https://doi.org/10.3847/1538-3881/ac882b)
- DESI Collaboration, Abdul-Karim, M., Adame, A. G., et al. 2025, arXiv e-prints, arXiv:2503.14745, doi: [10.48550/arXiv.2503.14745](https://doi.org/10.48550/arXiv.2503.14745)
- Donnari, M., Pillepich, A., Joshi, G. D., et al. 2021, *MNRAS*, 500, 4004, doi: [10.1093/mnras/staa3006](https://doi.org/10.1093/mnras/staa3006)
- Dutta, R., Fumagalli, M., Fossati, M., et al. 2024, *A&A*, 691, A236, doi: [10.1051/0004-6361/202450733](https://doi.org/10.1051/0004-6361/202450733)
- Favole, G., Granett, B. R., Silva Lafaurie, J., & Sapon, D. 2021, *MNRAS*, 505, 5833, doi: [10.1093/mnras/stab1720](https://doi.org/10.1093/mnras/stab1720)
- Favole, G., McBride, C. K., Eisenstein, D. J., et al. 2016a, *MNRAS*, 462, 2218, doi: [10.1093/mnras/stw1801](https://doi.org/10.1093/mnras/stw1801)
- Favole, G., Montero-Dorta, A. D., Artale, M. C., et al. 2022, *MNRAS*, 509, 1614, doi: [10.1093/mnras/stab3006](https://doi.org/10.1093/mnras/stab3006)
- Favole, G., Rodríguez-Torres, S. A., Comparat, J., et al. 2017, *MNRAS*, 472, 550, doi: [10.1093/mnras/stx1980](https://doi.org/10.1093/mnras/stx1980)
- Favole, G., Comparat, J., Prada, F., et al. 2016b, *MNRAS*, 461, 3421, doi: [10.1093/mnras/stw1483](https://doi.org/10.1093/mnras/stw1483)
- Foreman-Mackey, D., Hogg, D. W., Lang, D., & Goodman, J. 2013, *PASP*, 125, 306, doi: [10.1086/670067](https://doi.org/10.1086/670067)
- Gao, H., Jing, Y. P., Xu, K., et al. 2024, *ApJ*, 961, 74, doi: [10.3847/1538-4357/ad09d6](https://doi.org/10.3847/1538-4357/ad09d6)
- Gao, L., Navarro, J. F., Cole, S., et al. 2008, *MNRAS*, 387, 536, doi: [10.1111/j.1365-2966.2008.13277.x](https://doi.org/10.1111/j.1365-2966.2008.13277.x)
- Garrison, L. H., Eisenstein, D. J., Ferrer, D., Maksimova, N. A., & Pinto, P. A. 2021, *MNRAS*, 508, 575, doi: [10.1093/mnras/stab2482](https://doi.org/10.1093/mnras/stab2482)
- Gonzalez-Perez, V., Comparat, J., Norberg, P., et al. 2018, *MNRAS*, 474, 4024, doi: [10.1093/mnras/stx2807](https://doi.org/10.1093/mnras/stx2807)
- Guo, H., Jones, M. G., Wang, J., & Lin, L. 2021, *ApJ*, 918, 53, doi: [10.3847/1538-4357/ac062e](https://doi.org/10.3847/1538-4357/ac062e)
- Guo, H., Zheng, Z., Behroozi, P. S., et al. 2016, *MNRAS*, 459, 3040, doi: [10.1093/mnras/stw845](https://doi.org/10.1093/mnras/stw845)
- Hadzhiyska, B., Bose, S., Eisenstein, D., & Hernquist, L. 2021a, *MNRAS*, 501, 1603, doi: [10.1093/mnras/staa3776](https://doi.org/10.1093/mnras/staa3776)
- Hadzhiyska, B., Eisenstein, D., Bose, S., Garrison, L. H., & Maksimova, N. 2022, *MNRAS*, 509, 501, doi: [10.1093/mnras/stab2980](https://doi.org/10.1093/mnras/stab2980)
- Hadzhiyska, B., Tacchella, S., Bose, S., & Eisenstein, D. J. 2021b, *MNRAS*, 502, 3599, doi: [10.1093/mnras/stab243](https://doi.org/10.1093/mnras/stab243)
- Haines, C. P., Pereira, M. J., Smith, G. P., et al. 2015, *ApJ*, 806, 101, doi: [10.1088/0004-637X/806/1/101](https://doi.org/10.1088/0004-637X/806/1/101)
- Hartlap, J., Simon, P., & Schneider, P. 2007, *A&A*, 464, 399, doi: [10.1051/0004-6361:20066170](https://doi.org/10.1051/0004-6361:20066170)
- Hirschmann, M., De Lucia, G., Wilman, D., et al. 2014, *MNRAS*, 444, 2938, doi: [10.1093/mnras/stu1609](https://doi.org/10.1093/mnras/stu1609)
- Hoshino, H., Leauthaud, A., Lackner, C., et al. 2015, *MNRAS*, 452, 998, doi: [10.1093/mnras/stv1271](https://doi.org/10.1093/mnras/stv1271)
- Ishiyama, T., Prada, F., Klypin, A. A., et al. 2021, *MNRAS*, 506, 4210, doi: [10.1093/mnras/stab1755](https://doi.org/10.1093/mnras/stab1755)
- Jun, R. L., Theuns, T., Moriwaki, K., & Bose, S. 2025, arXiv e-prints, arXiv:2506.03015, doi: [10.48550/arXiv.2506.03015](https://doi.org/10.48550/arXiv.2506.03015)
- Kaiser, N. 1987, *MNRAS*, 227, 1, doi: [10.1093/mnras/227.1.1](https://doi.org/10.1093/mnras/227.1.1)
- Kitaura, F.-S., Rodríguez-Torres, S., Chuang, C.-H., et al. 2016, *MNRAS*, 456, 4156, doi: [10.1093/mnras/stv2826](https://doi.org/10.1093/mnras/stv2826)
- Klypin, A. A., Trujillo-Gomez, S., & Primack, J. 2011, *ApJ*, 740, 102, doi: [10.1088/0004-637X/740/2/102](https://doi.org/10.1088/0004-637X/740/2/102)
- Knebe, A., Knollmann, S. R., Muldrew, S. I., et al. 2011, *MNRAS*, 415, 2293, doi: [10.1111/j.1365-2966.2011.18858.x](https://doi.org/10.1111/j.1365-2966.2011.18858.x)
- Kraljic, K., Arnouts, S., Pichon, C., et al. 2018, *MNRAS*, 474, 547, doi: [10.1093/mnras/stx2638](https://doi.org/10.1093/mnras/stx2638)
- Kravtsov, A. V., Berlind, A. A., Wechsler, R. H., et al. 2004, *ApJ*, 609, 35, doi: [10.1086/420959](https://doi.org/10.1086/420959)
- Lamman, C., Eisenstein, D., Forero-Romero, J. E., et al. 2024, *MNRAS*, 534, 3540, doi: [10.1093/mnras/stae2290](https://doi.org/10.1093/mnras/stae2290)
- Laureijs, R., Amiaux, J., Arduini, S., et al. 2011, arXiv e-prints, arXiv:1110.3193, doi: [10.48550/arXiv.1110.3193](https://doi.org/10.48550/arXiv.1110.3193)

- Leauthaud, A., Saito, S., Hilbert, S., et al. 2017, *MNRAS*, 467, 3024, doi: [10.1093/mnras/stx258](https://doi.org/10.1093/mnras/stx258)
- Levi, M., Bebek, C., Beers, T., et al. 2013, arXiv e-prints, arXiv:1308.0847, doi: [10.48550/arXiv.1308.0847](https://doi.org/10.48550/arXiv.1308.0847)
- Maksimova, N. A., Garrison, L. H., Eisenstein, D. J., et al. 2021, *MNRAS*, 508, 4017, doi: [10.1093/mnras/stab2484](https://doi.org/10.1093/mnras/stab2484)
- McGee, S. L., Bower, R. G., & Balogh, M. L. 2014, *MNRAS*, 442, L105, doi: [10.1093/mnrasl/slu066](https://doi.org/10.1093/mnrasl/slu066)
- More, S., Kravtsov, A. V., Dalal, N., & Gottlöber, S. 2011a, *ApJS*, 195, 4, doi: [10.1088/0067-0049/195/1/4](https://doi.org/10.1088/0067-0049/195/1/4)
- More, S., van den Bosch, F. C., Cacciato, M., et al. 2011b, *MNRAS*, 410, 210, doi: [10.1111/j.1365-2966.2010.17436.x](https://doi.org/10.1111/j.1365-2966.2010.17436.x)
- Nagai, D., & Kravtsov, A. V. 2005, *ApJ*, 618, 557, doi: [10.1086/426016](https://doi.org/10.1086/426016)
- Navarro, J. F., Frenk, C. S., & White, S. D. M. 1997, *ApJ*, 490, 493, doi: [10.1086/304888](https://doi.org/10.1086/304888)
- Orsi, Á. A., & Angulo, R. E. 2018, *MNRAS*, 475, 2530, doi: [10.1093/mnras/stx3349](https://doi.org/10.1093/mnras/stx3349)
- Ortega-Martinez, S., Contreras, S., & Angulo, R. 2024, *A&A*, 689, A66, doi: [10.1051/0004-6361/202449597](https://doi.org/10.1051/0004-6361/202449597)
- Paranjape, A., Kovač, K., Hartley, W. G., & Pahwa, I. 2015, *MNRAS*, 454, 3030, doi: [10.1093/mnras/stv2137](https://doi.org/10.1093/mnras/stv2137)
- Peng, Y., Maiolino, R., & Cochrane, R. 2015, *Nature*, 521, 192, doi: [10.1038/nature14439](https://doi.org/10.1038/nature14439)
- Piotrowska, J. M., Bluck, A. F. L., Maiolino, R., & Peng, Y. 2022, *MNRAS*, 512, 1052, doi: [10.1093/mnras/stab3673](https://doi.org/10.1093/mnras/stab3673)
- Planck Collaboration, Aghanim, N., Akrami, Y., et al. 2020, *A&A*, 641, A6, doi: [10.1051/0004-6361/201833910](https://doi.org/10.1051/0004-6361/201833910)
- Prada, F., Ereza, J., Smith, A., et al. 2025, *A&A*, 698, A170, doi: [10.1051/0004-6361/202451022](https://doi.org/10.1051/0004-6361/202451022)
- Pujol, A., Skibba, R. A., Gaztañaga, E., et al. 2017, *MNRAS*, 469, 749, doi: [10.1093/mnras/stx913](https://doi.org/10.1093/mnras/stx913)
- Raichoor, A., Moustakas, J., Newman, J. A., et al. 2023, *AJ*, 165, 126, doi: [10.3847/1538-3881/acb213](https://doi.org/10.3847/1538-3881/acb213)
- Reddick, R. M., Wechsler, R. H., Tinker, J. L., & Behroozi, P. S. 2013, *ApJ*, 771, 30, doi: [10.1088/0004-637X/771/1/30](https://doi.org/10.1088/0004-637X/771/1/30)
- Reid, B. A., & Spergel, D. N. 2009, *ApJ*, 698, 143, doi: [10.1088/0004-637X/698/1/143](https://doi.org/10.1088/0004-637X/698/1/143)
- Rhee, J., Yi, S. K., Ko, J., et al. 2024, *ApJ*, 971, 111, doi: [10.3847/1538-4357/ad5a83](https://doi.org/10.3847/1538-4357/ad5a83)
- Rocher, A., Ruhlmann-Kleider, V., Burtin, E., et al. 2023, *JCAP*, 2023, 016, doi: [10.1088/1475-7516/2023/10/016](https://doi.org/10.1088/1475-7516/2023/10/016)
- Rodríguez-Torres, S. A., Chuang, C.-H., Prada, F., et al. 2016, *MNRAS*, 460, 1173, doi: [10.1093/mnras/stw1014](https://doi.org/10.1093/mnras/stw1014)
- Ross, A. J., Aguilar, J., Ahlen, S., et al. 2025, *JCAP*, 2025, 125, doi: [10.1088/1475-7516/2025/01/125](https://doi.org/10.1088/1475-7516/2025/01/125)
- Steinhauser, D., Schindler, S., & Springel, V. 2016, *A&A*, 591, A51, doi: [10.1051/0004-6361/201527705](https://doi.org/10.1051/0004-6361/201527705)
- Tal, T., Wake, D. A., & van Dokkum, P. G. 2012, *ApJL*, 751, L5, doi: [10.1088/2041-8205/751/1/L5](https://doi.org/10.1088/2041-8205/751/1/L5)
- Tinker, J. L., Sheldon, E. S., Wechsler, R. H., et al. 2012, *ApJ*, 745, 16, doi: [10.1088/0004-637X/745/1/16](https://doi.org/10.1088/0004-637X/745/1/16)
- Trujillo-Gomez, S., Klypin, A., Primack, J., & Romanowsky, A. J. 2011, *ApJ*, 742, 16, doi: [10.1088/0004-637X/742/1/16](https://doi.org/10.1088/0004-637X/742/1/16)
- van den Bosch, F. C., More, S., Cacciato, M., Mo, H., & Yang, X. 2013, *MNRAS*, 430, 725, doi: [10.1093/mnras/sts006](https://doi.org/10.1093/mnras/sts006)
- van den Bosch, F. C., Tormen, G., & Giocoli, C. 2005, *MNRAS*, 359, 1029, doi: [10.1111/j.1365-2966.2005.08964.x](https://doi.org/10.1111/j.1365-2966.2005.08964.x)
- Vaughan, S. P., Tiley, A. L., Davies, R. L., et al. 2020, *MNRAS*, 496, 3841, doi: [10.1093/mnras/staa1837](https://doi.org/10.1093/mnras/staa1837)
- Weaver, J. R., Davidzon, I., Toft, S., et al. 2023, *A&A*, 677, A184, doi: [10.1051/0004-6361/202245581](https://doi.org/10.1051/0004-6361/202245581)
- Wetzel, A. R., Tinker, J. L., & Conroy, C. 2012, *MNRAS*, 424, 232, doi: [10.1111/j.1365-2966.2012.21188.x](https://doi.org/10.1111/j.1365-2966.2012.21188.x)
- Wetzel, A. R., Tinker, J. L., Conroy, C., & van den Bosch, F. C. 2013, *MNRAS*, 432, 336, doi: [10.1093/mnras/stt469](https://doi.org/10.1093/mnras/stt469)
- Yu, J., Zhao, C., Chuang, C.-H., et al. 2022, *MNRAS*, 516, 57, doi: [10.1093/mnras/stac2176](https://doi.org/10.1093/mnras/stac2176)
- Yuan, S., Garrison, L. H., Hadzhiyska, B., Bose, S., & Eisenstein, D. J. 2022, *MNRAS*, 510, 3301, doi: [10.1093/mnras/stab3355](https://doi.org/10.1093/mnras/stab3355)
- Yuan, S., Zhang, H., Ross, A. J., et al. 2024, *MNRAS*, 530, 947, doi: [10.1093/mnras/stae359](https://doi.org/10.1093/mnras/stae359)
- Yuan, S., Wechsler, R. H., Wang, Y., et al. 2025, *MNRAS*, 538, 1216, doi: [10.1093/mnras/staf368](https://doi.org/10.1093/mnras/staf368)
- Zehavi, I., Zheng, Z., Weinberg, D. H., et al. 2005, *ApJ*, 630, 1, doi: [10.1086/431891](https://doi.org/10.1086/431891)
- Zhao, C. 2023, *A&A*, 672, A83, doi: [10.1051/0004-6361/202346015](https://doi.org/10.1051/0004-6361/202346015)
- Zhao, C., Kitaura, F.-S., Chuang, C.-H., et al. 2015, *MNRAS*, 451, 4266, doi: [10.1093/mnras/stv1262](https://doi.org/10.1093/mnras/stv1262)
- Zheng, Z., Coil, A. L., & Zehavi, I. 2007, *ApJ*, 667, 760, doi: [10.1086/521074](https://doi.org/10.1086/521074)
- Zheng, Z., Zehavi, I., Eisenstein, D. J., Weinberg, D. H., & Jing, Y. P. 2009, *ApJ*, 707, 554, doi: [10.1088/0004-637X/707/1/554](https://doi.org/10.1088/0004-637X/707/1/554)
- Zheng, Z., Berlind, A. A., Weinberg, D. H., et al. 2005, *ApJ*, 633, 791, doi: [10.1086/466510](https://doi.org/10.1086/466510)
- Zhou, R., Dey, B., Newman, J. A., et al. 2023, *AJ*, 165, 58, doi: [10.3847/1538-3881/aca5fb](https://doi.org/10.3847/1538-3881/aca5fb)
- Zu, Y., & Mandelbaum, R. 2015, *MNRAS*, 454, 1161, doi: [10.1093/mnras/stv2062](https://doi.org/10.1093/mnras/stv2062)
- . 2016, *MNRAS*, 457, 4360, doi: [10.1093/mnras/stw221](https://doi.org/10.1093/mnras/stw221)
- . 2018, *MNRAS*, 476, 1637, doi: [10.1093/mnras/sty279](https://doi.org/10.1093/mnras/sty279)